

HU ISSN 1586–2070

JOURNAL OF COMPUTATIONAL AND APPLIED MECHANICS

An Open Access International Journal

Published by the University of Miskolc

VOLUME 9, NUMBER 1 (2014)



MISKOLC UNIVERSITY PRESS

EDITORS

László BARANYI, Institute of Energy Engineering and Chemical Machinery, University of Miskolc, H-3515 MISKOLC, Hungary, e-mail: arambl@uni-miskolc.hu

István PÁCZELT, Institute of Applied Mechanics, University of Miskolc, H-3515 MISKOLC, Hungary e-mail: mechpacz@uni-miskolc.hu

György SZEIDL, Institute of Applied Mechanics, University of Miskolc, H-3515 MISKOLC, Hungary e-mail: Gyorgy.SZEIDL@uni-miskolc.hu

EDITORIAL BOARD

Edgár BERTÓTI, Institute of Applied Mechanics, University of Miskolc, H-3515 MISKOLC, Hungary, e-mail: edgar.bertoti@uni-miskolc.hu

Atila BAKSA, Institute of Applied Mechanics, University of Miskolc, H-3515 MISKOLC, Hungary, attila.baksa@uni-miskolc.hu

István ECSEDI, Institute of Applied Mechanics, University of Miskolc, H-3515 MISKOLC, Hungary, mechecs@uni-miskolc.hu

Ulrich GABBERT, Institut für Mechanik, Otto-von-Guericke-Universität Magdeburg, Universitätsplatz 2, 39106 MAGDEBURG, Germany, ulrich.gabbert@mb.uni-magdeburg.de

Zolt GÁSPÁR, Department of Structural Mechanics, Budapest University of Technology and Economics, Műgyetem rkp. 3, 1111 BUDAPEST, Hungary, gaspar@ep-mech.me.bme.hu

Robert HABER, Department of Theoretical and Applied Mechanics, University of Illinois at Urbana-Champaign, 216 Talbot Lab., 104 S. Wright Str., URBANA, IL 61801, USA, r-haber@uiuc.edu

Csaba HÓS, Department of Hydraulic Machines, Budapest University of Technology and Economics, Műgyetem rkp. 3, 1111 BUDAPEST, Hungary, HOSCSABA@vizgep.bme.hu

Károly JÁRMAI, Institute of Logistics, University of Miskolc, H-3515 MISKOLC, Hungary, altjar@uni-miskolc.hu

László KOLLÁR, Department of Strength of Materials and Structures, Budapest University of Technology and Economics, Műgyetem rkp. 3. K.II.42., 1521 BUDAPEST, Hungary, lkollar@eik.bme.hu

József KÖVECSES, Mechanical Engineering Department 817 Sherbrooke Street West, MD163 Montreal, Quebec H3A 2K6 jozsef.kovecses@mcgill.ca

Márta KURUTZ, Department of Structural Mechanics, Budapest University of Technology and Economics, Műgyetem rkp. 3, 1111 BUDAPEST, Hungary, kurutzm@eik.bme.hu

Herbert MANG, Institute for Strength of Materials, University of Technology, Karlsplatz 13, 1040 VIENNA, Austria, Herbert.Mang@tuwien.ac.at

Sanjay MITTAL, Department of Aerospace Engineering, Indian Institute of Technology Kanpur, UP 208 016, India, smittal@iitk.ac.in

Zenon MROZ, Polish Academy of Sciences, Institute of Fundamental Technological Research, Swietokrzyska 21, WARSAW, Poland zmroz@ippt.gov.pl

Gyula PATKÓ, Institute of Machine Tools and Mechatronics, University of Miskolc, H-3515 MISKOLC, Hungary, patko@uni-miskolc.hu

Jan SLADEK, Ústav stavbenictva a architektúry, Slovenskej akadémie vied, Dubróvská cesta 9, 842 20 BRATISLAVA, Slovakia, usarslad@savba.sk

Gábor STÉPÁN, Department of Applied Mechanics, Budapest University of Technology and Economics, Műgyetem rkp. 3, 1111 BUDAPEST, Hungary, stepan@mm.bme.hu

Barna SZABÓ, Center for Computational Mechanics, Washington University, Campus Box 1129, St. LOUIS, MO63130, USA, szabo@me.wustl.edu

Balázs TÓTH, Institute of Applied Mechanics, University of Miskolc, 3515 MISKOLC, Hungary, balazs.toth@uni-miskolc.hu

HONORARY EDITORIAL BOARD MEMBERS

Imre KOZÁK, Institute of Applied Mechanics, University of Miskolc, H-3515 Miskolc-Egyetemváros, Hungary

Tibor CZIBERE, Department of Fluid and Heat Engineering, University of Miskolc, H-3515 Miskolc-Egyetemváros, Hungary

R. Ivan LEWIS, Room 2-16 Bruce Building, Newcastle University, NEWCASTLE UPON TYNE, NE1 7RU, UK

Gábor HALÁSZ, Department of Hydraulic Machines, Budapest University of Technology and Economics, Műgyetem rkp. 3, 1111 BUDAPEST, Hungary,

A Short Preface for Authors and Readers

The Journal of Computational and Applied Mechanics (JCAM) came out first in 2000 and two issues a year were published till 2008. There was an increasing interest in publishing papers in the journal since the review period was relatively short and in addition the papers could be downloaded freely from the home page of the journal. It was the main objective of the editorial board to establish an international journal in Hungary which would provide an opportunity for publishing papers in the field of theoretical and applied mechanics. With regard to the research carried out at the University of Miskolc in computational mechanics (fluid mechanics and mechanics of solid bodies as well as heat conduction could be mentioned here) a special emphasis was laid on the results achieved in these fields. We planned to publish review papers and special issues were devoted to novel results in biomechanics.

The financial difficulties that began in 2008 played a role in our being unable to publish the journal between 2008 and 2013. With this issue we would like on one hand to restart the journey we began in 2000 so that we can make up for what we have missed and on the other hand to reinforce the objectives set in 2000.

It is worth emphasizing that the journal should be open access – in the same way as before – for ambitious young and also for more experienced researchers, that is, for everybody who takes an interest in doing research in theoretical and applied mechanics. In contrast to some free journals which expect the authors to pay for the review (or for the publication of a paper), JCAM insists on the novelty and the level of the papers published, and at the same time we would like to emphasize that publication as well as access to the papers published is free of charge. The review process is, however, a rigorous one: we need two positive reviews to accept a paper for publication.

We truly hope that we can regain the trust of our faithful readers, who would also honor us contributing manuscripts for publication.

László Baranyi, István Páczelt and György Szeidl

P.S. Our home page is being redesigned, which will take some time. We apologize for the inconvenience.

RESPONSE OF PLATES UNDER STATISTICALLY UNSYNCHRONIZED UNIFORM RANDOM LOADS USING MONTE-CARLO SIMULATION

JEAN-MICHEL DHAINAUT

Mechanical Engineering Department, Embry-Riddle University
Daytona Beach, FL 32114, USA

dhain460@erau.edu

GUANGFENG CHENG

Jefferson Lab
Newport News, VA 23606, USA

cheng@jlab.org

CHUH MEI

Old Dominion University
Norfolk, VA 23329, USA

cmei@odu.edu

[Received: February 8, 2007]

Abstract. Classic solutions of the responses of plates subjected to uniform random pressure are generally confined to simple boundary conditions where the assumed mode shape solutions are known. Even in those simple cases, response solutions have neglected the asymmetric modes for rectangular plates with symmetric boundary conditions due to mathematical limitations. To the best knowledge of the authors, the present paper presents for the first time the random response and fatigue life prediction for plates subjected to unsynchronized and statistically uncorrelated uniform random loads. A linear finite element formulation combined with the Monte Carlo simulation is employed to determine the stress response, and the stochastic Palmgren-Miner reliability model is used for the fatigue analysis. A simply supported rectangular plate is studied first in detail to show the contributions of both symmetric and asymmetric modes due to the unsynchronized loading. A clamped-simply supported plate is analyzed next to show the versatility of the present approach. In both cases, a significant reduction on the responses and increase in fatigue life was observed as compared to corresponding results from the uniform synchronized loading condition. Results also include RMS displacement and stress values, power spectral densities, probability density functions, and rainflow plots. Computational burden due to the unsynchronized random pressure fluctuations required the use of parallel computing capabilities.

Mathematical Subject Classification: 05C38, 15A15

Keywords: unsynchronized, random, fatigue life

1. INTRODUCTION

Currently the random acoustic pressure for sonic fatigue design and analysis of beam, plate [1, 2, 3, 4, 5, 6, 7] and shallow shell [8] structures (linear or non-linear) is often considered uniformly distributed over the surface of the structure and synchronized in

time. In addition, the random loading is generally assumed as a truncated Gaussian white noise. In two previous experiments, two clamped square aluminum plates were tested in the Wideband Noise Test Chamber of the Flight Dynamics Laboratory Sonic Fatigue Facility at WPAFB. The mean-square strains versus non-dimensional Sound Pressure Level (SPL) showed good agreement among the PDE/Galerkin/Equivalent Linearization (EL) analytical results and the experimental data [2, 9]. A steel beam rigidly clamped in a clamping fixture and mounted on a vibration shaker was also recently tested. Excellent agreement of the strain Power Spectral Density (PSD) was obtained among the experimental data and the two finite element modal results [3, 10]. In both experiments, the loading could be considered as synchronized in time and uniformly distributed, thus the asymmetric natural bending modes of the panel were not considered in the analysis. By synchronized load it is meant that the simulated random pressure load is generated from one seed number [1, 3, 7, 8, 10] (see Section III. C) for the whole surface area of the panel, and at each time step the pressure load on the beam, plate or shell is uniform. On the other hand, let us use the long period of steady rain falling on top of a flat small roof as an illustration of the unsynchronized uniform random load. The pressure of the raindrops falling on the roof surface is certainly random in nature, with more or less a fairly uniform pressure distribution in the random sense (white noise, but not identical time history). It cannot be simulated as a random uniform pressure synchronized in time coming from only one seed number, but rather as a random load with different seed number for each raindrop in an ideal simulation case. Another example of uniform random load unsynchronized in time is the 30,000 to 40,000 marathon runners across a long-span bridge, especially cable-supported. For those cases, the asymmetric as well as the symmetric modes are excited and they should be considered in the analysis. For panel design in practice, the highest measured or estimated PSD level should be used, and it may also be reasonable to assume that the PSD is a band-limited white noise, since the contribution from the high frequency modes to the panel response is usually small. Influences of acoustic pressure with nonwhite PSD (synchronized) on maximum deflection, stress/strain and fatigue life have been investigated recently for plates[?] and shallow shells.[?]. This paper studies the random response and fatigue life of isotropic rectangular plates subjected to a uniformly distributed random pressure load unsynchronized in time. Results show that the Root Mean Square (RMS) deflections and maximum stress are reduced and the fatigue life is increased for the unsynchronized as compared with the traditional synchronized loading case.

2. ANALYTICAL SOLUTION

The mathematical difficulties in considering the asymmetric modes in the response of a plate under uniformly distributed random load (white-noise) using the classic analytical method is briefly explained first. Considering the linear vibrations of a Simply-Supported (S-S) isotropic plate subjected to a uniformly distributed random pressure $P(t)$. The transverse displacement $w(x, y, t)$ of a $a \times b \times h$ (length \times width \times thickness)

panel can be represented as

$$w(x, y, t) = \sum_{r=1}^m \sum_{s=1}^n q_{r,s}(t) \sin\left(\frac{r\pi x}{a}\right) \sin\left(\frac{s\pi y}{b}\right), \quad (r, s) = 1, 2, 3\ldots \quad (1)$$

The classic analytical partial differential equation (PDE) and normal mode approach leads to the modal equations for the damped motion of the panel as

$$\ddot{q}_{r,s} + 2\zeta_{r,s}\omega_{r,s}\dot{q}_{r,s} + \omega_{r,s}^2 q_{r,s} = \frac{\gamma_{r,s}}{m_{r,s}} P(t), \quad (r, s) = 1, 3, 5\ldots \quad (2)$$

By setting $(r, s) = m$ and $(k, l) = n$, the mean-square values of the modal amplitudes are

$$E[q_m^2] = \frac{\gamma_m^2 S_0}{8m^2 \zeta_m \omega_m^3} \quad (3)$$

and

$$\begin{aligned} E[q_m q_n] &= \\ &= \frac{\gamma_m \gamma_n (\zeta_m \omega_m + \zeta_n \omega_n) S_0}{m_m m_n \left[(\omega_m^2 - \omega_n^2)^2 + 4\omega_m \omega_n (\zeta_m \omega_m + \zeta_n \omega_n) (\zeta_m \omega_n + \zeta_n \omega_m) \right]} \end{aligned} \quad (4)$$

where ζ_m is the modal damping coefficient, ω_m the natural frequency corresponding to the (r, s) mode, respectively, and $m = \frac{\rho h a b}{4}$ the constant modal mass. The coefficient $\gamma_{r,s} = \gamma_m$ is the result from the application of the PDE/normal mode approach as

$$\int_0^a \int_0^b P(t) \sin\left(\frac{r\pi x}{a}\right) \sin\left(\frac{s\pi y}{b}\right) dx dy = \begin{cases} P(t) \gamma_m & \text{for } (r, s) = \text{odd} \\ 0 & \text{for } r \text{ or } s = \text{even} \end{cases} \quad (5)$$

where $\gamma_m = \frac{4ab}{rs\pi^2}$. The γ_m value from equations (3) and (5) implies that only the symmetric modes (r and $s = \text{odd}$) are excited with the uniformly distributed random pressure $P(t)$ synchronized in time since for asymmetric modes, (r or $s = \text{even}$), the integration of equation (5) over the surface of the panel is zero.

The definition of $P(t)$ is a rather restricted case of random load since at any instant time the pressure is constant at any location of the panel, and thus $P(t)$ is statistically synchronized in time. This synchronized uniform random pressure $P(t)$ does not fit the more general stochastic definition of band-limited white noise pressure,

$$S_p(\xi, \eta, f) = \begin{cases} S_0 & \text{if } 0 \leq f \leq f_u \\ 0 & \text{if } f < 0 \text{ or } f > f_u \\ \xi = x_1 - x_2 \\ \eta = y_1 - y_2 \end{cases} \quad (6)$$

where the spatial separations are denoted by $\xi = x_1 - x_2$, $\eta = y_1 - y_2$, and the upper cut-off frequency in hertz (Hz) by f_u . The auto-spectral density function of the random excitation is defined as

$$S_0 = P_0^2 10^{SPL/10} \quad (7)$$

where SPL denotes the sound pressure level in decibels (dB), and P_0 is the reference pressure equal to 2.9008×10^{-9} psi (20μ Pa). Explicitly, the time histories of random pressure $P(x, y, t)$ at any two points of the panel could be different and statistically unsynchronized in time, however, their PSD values (S_o) should be the same. This statistically unsynchronized uniformly distributed random pressure would certainly excite the asymmetric (r or s =even) as well as symmetric (r or s =odd) modes. However, as it can be easily seen from equation (5) that the asymmetric modes would not be considered in the analytical PDE/normal mode solution. The steady rain and the marathon runners discussed earlier are two examples of statistically unsynchronized uniform random loads just addressed.

3. FORMULATION AND SIMULATION

3.1. Finite Element Formulation.

Structural Node Degree of Freedom (DOF)

The finite element employed in the present study is the C^1 -conforming Bogner-Fox-Schmit [11] (BFS) plate element, which has a total of 16 bending DOF $\{w_b\}$:

$$\{w_b\} = \{w_k \ w_{,xk} \ w_{,yk} \ w_{,xyk}\}^T \quad (8)$$

Applying the principle of virtual work, the system equations of motion are derived,

$$[M_b] \{\ddot{W}_b\} + [K_b] \{W_b\} = \{P\} \quad (9)$$

where $[M_b]$ and $[K_b]$ are the system consistent mass and stiffness matrices, and $\{P\}$ is the load vector for uniform random loading.

Modal DOF

The system equations of motion in the structural DOF are then transformed into a set of truncated modal coordinates by expressing the plate response as a linear combination of some base functions as

$$\{W_b\} = \sum_{m=1}^l q_m(t) \{\phi_b\}^{(m)} = [\Phi] \{q\} \quad (10)$$

where $\{\phi_b\}^{(m)}$ corresponds to the m -th normal mode of the linear vibration problem. Adding a damping matrix $2\zeta_m\omega_m [I]$ where the modal damping ζ_m can be determined experimentally or from previous experience. The equations of motion, equation (9), are reduced to a set of uncoupled modal equations as

$$[\bar{M}_b] \{\ddot{q}\} + 2\zeta_r\omega_r [\bar{M}_b] \{\dot{q}\} + [\bar{K}_b] \{q\} = \{\bar{P}\} \quad (11)$$

where the diagonal modal mass and stiffness matrices are

$$([\bar{M}_b], [\bar{K}_b]) = [\Phi]^T ([M_b], [K_b]) [\Phi] \quad (12)$$

and the modal random load vector is

$$\{\bar{P}\} = [\Phi]^T \{P\} \quad (13)$$

The modal displacement $\{q\}$ in equation (11) is obtained by the fourth order Runge-Kutta (RK4) numerical integration scheme. The system bending displacement $\{W_b\}$

is then calculated with equation (10), and the stress vector $\{\sigma\}$ at the element level is evaluated with

$$\{M\} = [D] \{\kappa\}, \quad \{\sigma\} = \left(\pm \frac{6}{h^2} \right) \{M\} \quad (14)$$

where h is the thickness, $\{M\}$ the bending moment vector, $\{\kappa\}$ the curvature, and $[D]$ the bending stiffness matrix of the plate. For the displacement based finite element method, the stress calculation is not as accurate as displacement calculation. According to Barlow [12] the stresses are more precise if calculated at the Barlow points and then extrapolated to the nodal points or other desired point.

3.2. Fatigue Life Estimation - RFC Method.

The Palmgren-Miner [13] cumulative damage theory method is employed for fatigue life analysis in the time domain

$$D = \sum_{i=1}^k \frac{n_i}{N_i} = 1.0 \quad (15)$$

where D is the damage and n_i and N_i are the actual number of cycles at a given stress level and the number of total cycles at which failure occurs at the same stress level. The stress/strain versus the number of cycles to failure (S-N) curve normally takes the form,

$$N = K/S^\beta \quad (16)$$

where the material constants K and β are determined experimentally. For random response, the Palmgren-Miner [13] theory is rewritten as

$$E[D(t)] = \frac{1}{K} \int_0^\infty p(s) s^\beta ds = E \left[\frac{1}{K} \sum p(s) s^\beta \right] = E \left[\frac{1}{K} \sum s_k^\beta \right] \quad (17)$$

where $p(s)$ is the stress/strain range Probability Distribution Function (PDF). Based on equations (15) and (17) the simplest fatigue life estimate is

$$T^f = \frac{1}{E[D(t)]} \quad (18)$$

Some of the cycles counting methods to predict $p(s)$ are: (i) the peak counting method, (ii) the range counting method, and (iii) the Rainflow Counting Cycles (RFC) method. Langley and McWilliam [14] showed that the first two methods give similar results for narrow-band processes, but quite different for a wide-band process. The RFC method uses a specific counting scheme to account for effective stress ranges and identified stress cycles related to closed hysteresis loops in the stress-strain curves. The validity of the RFC method was studied in detail by Dowling [15] where the accuracy of fatigue life predictors was based on eight commonly used cycle counting methods. Dowling concluded that the RFC method was the only accurate method for wide-band processes. The RFC algorithm used in this paper was provided as part of the Wave Analysis for Fatigue analysis and Oceanography [16] (WAFO) toolbox. In addition, Bishop and Sherratt [17] showed that fatigue life of wide-band Gaussian signal using the RFC yields to the most realistic estimates.

3.3. Synchronized Random Pressure Generation.

Consider a uniformly distributed random pressure $P(t)$ that is characterized by the auto-spectral density function defined by equation (6) and (7). A simple process possessing such a PSD is a truncated white noise and its samples are assumed here to be drawn according to a Gaussian distribution. An algorithm [1, 3] that simulates a random pressure using complex numbers with independent random phase angles uniformly distributed between 0 and 2π is used to generate the band-limited truncated white noise [1, 3, 8]. The algorithm uses a random number generator that needs an initial seed number (ISEED). Once the random pressure time history is generated the average value of the auto-spectral density is calculated and compared to S_0 for a given SPL. Each pressure time history had a time history of 1 second, a cut-off frequency of 4096 Hertz (Hz), a time step $\Delta t = 1/2^{16}$ second, and a total of 65536 (NPT) pressure data points.

3.4. Unsynchronized Random Pressure Generation.

The unsynchronized random load generation follows alike procedure as the synchronized load case, except that for each plate element, a random load is generated with a different ISEED number. Using different ISEED numbers guaranties that each random pressure time history to be different from one another as shown in Figure 1.

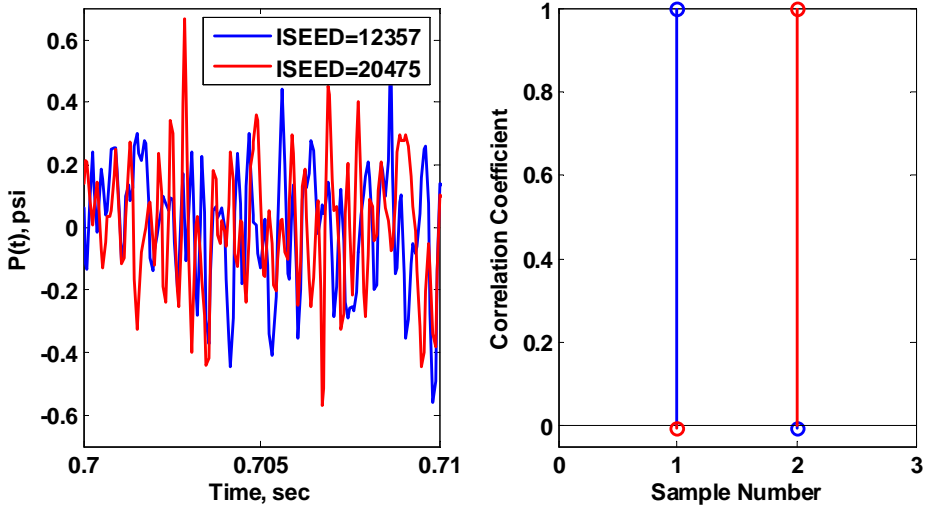


Figure 1. Random load generation for ISEED=14407 and ISEED=12357

This phenomenon was referred in the introduction as the simulation of the raindrops and/or the marathon runners' steps on a cable-supported bridge. Table 1 shows that pressure histories from 5 different ISEED numbers have a PSD equal to mean value of S_0 at SPL=100 dB.

Table 1. Load generation from 5 different ISEED numbers

<i>ISEED</i>	<i>Analytical</i>	<i>PSD*</i>	<i>Time history**</i>	<i>*Err. %</i>	<i>**Err. %</i>
20392	3.44651799e-2	3.446530047e-2	3.453362e-2	0.00034	-0.1985
20462	3.44651799e-2	3.446530048e-2	3.459602e-2	0.00034	-0.3796
20506	3.44651799e-2	3.446530047e-2	3.435795e-2	0.00034	0.3111
20527	3.44651799e-2	3.446530047e-2	3.445678e-2	0.00034	0.02435
12357	3.44651799e-2	3.44653004e-2	3.446085e-2	0.00034	0.01254

Analytical: Power= $(P_{ref}^2 10^{SPL/10}) \times f_u$, PSD*: Power=mean(S_0) $\times f_u$, and Time history**: Power= $P(t)^2/NPT$

A more detailed analysis using the correlation coefficient command in MATLAB has shown that the pressure time histories were statistically uncorrelated to each other as shown in Figure 1. For instance, if a generated pressure time history was compared with fifty others (all with different ISEED numbers), the lowest correlation coefficient found was 0.0011 and the highest 0.0264, where a correlation coefficient of 0 indicates no relationship and a coefficient of 1.0 indicates the highest possible relationship (correlation factor of the pressure time histories with each other).

3.5. Parallel Computations.

The computational burden caused by the storage of the random loads from different ISEED numbers was resolved by the use of parallel computing facilities at Embry-Riddle Aeronautical University. In Matlab the Distributed Computing Toolbox (DCT) and the Distributed Computing Engine (DCE) enable to develop parallel MATLAB applications and execute them on a cluster of computers without leaving the Matlab environment. A local UNIX machine was used to connect to the DCE installed in the cluster. The MCS-FE code was run into two workers (nodes) 4 GB Ram memory each; the first worker was used as storage for the huge amount of data points contained in the load matrix. (There are 1024 columns each containing 16384 points). The second worker is used exclusively to run the modal finite element numerical simulation. The program is at the first stage to be adapted for parallel computing capabilities. At this stage the program was modified such that at each time step the FE-MCS was able to call the corresponding random pressure values contained in the load matrix. In a near future the program would be optimized to be able to run on multiples nodes which will significantly increase the number of degree of freedom (or mesh size) and it will decrease the computational time.

4. RESULTS AND DISCUSSION

The responses of a plate under the synchronized uniform random pressure are studied first. Results are compared between the analytical solution (see section II) and the Finite Element code (FE) which uses the Monte Carlo Simulation (MCS). Next, the same panel is subject to an unsynchronized random load, and results are quantitatively compared to previous ones. Finally, the FE modal formulation is generalized by the study of the response of a panel with mixed (asymmetric) boundary conditions under the unsynchronized uniform random pressure.

4.1. Validation. A Simply-Supported (S-S) plate was first selected for validation because some preliminary results can be compared with the analytical solution. The aluminum plate has dimension 15 in. \times 12 in. \times 0.040 in. (38.1 cm \times 30.48 cm \times 0.1016 cm). The material properties are Young's modulus $E = 10.587 \times 10^6$ psi (73 GPa), density $\rho = 2.588 \times 10^{-4}$ lbf-sec²/in.⁴ (2763 kg/m³), Poisson ratio $\nu = 0.30$. A constant modal damping ratio of $\zeta_r = 0.02$ is applied. The panel is modeled with a convenient 32×32 mesh (1024 BFS elements). The lowest twenty-two natural frequencies and corresponding modes are given in Table 2.

Table 2. Lowest twenty-two S-S panel modes and frequencies in Hz (32×32 mesh)

Mode	(1,1)	(2,1)	(1,2)	(2,2)	(3,1)	(1,3)	(3,2)	(4,1)	(2,3)	(4,2)	(3,3)
FEM	43.8	95.07	123.9	175.2	180.5	257.5	260.7	300.2	308.7	380.4	394.2
Analytical	43.8	95.1	123.9	175.2	180.5	257.4	260.7	300.2	308.7	380.3	394.2
Mode	(1,4)	(5,1)	(2,4)	(4,3)	(5,2)	(3,4)	(6,1)	(5,3)	(1,5)	(4,4)	(6,2)
FEM	444.4	454.0	495.7	513.8	534.1	581.1	642.1	667.7	684.8	700.8	722.2
Analytical	444.4	454.0	495.7	513.8	534.1	581.1	642.0	667.7	684.7	700.8	722.1

The number of modal coordinates to be included in the analysis for converged deflection and stress is studied first. The RMS maximum non-dimensional deflection (W_{max}/h) and the RMS maximum stress (σ_y at the plate center) for different number of modes under a synchronized random load of intensity SPL=100 dB are given in Table 3. Analytical solutions (section II) for 1, 2, 4 and 5 symmetric modes are also tabulated for validation of the present modal Finite Element Model (FEM).

Table 3. Verification and modal convergence for S-S panel under synchronized loading (32×32 mesh)

SPL=100 dB Modes	Analytical RMS (W_{max}/h)	Analytical RMS(Stress) psi	FEM RMS (W_{max}/h)	FEM RMS(Stress) psi
(1,1)	0.6219	473.105 (3.26 MPa)	0.6220	474.472 (3.27 MPa)
(1,1), (3,1)	0.6227	475.043 (3.28 MPa)	0.6227	476.690 (3.28 MPa)
(1,1), (3,1), (1,3), (3,3)	0.6228	483.010 (3.33 MPa)	0.6229	485.220 (3.35 MPa)
(1,1), (3,1), (1,3), (3,3), (5,1)	0.6228	483.070 (3.33 MPa)	0.6230	484.950 (3.34 MPa)
Lowest 4 modes	0.6219	473.105 (3.26 MPa)	0.6220	474.472 (3.27 MPa)
Lowest 5 modes	0.6227	475.090 (3.28 MPa)	0.6227	476.690 (3.28 MPa)
Lowest 11 modes	0.6228	483.010 (3.33 MPa)	0.6229	485.220 (3.35 MPa)
Lowest 13 modes	0.6228	483.070 (3.33 MPa)	0.6230	484.950 (3.34 MPa)

Results show that the lowest four symmetric modes (1,1), (3,1), (1,3), and (3,3) are sufficient for a converged displacement and stress solutions, and that the asymmetric modes (2,1), (1,2), (2,2), (3,2), (4,1), (2,3), (4,2), (1,4) and (5,1) have no appreciable contribution to the maximum displacement response. The modal convergence based on stress also indicated that four symmetric modes are sufficient for converging stress response. Since the present paper deals with fatigue life predictions, which are based

on stress ranges, equation (17), four symmetric modes are considered for converged stress calculations. In the RMS calculations, the transient part of the responses has been omitted by dropping the first 8192 data points or 0.125 second (sec). This means that the total useful time of data is 0.875 sec for each sample. This same procedure is adopted for all subsequent results in the paper. Fatigue life prediction results are obtained by evaluating the mean of the RMS values of ten samples.

Two other considerations for accurate and converged response predictions were also addressed: the number of elements and the integration time step. It is found that a discretization of the panel into 1024 BFS elements is more than adequate since 384 elements (24×16 mesh) should be sufficient for converged responses. The selection of the time step has observed two criteria: 1) the Nyquist-Shannon sampling theorem, which basically states that it is necessary to sample a time sequence at least two times faster than the highest frequency present in the modal expansion (394.18 Hz), and 2) two consecutive time steps ($\Delta t_2 = \Delta t_1/2$), for a same pressure load, should give identical time history responses. It was found that a time step of $\Delta t = 1/2^{16} = 1.52 \times 10^{-5}$ sec satisfies the above two requirements.

4.2. Unsynchronized Response of Simply Supported Panel.

The same panel (32×32 mesh) was subjected to an unsynchronized sample random pressure load by the procedure described in section III.D. Results in this section are obtained from a unique random load file containing 1024 uncorrelated random pressure loads for the $32 \times 32 = 1024$ elements. This means that RMS values are always calculated from the same random load file (always same ISEED numbers), and can consequently be used for modal and mesh convergence purposes. However, since the RMS values are based on only one load sample their accuracy (RMS values) cannot be considered as accurate. As it will be explained in a later section, the accuracy is improved by applying the MCS technique by taking many samples. Table 4 shows the RMS values of the maximum stress computed from different mesh sizes. It is observed that a stress mesh convergence is not obtained by a mesh refinement of 32×32 , which is the maximum mesh size that a Dell Precision 450 (Intel Xeon processor 533 MHz) with 4GB of ram memory could model. This limitation could be

Table 4. Mesh and modal convergence for stress of S-S panel under unsynchronized loading

Mesh Size	16 × 16 mesh RMS(Stress), psi	24 × 20 mesh RMS(Stress), psi	32 × 32 mesh RMS(Stress), psi
Lowest 11 modes	84.34 (0.582 MPa)	62.65 (0.432 MPa)	17.62 (0.121 MPa)
Lowest 18 modes	84.77 (0.585 MPa)	62.82 (0.433 MPa)	17.78 (0.123 MPa)
Lowest 20 modes	87.97 (0.607 MPa)	64.37 (0.444 MPa)	19.14 (0.132 MPa)
Lowest 22 modes	87.97 (0.607 MPa)	64.37 (0.444 MPa)	19.14 (0.132 MPa)

overcome by the use of Parallel Computing Methods (PCM), but it will not be addressed in this paper. The main goal of the present work is to show the reduction in RMS responses and increase in fatigue life prediction due to the unsynchronized characteristics of the random load. However, it was observed that 20 modes were sufficient for modal convergence. Consequently, unsynchronized random results will

be limited to a 32×32 mesh size with 20 modes, where the highest two modes are (5,3) with a frequency of 667.65 Hz, and (1,5) with frequency 684.74 Hz, respectively. These two modes indicate that the 32×32 mesh scheme is adequate for numerical simulation.

In order to show the contribution from asymmetric modes other than the lowest four symmetric modes (1,1), (3,1), (1,3), and (3,3), the deflection and stress PSD plots at $x = 15/4$ in. and $y = 12/4$ in., and at the center of the panel for the synchronized and unsynchronized loads at SPL=100 dB are shown in Figure 2. The displacement figure at $x = 15/4$ in. and $y = 12/4$ in. ($x = 38.1/4$ cm & $y = 30.48/4$ cm) clearly indicates that the unsynchronized loading case excited the modes (2,1), (1,2), and (2,3) in addition to the lowest five symmetric modes. A close observation reveals that the mode (4,1) is also excited, but it does not appear on the PSD since the analysis is at the node point for mode (4,1). Stress PSD at $x = 15/4$ in. and $y = 12/4$ in. ($x = 38.1/4$ cm & $y = 30.48/4$ cm) shows that at this location the stress is still influenced by the symmetric modes (3,1) for the synchronized loading case, while for the unsynchronized case the contribution from the of symmetric and asymmetric modes, (2,1), (1,2), (4,1), is more or less evenly distributed. Finally, the stress PSD indicates that the area under the curve ($\text{Power} = S_0 \times \Delta f$) is much lower for the unsynchronized than for the synchronized load case. This implies that the fatigue life would then be higher for the unsynchronized loading case [17].

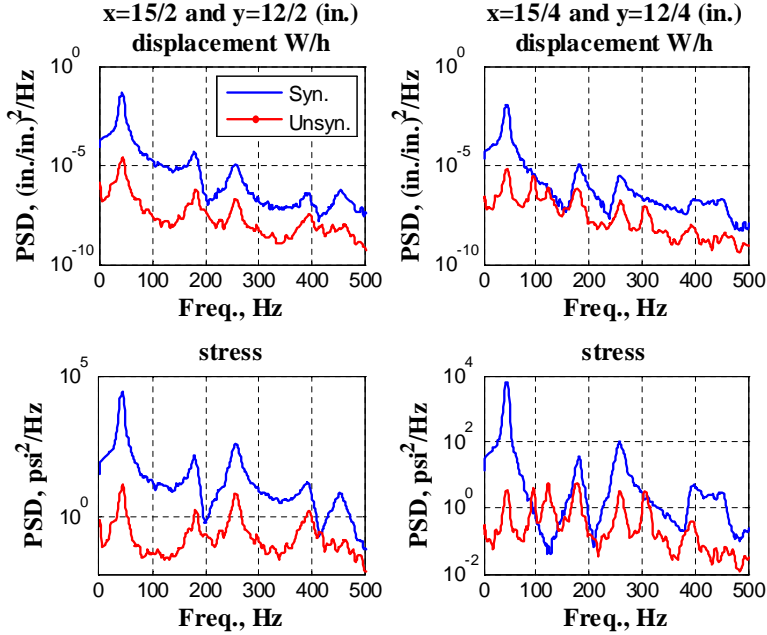


Figure 2. Displacement and stress PSD for synchronized and unsynchronized loads at $x = 15/2$ in. and $y = 12/2$ in. and $x = 15/4$ in. and $y = 12/4$ in.

4.3. Panel Fatigue Life under Synchronized and Unsynchronized Loads.

The MCS technique is adopted for the accurate prediction of fatigue life of panels under random synchronized and unsynchronized processes. The MCS consists of taking a number of various samples of load pressure distribution and evaluate the RMS maximum stress response of each sample at a time. With the results from many samples, a statistical distribution is obtained and used to find a mean value of the RMS responses. Fatigue life results are based on 10 samples of 1 sec. each where the first 0.125 sec. has been discarded to eliminate the initial transient response. The MCS technique has been proven to be effective for synchronized loadings where a small number of samples (based on one random ISEED number for each sample and all finite elements) yield pretty quickly to a converged fatigue estimate. However, the convergence for the unsynchronized loading case (each of the $32 \times 32 = 1024$ elements is excited by a different ISEED number) has shown to be extremely slow and computationally costly. This issue again makes the unsynchronized problem suitable for PCM where the simulated random load (different ISEED) could be distributed among different nodes (processors) instead of just one.

Table 5. Fatigue life prediction for simply-supported panel (10 samples)

SPL=100 dB	Synchronized	Unsynchronized
Fatigue Life Prediction (years)	85.47	8.97×10^7 (Infinity)

Fatigue results shown in Table 5 are based on the maximum bending stress with S-N properties of $\beta = 4.8$ and $K = 1.52 \times 10^{25}$. These fatigue life prediction results

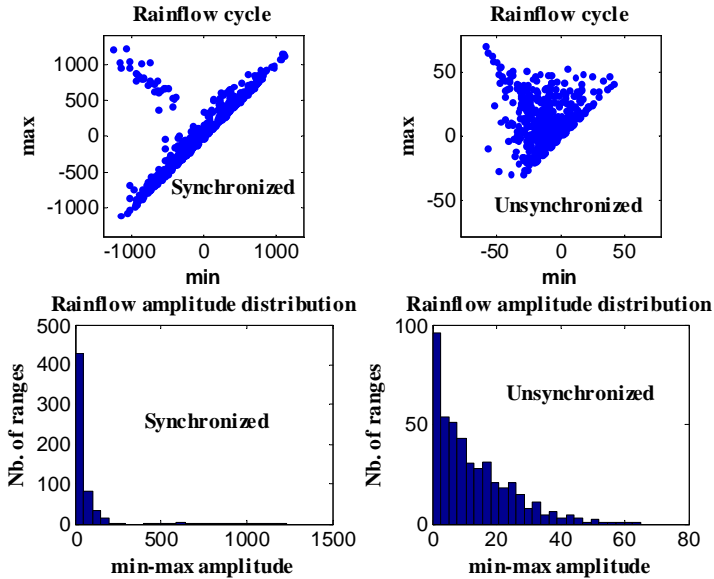


Figure 3. Rainflow cycle and rainflow amplitude distributions for synchronized and unsynchronized loads

suggest the following two questions: 1) is the traditional synchronized random analysis too conservative for structures subjected to highly unsynchronized loads, and 2) if the SPL is high enough to require a nonlinear analysis for synchronized loads, would it be valid just to consider the linear analysis for highly unsynchronized loads at high SPL since their responses might be within the linear range? Certainly, much more investigations are needed for the unsynchronized loading cases at higher SPL including the consideration of nonlinear large deflection effects.

For the synchronized load, the maximum stress is at the panel center, whereas for the unsynchronized the maximum stress alternated between the center node (No. 481) and its eight adjacent nodes (449, 450, 451, 480, 482, 511, 512, 513). Figure 3 gives more detailed information about the characteristics of the stress responses yielding to the fatigue results in Table 5. The differences shown in both figures are an indication on how the stress response differs as a result of synchronized versus unsynchronized loading. This means that even if both responses were obtained from the same SPL=100 dB, their fatigue characteristics are quite different due to the different stress min-max/rainflow amplitude distributions. For instance, the horizontal coordinate axis in the min-max amplitudes figures clearly indicates that the min-max amplitudes for the unsynchronized case are about a fourth of the min-max amplitudes for the synchronized loading case. Consequently, higher fatigue life prediction is expected for the unsynchronized case as shown in Table 5.

4.4. Unsynchronized Response of Panel with Clamped-Simply Supported Boundary Conditions.

A clamped-simply supported (C-SS-SS-C) plate clamped on edges $x=0$ and $y=0$, and simply supported on edges $x=15$ in. and $y=12$ in. ($x=38.1$ cm & $y=30.48$ cm), with similar geometrical and material properties as in the previous section, is studied next. Figure 4 shows the first twenty-two unsymmetrical natural modes normalized with respect to the thickness, $h=0.04$ in. (0.1016 cm), with their corresponding frequencies using a 24×20 mesh (480 elements). In order to reduce the computational time, results in this section are obtained from a mesh size of 24×20 , which is adequate for 20 modes.

For the plate with mixed boundary conditions under synchronized or unsynchronized load for which no closed-form solution is readily available or exists, the most suitable approach is the MCS. For both loading conditions, the location of maximum displacement is situated approximately 8.75 inches (22.225 cm) away from the short clamped edge and 5.4 inches (13.716 cm) away from the long clamped edge (element 278 or node 243).

The MCS for modal and mesh convergence of the unsynchronized loading case is numerically tedious and computationally costly, since each plate element is excited by a different random load or ISEED number at each of the ten-sample runs. This means that 480 pressure time histories with each time history containing 2^{16} points must be generated prior to the numerical integration. For the numerical simulation a

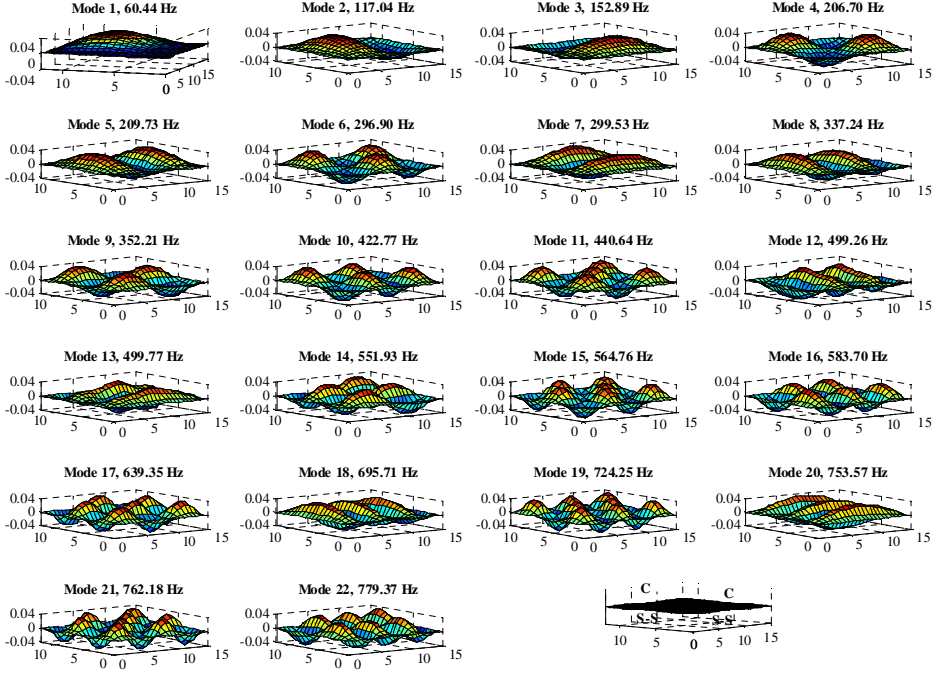


Figure 4. C-SS-SS-C panel modes and frequencies

sample run for unsynchronized loading on a 24×20 mesh with twenty-two modes and $\Delta t = 1/2^{16}$ sec. took approximately 12 hours. The maximum stress is located along the long clamped edge at the node perpendicular to the maximum displacement. For the 24×20 mesh, this corresponds to element 14 or node 13. The stress for the C-SS-SS-C panel was found to be very sensitive to the location of the maximum curvature $\{\kappa\}$ which varies considerably with the mesh size.

Figure 5 presents the PSD of the maximum displacement (element 278 or node 243), and at the maximum stress (element 14 or node 13) for both synchronized and unsynchronized loading cases. The synchronized response results were generated using ISEED=12357 yielding to an RMS (W_{max}/h) of 0.410, and RMS stress value of 477.49 psi (3.292 MPa).

A first trial analysis of displacement PSD indicated that 6 asymmetric modes for the synchronized and 8 asymmetric modes for the unsynchronized loading cases were required for converged displacement responses. A refined analysis showed that more asymmetric modes contributed to both responses but that they did not appear in the PSD because their mode shapes were close to zero at that location (node 243). A clear example is given by mode 2 (117.04 Hz)

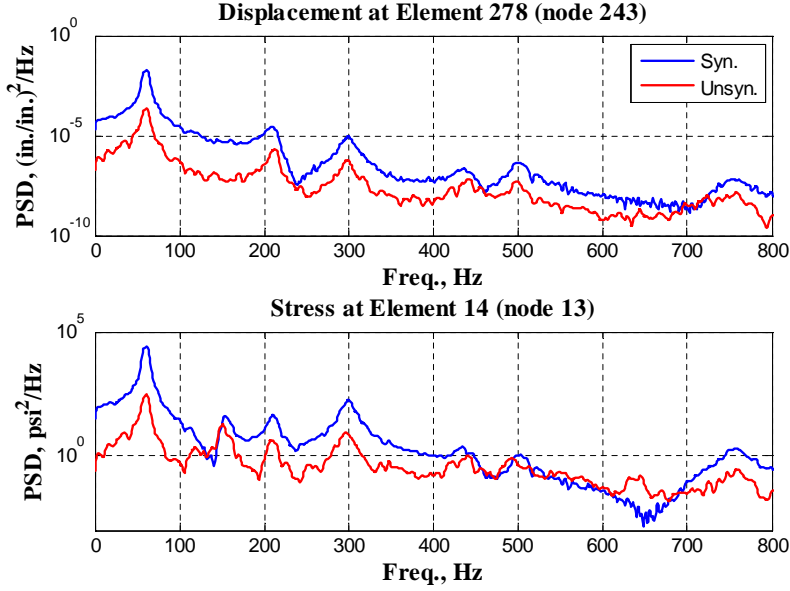


Figure 5. Maximum displacement and stress PSD for synchronized and unsynchronized loads.

A first trial analysis of displacement PSD indicated that 6 asymmetric modes for the synchronized and 8 asymmetric modes for the unsynchronized loading cases were required for converged displacement responses. A refined analysis showed that more asymmetric modes contributed to both responses but that they did not appear in the PSD because their mode shapes were close to zero at that location (node 243). A clear example is given by mode 2 (117.04 Hz) in Fig. 4, where the figure reveals that at node 243 its modal contribution is very small or zero. It is observed for the stress PSD that more modes (peaks) appear for the unsynchronized than for the synchronized loading.

Table 6. Fatigue life prediction for C-SS-SS-C panel (10 samples)

SPL=100 dB	Synchronized	Unsynchronized
Fatigue Life Prediction (years)	77.42 (Infinity)	10.55×10^5 (Infinity)

Fatigue lives shown in Table 6 are predicted at node 13 where the stress is the highest and most critical. Results are based on the mean value of the fatigue life of ten samples.

5. CONCLUSION

The present work has studied the RMS responses of a simply supported and a clamped-simply supported panel subjected to synchronized and unsynchronized loading, respectively. Classic analytical solutions of the random responses are generally

confined to simple boundary conditions where the mode shape solutions are known. Even in those simple cases, response solutions have neglected the asymmetric modes for the synchronized case due to mathematical limitations. The present work has shown for the first time that panels under unsynchronized loads excite both symmetric and asymmetric modes, and that the unsynchronized load characteristics lower the RMS values and increase the fatigue life predictions.

These conclusions appear to be quite intuitive but they are a first attempt to explore and understand the real loading conditions. It is likely that real random pressure excitation characteristics are neither fully spatially correlated nor uncorrelated. In such case developing a procedure applicable for analysis with an arbitrary spatial input correlation is deemed an important part of future work. In addition, in order to verify these conclusions, more simulation studies and further experimental data of structures subjected to uniform random pressure loads that are unsynchronized in time are needed.

The computational burden encountered in solving the unsynchronized loading case required the necessity of considering Parallel Computing Methods (PCM). Parallel computing methods greatly reduce the computational time by splitting the load generation into multiple processors (nodes).

REFERENCES

1. ARNOLD, R. R. and VAICAITIS, R. R.: *Nonlinear Response and Fatigue of Surface Panels by the Time Domain Monte Carlo Approach*, WRDC-TR-90-3081, Wright Laboratory, WPAFB, OH, May 1992.
2. MEI, C. and WOLFE, H. F.: On large deflection analysis in acoustic design, in *Random Vibrations – Status and Recent Developments*. The Stephen H. Crandall Festschrift, Editors: I. Elishakoff and R. H. Lyon, Elsevier Applied Science Publishers, Amsterdam 1986, 279-302.
3. MEI, C., DHAINAUT, J. M., DUAN, B., SPOTTSWOOD, S. M. and WOLFE, H. F.: *Nonlinear Random Response of Composite Panels in an Elevated Thermal Environment*, AFRL-VA-WP-TR-2000-3049, Air Force Research Laboratory, WPAFB, OH, October 2000.
4. MCEVAN, M. J., WRIGHT, J. R., COPPER, J. E. and LEUNG, A. Y. T.: A finite element/modal technique for nonlinear plate and stiffened panel response prediction. AIAA 2001-1595, 42nd Structures, Structural Dynamics and Materials Conference, Seattle, WA, April 2001 (CD-ROM).
5. RIZZI, S. A. and MURAVYOV, A. A.: Improved equivalent linearization implementations using nonlinear stiffness evaluation. NASA TM-2001-210838, March 2001.
6. MURAVYOV, A. A. and RIZZI, S. A.: Determination of nonlinear stiffness with application to random vibration of geometrically nonlinear structures. *Computers and Structures*, **81**(15), (2003), 1513-1523.
7. DHAINAUT, J. M. and Mei, C.: Nonlinear response and fatigue life of isotropic panels subjected to nonwhite pressure fluctuations. AIAA 2002-1635, 43rd Structures, Structural Dynamics, and Materials Conference, Denver, Colorado, April, 2002, 22-25.

8. PRZEKOP, A., GUO, X., AZZOUZ, S. and MEI, C.: Reinvestigation of nonlinear random response of shallow shells using finite element modal formulation. AIAA 2004-1553, 45th *Structures, Structural Dynamics and Materials Conference*, Palm Spring, CA, April 2004 (CD-ROM).
9. MEI, C. and WENTZ, K. R.: Analytical and experimental nonlinear response of rectangular panels to acoustic excitation. AIAA 82-0733, 23rd *Structures, Structural Dynamics and Materials Conference*, New Orleans, LA, May 1982, 514-520.
10. HOLLKAMP, J. J., GORDON, R. W. and SPOTTSWOOD, S. M.: Nonlinear sonic fatigue response prediction from finite element modal models: A comparison with experiments. AIAA 2003-1709, 44th *Structures, Structural Dynamics and Materials Conference*, Norfolk, VA, April 2003 (CD-ROM).
11. BOGNER, F. K., FOX, R. L. and SCHMIDT, L. A.: The generation of inter-element compatible stiffness and mass matrices by the use of interpolation formulas. *AFFDL-TR-66-80*, Wright-Patterson AFB, OH, 1996, 396-443.
12. BARLOW, J.: Optimal stress locations in finite element models. *International Journal for Numerical Methods in Engineering*, **10**, (1976), 243-251.
13. MINER, M. A.: Cumulative damage in fatigue. *Journal of Applied Mechanics*, **12**, (1945), 159-164.
14. LANGLEY, R. S. and MCWILLIAM, S.: Mathematical models for structural reliability analysis. F. Casciati and B. Roberts (eds), *CRC Press*, July 1996, 333-334.
15. DOWLING, N. E.: Fatigue failure predictions for complicated stress-strain histories. *Journal of Materials*, **7**, (1972), 71-87.
16. *WAF0 - A Matlab Toolbox for Analysis of Random Waves and Loads*, Version 2.0.02, Lund Institute of Technology, Lund University, 2000.
17. BISHOP, N. W. N. and SHERRATT, F.: A theoretical solution for the estimation of rain-flow ranges from power spectral density data. *Fatigue Fracture Engineering Material Structures*, **13**(4), (1990), 311-326.

REINFORCEMENT OF INNER AND OUTER CIRCULAR FAILURES OF PIPES BY TEXTILE COMPOSITE LAYERS

BALÁZS PERE, JÁNOS ÉGERT AND TAMÁS SZABÓ
Department of Applied Mechanics, Széchenyi István University,
Egyetem tér 1., 9026 Győr, Hungary
perebal@sze.hu, egert@sze.hu, sztamassze.hu

[Received: September 15, 2008]

Abstract. The first part of the paper deals with the FEM computation of deformations, stresses and strain in the surrounding area of inner and outer circular artificial failures with a set of given geometrical dimensions in steel pipelines. For the investigation of this problem three groups of mechanical models are applied: multilayered elastic shell, 3D elastic solid and 3D elastic-plastic solid FEM models. The aim of this analysis is to clarify the case in which the pipeline fails. When a pipe fails and needs repair or reinforcement, this is called critical case.

In the second part of the paper the repaired pipes are investigated. For repairing of the inner and outer failures, inner or outer multilayered textile composite reinforcements are applied by winding technology. The task is to determine the width of the reinforcement and the number of layers needed for repair.

The different mechanical models (multilayered elastic shell, 3D elastic solid and 3D elasto-plastic solid) are compared on the basis of numerical results. The critical cases are determined and the questions of repair are answered also numerically.

Keywords: Steel pipeline, artificial circular damage, textile composite reinforcement, FEM analysis, elastic shell and 3D elastic-plastic modelling

1. INTRODUCTION

Oil and gas pipelines often have inner and outer circular failures. The inner failures usually originate from welding on location, and the outer failures result from any other violent outer effect, for instance due to agricultural equipment working above the pipeline.

The first task is to predict the risk caused by these circular failures. In the first step one needs to clarify the deformations, stresses and strains around the damaged part of the pipe. On the basis of such analysis one can find critical cases in which repairs are needed.

The second task is to fix or to repair the damaged pipe. In this paper an inner or outer multilayered textile composite reinforcement are applied at the location of the failures. The multilayered textile composite reinforcement is made by winding technology. During design of this composite reinforcement the width and the number

of layers of the winding should be determined. The failures are considered to be fixed when stresses are below the critical values both in the steel pipe and in the composite reinforcement.

The numerical aspects of both tasks are discussed in this paper. In the first step two kinds of circular damaged pipe-parts using the finite element method and the I-DEAS program code are investigated. The failures may have a high number of varieties therefore two typical artificial failure geometries are chosen. On the basis of the numerical analysis the critical cases have been determined in which repairs are needed. In the second step an inner and/or outer composite reinforcement with different widths and numbers of layers are applied for the critical cases. When analyzing critical cases the proper width and number of layers of reinforcement can be found.

2. GEOMETRY OF TYPICAL ARTIFICIAL FAILURES AND REINFORCEMENTS

Figure 1 shows the global geometry i.e. the location of the investigated inner and outer circular failures.

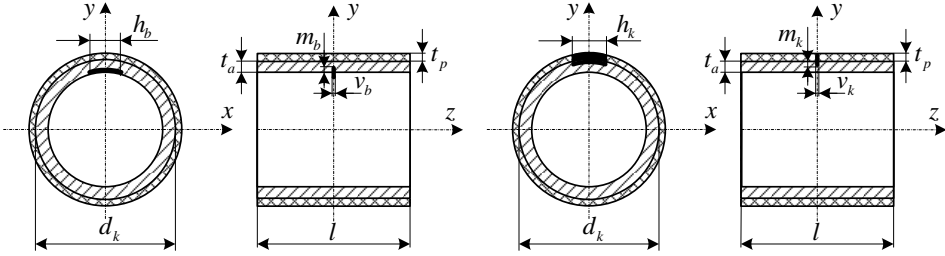


Figure 1. Global geometry of the inner and outer circular failures

The steel pipe's outer diameter is $d_k = 323,9$ mm, its wall thickness $t_a = 7,1$ mm and the length of the investigated pipe part is $l = 2000$ mm. The steel pipe is coated with a $t_p = 3,12$ mm thick polyethylene insulation layer against corrosion. The longitudinal dimension of circular failures are $h_b = h_k = 150$ mm for both inner and outer cases, the width is $v_b = 1,5$ mm for the inner case and $v_k = 2$ mm for the outer case. There are three depth versions $m_b = m_k = 2; 4; 6$ mm investigated.

Figure 2 shows the the local geometry of analyzed inner and outer circular failures. The geometry of artificial failures (Figure 2) are assumed to be reproduced easily for the planned experiments.

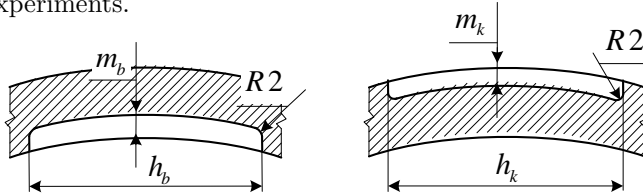


Figure 2. Local geometry of the inner and outer circular failures

An inner and outer circular failures of pipes can be reinforced theoretically from the outside or the inside as well. Figure 3 shows the reinforcement possibilities for an inner failure. At the location of the failure the anti-corrosion layer is removed and the reinforcement is wound directly to the steel surface.

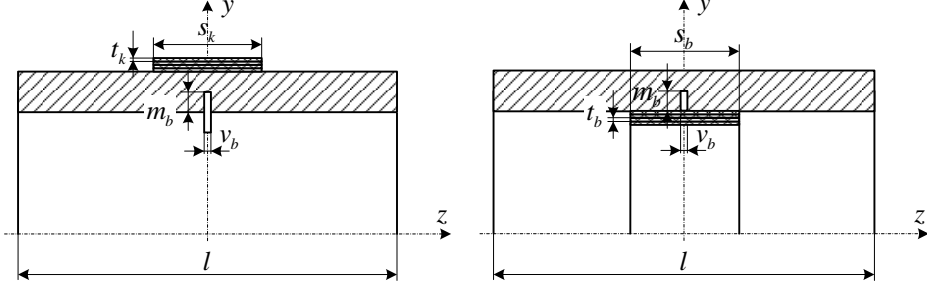


Figure 3. Reinforcement versions for the inner circular damage

The layer thickness of reinforcement in each case is the same $t_k = t_b = 0,3$ mm, and three different widths of the winding bands are investigated $s_k = s_b = 50; 100; 200$ mm.

3. MECHANICAL MODELLING OF THE MATERIALS AND WORKING CONDITIONS

The pipe is made of steel, the protecting layer against corrosion is polyethylene and the material of the reinforcement is carbon fiber textile reinforced plastics (CFRP). In mechanical point of view the steel and the polyethylene are modelled as linear elastic materials given by two material constants and the limit of elasticity. These material parameters in Table 1 are measured by the Department of Mechanical Technology of Miskolc University [7].

Table 1. Material constants and ultimate stress values

Material	E [MPa]	ν [-]	$R_{t0,5}$ [MPa]	R_m [MPa]
Steel	205 000	0,3	499	603
Polyethylene	527	0,31	—	12,8

In Table 1 E is the modulus of elasticity, ν is the Poisson's ratio, $R_{t0,5}$ is the yield limit and R_m is the breaking strength of material.

In linear elastic, isotropic, plane stress problems the following Hooke's law provides the constitutive equations:

$$\begin{bmatrix} \varepsilon_1 \\ \varepsilon_2 \\ \gamma_{12} \end{bmatrix} = \begin{bmatrix} \frac{1}{E} & -\frac{\nu}{E} & 0 \\ -\frac{\nu}{E} & \frac{1}{E} & 0 \\ 0 & 0 & \frac{2(1+\nu)}{E} \end{bmatrix} \begin{bmatrix} \sigma_1 \\ \sigma_2 \\ \tau_{12} \end{bmatrix}, \quad (1)$$

1 and 2 are directions perpendicular to each other in the tangent plane of the middle surface of pipe. $\varepsilon_1, \varepsilon_2$ and σ_1, σ_2 are tensions and normal stresses in directions 1, 2 respectively. γ_{12} and τ_{12} are the in-plane shear strain and the shear stress.

The elasto-plastic computations are carried out by using the stress-strain diagram in Figure 4 given by the Department of Mechanical Technology of Miskolc University [7].

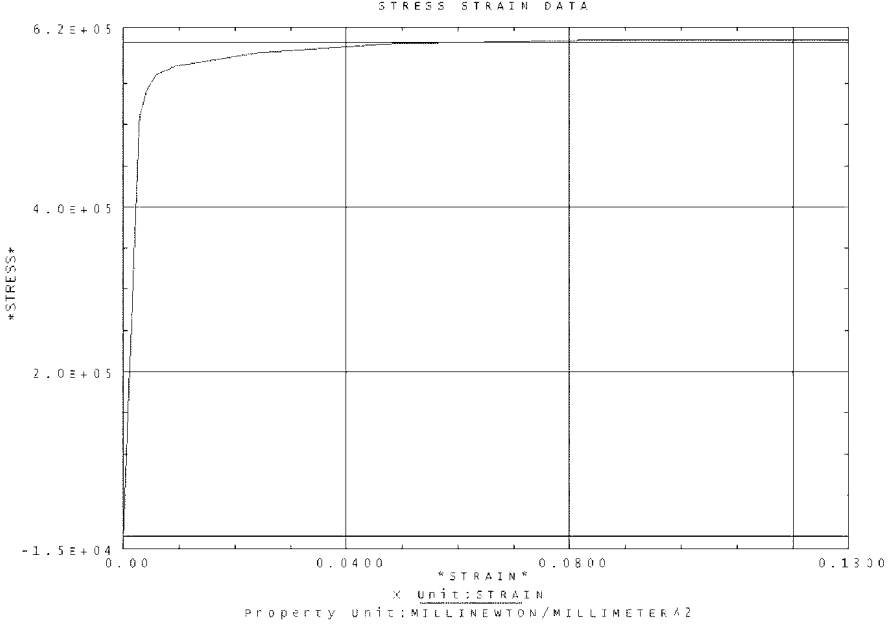


Figure 4. Stress-strain diagram of the steel pipe

For isotropic materials the well known von Mises failure criterium is applied:

$$\frac{1}{2} \left(\frac{1}{R_{t0,5}} \right)^2 \left[(\sigma_I - \sigma_{II})^2 + (\sigma_{II} - \sigma_{III})^2 + (\sigma_I - \sigma_{III})^2 \right] \leq 1, \quad \text{or} \quad (2)$$

$$\sigma_{red\ max} \leq R_{t0,5}, \quad (3)$$

where $\sigma_I, \sigma_{II}, \sigma_{III}$ are the principal stresses.

According to references [1], [2], the carbon fiber textile reinforced composite can be modelled from macroscopic point of view by an orthotropic constitutive law:

$$\begin{bmatrix} \varepsilon_1 \\ \varepsilon_2 \\ \gamma_{12} \end{bmatrix} = \begin{bmatrix} 1/E_1 & -\nu_{12}/E_2 & 0 \\ -\nu_{21}/E_1 & 1/E_2 & 0 \\ 0 & 0 & 1/G_{12} \end{bmatrix} \begin{bmatrix} \sigma_1 \\ \sigma_2 \\ \tau_{12} \end{bmatrix}, \quad (4)$$

In the above equations the indices 1, 2 stand for the principal material direction of CFRP. In the constitutive law E_1, E_2 are orthotropic moduli of elasticity, ν_{12}, ν_{21} are Poisson's ratios and G_{12} is the independent in-plane shear modulus. The Poisson's ratios are not independent from each other and due to energy reasons [2] the following relation exists :

$$\frac{\nu_{12}}{E_2} = \frac{\nu_{21}}{E_1}. \quad (5)$$

Macroscopic modelling means that equations are not appropriate to determine stresses and strains in the carbon fibers or in the matrix material, but do well for a larger area with a lot of fibers. Therefore, the above stresses and strains are the average features of an area with a lot of fibers.

For the orthotropic material the Tsai-Wu's failure criterium is applied:

$$\frac{\sigma_1^2}{\sigma_{H1}\sigma_{D1}} + \frac{\sigma_2^2}{\sigma_{H2}\sigma_{D2}} - \frac{\sigma_1\sigma_2}{\sqrt{\sigma_{H1}\sigma_{D1}\sigma_{H2}\sigma_{D2}}} + \frac{\tau_{12}^2}{\tau_{S12}^2} + \left(\frac{1}{\sigma_{H1}} - \frac{1}{\sigma_{D1}}\right)\sigma_1 + \left(\frac{1}{\sigma_{H2}} - \frac{1}{\sigma_{D2}}\right)\sigma_2 \leq 1, \quad (6)$$

or

$$K_{tw} \leq 1, \quad (7)$$

where σ_{H1}, σ_{H2} are tensile, σ_{D1}, σ_{D2} are compressive and τ_{S12} is shear strengths.

Table 2 contains the measured material constants and ultimate stress values of the applied CFRP measured by the Department of Polymer Engineering of the Budapest University of Technology [8].

Table 2. Material constants and ultimate stress values of CFRP layers

Thickness [mm]	E_1 [MPa]	E_2 [MPa]	ν [-]	G_{12} [MPa]
0,3	47 600	45 000	0,036	2 000
σ_{H1} [MPa]	σ_{H2} [MPa]	σ_{D1} [MPa]	σ_{D2} [MPa]	σ_{S12} [MPa]
436	430	310	340	76

The deformations, stresses and strains in the damaged pipe and in the reinforced pipe are determined for two loading cases, i.e. for a normal working condition and for an experimental loading, where it is possible to measure by gauges.

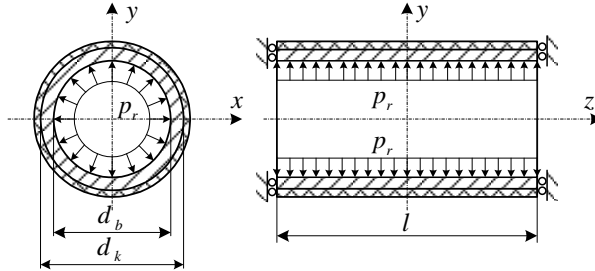


Figure 5. Mechanical model for normal working condition

In normal working conditions the pipeline is embedded in the earth which does not allow the longitudinal displacements of the investigated pipe parts. This is the reason why the mechanical model is clamped at both ends of the pipe part in the normal working loading case. There is a $p_r = 63$ bar inner pressure in both loading cases in the pipe.

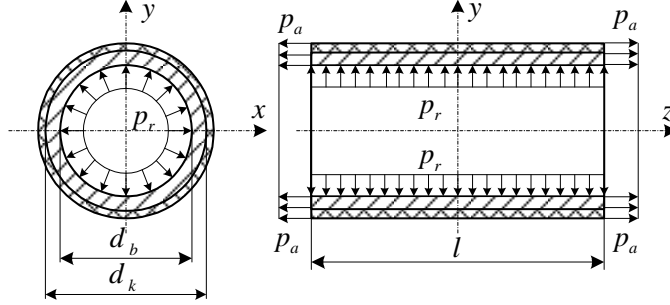


Figure 6. Mechanical model for experimental checking

In the experiments the investigated pipe part is closed at both ends. The inner pressure provides an $p_a = d_b^2 p_r / (d_k^2 - d_b^2)$ additional axial loading because of the closed ends. Therefore the experimental loading case consists of the inner pressure and the axial loading.

4. FINITE ELEMENT APPROACHES AND MESHES

For computation of deformations, stresses and strains around the circular failures the following three models are applied: multilayered elastic shell, 3D elastic solid and 3D elasto-plastic solid elements. However computations of repaired pipes are carried out only by multilayered elastic shell elements.

By using layered shell elements it is possible to model failures by proper choice of layer thicknesses. Figure 7 shows two cases for the proper thickness choice. The left one is at a common location of the pipe and the right one is at an inner failure with 4 mm depth. In both cases in Figure 7 the upper layer represents the insulation and two inner layers for modelling the inner failure are shown in the right picture. Naturally, for the failure area zero values should be given for material constants.











Thickness	Angle	Ply		Material	Thickness	Angle	Ply		Material
3.12	+0	5		INSULATION	3.12	+0	5		INSULATION
1.1	+0	4		STEEL	1.1	+0	4		STEEL
2	+0	3		STEEL	2	+0	3		STEEL
2	+0	2		STEEL	2	+0	2		FAILURE
2	+0	1		STEEL	2	+0	1		FAILURE

Figure 7. Modelling of failure thickness by multilayered shell elements

Figure 8 shows two cases for the proper thickness choice of layers at reinforcement. The left and right pictures represent the thicknesses of layers in undamaged and damaged locations, respectively.

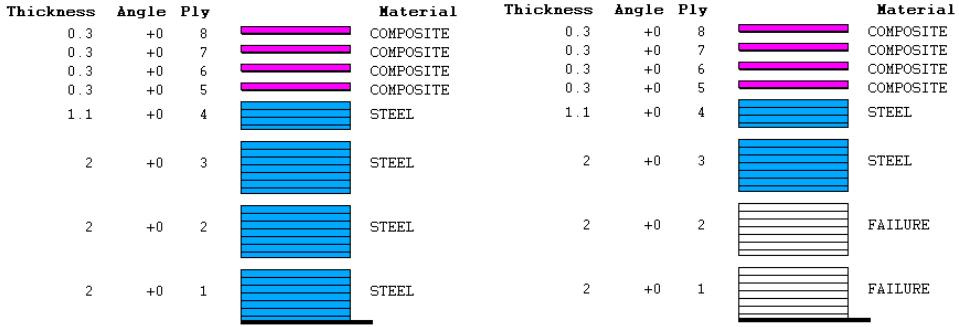


Figure 8. Modelling of reinforcement and failure thickness by shell elements

Using multilayered shell elements it is only possible to apply a sharp corner approach for failures, so the R2 mm rounding in Figure 2 is not taken into consideration at shell modelling.

The 3D modelling allows a very accurate approach of real geometry of artificial inner and outer failures, even an R2 mm rounding.

Table 3. Characteristic data for FEM meshes

	Shell model	3D solid model
Number of elements	5 000	17 500
Number of nodes	15 000	36 000

Table 3 includes the characteristic data of applied meshes. The nodes of shell elements have six degrees of freedom and the nodes of 3D solid elements three, so one has to solve in both tasks a linear algebraic equation system with about 90-108 thousand unknowns. The computations for both shell and 3D solid modelling are carried out also with much denser mesh in order to prove that the applied mesh provides accurate results.

When creating finite element meshes the double symmetry is taken into account. Naturally, the mesh is much denser around the failures than at the other areas of the model in interest of accuracy of computations.

Figure 9 shows a characteristic mesh for a shell model and a mesh part for a 3D solid model. The $l_m = l/2 = 1000$ mm length of mesh is chosen so that the influence of boundary conditions at the end of the pipe part and the influence of the circular failure do not disturb each other.

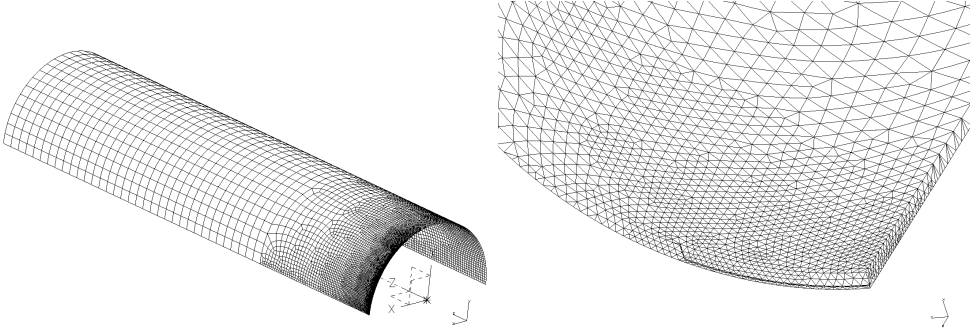


Figure 9. Shell mesh and 3D solid mesh part for circular failure

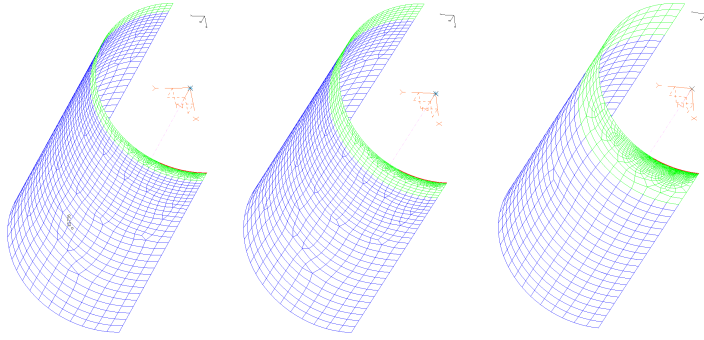


Figure 10. Shell meshes for different reinforcements

On the basis of computational experience it is enough to apply shorter models with $l_r = l_m/2 = 500$ mm length for the computation of reinforced pipe parts. In these meshes one has to take into consideration the width of the reinforcing composite band at meshing (Figure 10.).

5. COMPUTATIONAL RESULTS

5.1. Influence of the insulation layer. The analysis of the influence of the outer polyethylene insulation is carried out only for inner circular failure. Numerical results prove that the insulation layer has no importance from the mechanical point of view, since the stiffness of the insulation layer is negligible compared to the steel's stiffness. Therefore the insulation layer is neglected in the investigations.

5.2. Results for the damaged steel pipes. The character of deformations and stress/strain distributions is similar for both loading cases. However the critical values of deformations, stresses and strains are a little higher for the experimental checking than for the normal loading conditions. This is the consequence of the additional axial loading originated from the inner pressure. This axial loading seems to be a little higher than the axial loading originated from the clamped ends of the pipe

model at normal working conditions. Therefore, only the results of this hazardous experimental loading case are presented in this paper.

Numerical results show that the deformation of pipes with inner failure depends significantly on the depth of failure. Figure 11 demonstrates these differences on the radial displacement distribution of the middle surface. It is very interesting that the maximum deformation occurs not directly at the failure but beside that.

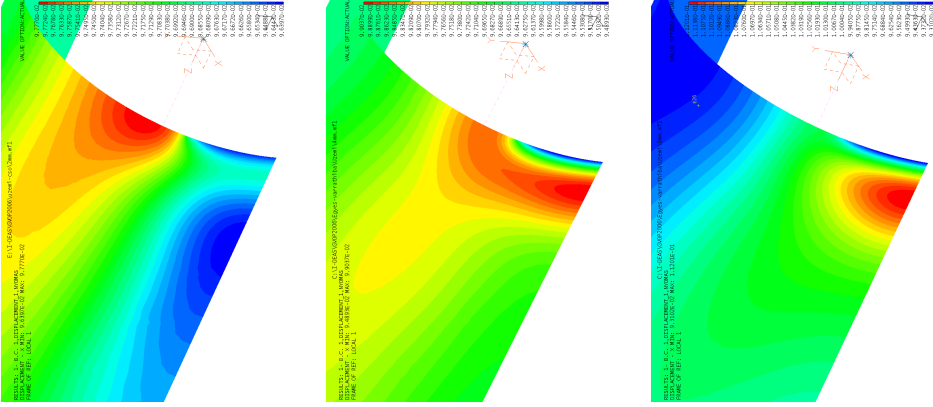


Figure 11. Radial displacements at inner failure with 2, 4 and 6 mm depth

Figure 12 shows the radial displacements in case of outer failure for the three investigated failure depths. In this case the character of deformation does not depend on the depth of outer failure. Naturally, the magnitudes of deformation are different.

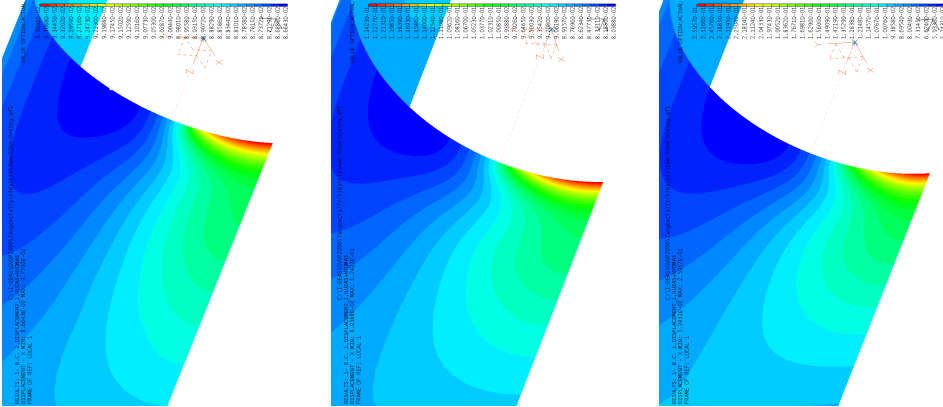


Figure 12. Radial displacements at outer failure with 2, 4 and 6 mm depth

The different character of deformations for inner and outer failure will play a very important role at the repair.

Table 4 summarizes the critical strain and von Mises reduced stress values for the hazardous experimental loading case at inner failure. Comparing the $\varepsilon_{z\ max}$ axial and $\varepsilon_{\varphi\ max}$ circular strains it is seen that they are in the same order of magnitude at lower depths. However the $\varepsilon_{z\ max}$ axial strains become dominant at increasing failure depth. Therefore one can state that the influence of axial loading is dominant for strains around the circular failure at higher depths.

Table 4. Critical values - inner failures - experimental loading case

Depth [mm]	Quantity [Dimension]	Shell model	3D elastic model	3D elasto- plastic model
2	$\varepsilon_{\varphi\ max}$ [1]	$1,2603 \cdot 10^{-3}$	$9,3827 \cdot 10^{-4}$	$9,3827 \cdot 10^{-4}$
	$\varepsilon_{z\ max}$ [1]	$1,0610 \cdot 10^{-3}$	$1,2283 \cdot 10^{-3}$	$1,2283 \cdot 10^{-3}$
	$\sigma_{red\ max}$ [MPa]	222,37	243,03	243,03
4	$\varepsilon_{\varphi\ max}$ [1]	$2,4310 \cdot 10^{-3}$	$8,7135 \cdot 10^{-4}$	$8,7235 \cdot 10^{-4}$
	$\varepsilon_{z\ max}$ [1]	$7,2919 \cdot 10^{-3}$	$2,5820 \cdot 10^{-3}$	$2,5820 \cdot 10^{-3}$
	$\sigma_{red\ max}$ [MPa]	502,38	455,11	455,11
6	$\varepsilon_{\varphi\ max}$ [1]	$2,8736 \cdot 10^{-3}$	$9,3700 \cdot 10^{-4}$	$9,4239 \cdot 10^{-4}$
	$\varepsilon_{z\ max}$ [1]	$3,5439 \cdot 10^{-2}$	$6,7759 \cdot 10^{-3}$	$7,4800 \cdot 10^{-3}$
	$\sigma_{red\ max}$ [MPa]	898,85	1191,4	603,0

The maximum reduced stresses computed by different models are close to each other below the yield stress, in cases of 2 and 4 mm deep inner failures. At 4 mm failure depth the maximum reduced stresses reach or are close to the yield stress value. For 6 mm failure depth every model, including the shell model, indicates the fracture of the pipe. Therefore the damaged pipe needs repair only at 6 mm failure depth.

Table 5. Critical values - outer failures - experimental loading case

Depth [mm]	Quantity [Dimension]	Shell model	3D elastic model	3D elasto- plastic model
2	$\varepsilon_{\varphi\ max}$ [1]	$8,9118 \cdot 10^{-4}$	$9,8610 \cdot 10^{-4}$	$9,8610 \cdot 10^{-4}$
	$\varepsilon_{z\ max}$ [1]	$7,2939 \cdot 10^{-4}$	$1,1496 \cdot 10^{-3}$	$1,1496 \cdot 10^{-3}$
	$\sigma_{red\ max}$ [MPa]	196,39	233,38	233,38
4	$\varepsilon_{\varphi\ max}$ [1]	$1,1614 \cdot 10^{-3}$	$1,1841 \cdot 10^{-3}$	$1,1841 \cdot 10^{-3}$
	$\varepsilon_{z\ max}$ [1]	$2,5196 \cdot 10^{-3}$	$2,7328 \cdot 10^{-3}$	$2,7328 \cdot 10^{-3}$
	$\sigma_{red\ max}$ [MPa]	531,40	490,62	490,62
6	$\varepsilon_{\varphi\ max}$ [1]	$1,4874 \cdot 10^{-3}$	$1,6668 \cdot 10^{-3}$	$1,6706 \cdot 10^{-3}$
	$\varepsilon_{z\ max}$ [1]	$4,8891 \cdot 10^{-3}$	$5,5436 \cdot 10^{-3}$	$7,1033 \cdot 10^{-3}$
	$\sigma_{red\ max}$ [MPa]	1009,7	973,58	603,0

Table 5 summarizes the characteristic critical strain and von Mises reduced stress values for the more hazardous experimental loading case at outer failure. These results show very similar behavior from the point of view of strains and stresses for the outer damaged pipe than for the inner failure. Also the outer damaged pipe needs repair only at 6 mm failure depth.

It is curious that though the deformations are different similar strain and stress values have been obtained for the inner and outer failures.

All the three applied models indicate the fracture of the pipe for the same failure depth. From here on the simplest multilayered shell model is used in the investigation of repaired cases because it needs less numerical efforts than the others.

5.3. Results for the pipes repaired. As it is determined in 5.2 the axial loading becomes dominant at both increasing inner and outer circular failure depths. This dominant loading results very different deformations at inner (Figure 13.) and outer (Figure 14.) failure. The highest radial deformations occur shifted in axial direction nearby the inner failure and exactly in the middle of the outer failure.

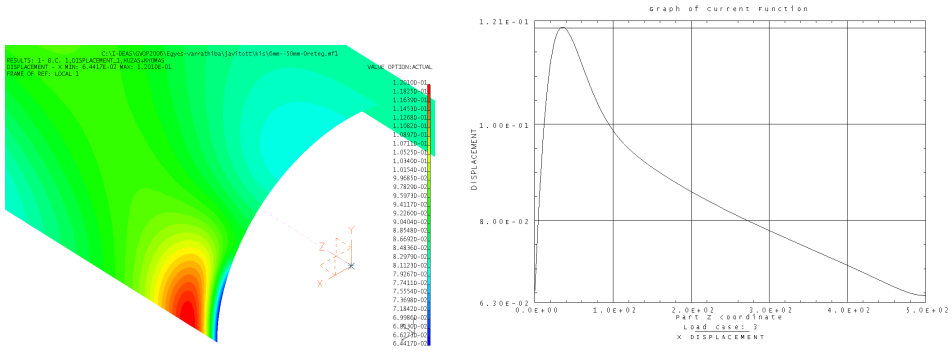


Figure 13. Radial displacements at inner failure with 6 mm depth

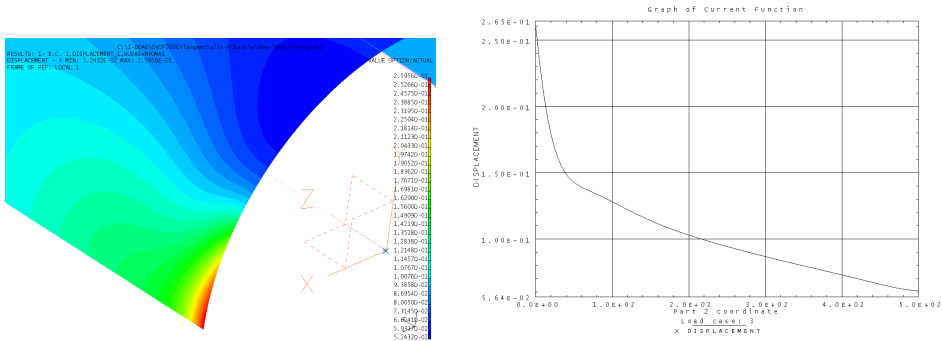


Figure 14. Radial displacements at outer failure with 6 mm depth

The phenomenon can be explained by Figure 15. If there is no failure in the pipe wall the stress resultant over the thickness is only the N_a force. In the undamaged case there is no bending effect in the pipe wall.

However in case of inner failure the stress resultants provide a N_a force and an additional M_{ti} bending moment. This bending moment opens the inner failure and results maximum radial deformations shifted nearby the failure.

In case of outer failure the stress resultants provide a N_a force and an additional M_{to} bending moment. This bending moment also opens the outer failure and results maximum radial deformations in the middle of the failure.

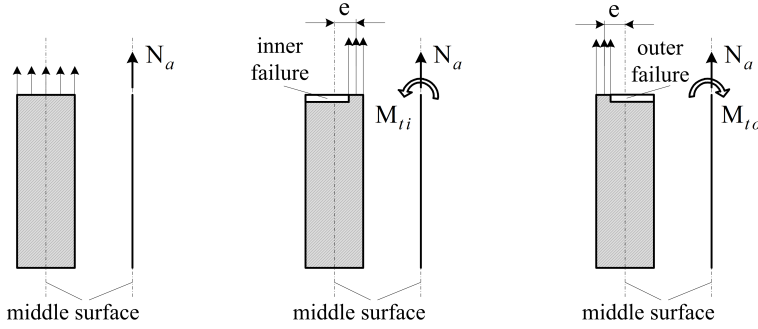


Figure 15. Force and moment resultants at inner and outer failure

Both inner and outer failures can be fixed from the outside or from the inside. Figure 16. shows the repair versions for an inner failure.

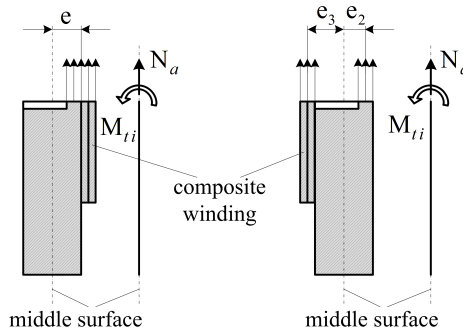


Figure 16. Reparation versions at inner failure

The pipe can be considered as fixed if the $\sigma_{red\ max}$ reduced stresses in the steel wall do not reach the yield stress value (3.3) and the K_{tw} Tsai-Wu failure coefficient in the reinforcement do not reach the value 1 (3.7).

Computations are carried out for repaired inner failure by 50, 100 and 200 mm bandwidth of CFRP layers. The numerical results proved that the bandwidth in this range practically does not influence the behavior of repaired case.

Table 6 summarizes the numerical results for a 6 mm deep inner failure with 50 mm bandwidth reinforcement, in the left two columns for outer reinforcement and in the right two columns for inner reinforcement.

Table 6. Reduced stresses and failure coefficients for inner failure with 6 mm depth

Number of layers/ thickness [mm]	$\sigma_{\text{red max}}^{\text{outer}}$ [MPa]	$K_{\text{tw}}^{\text{outer}}$ [-]	$\sigma_{\text{red max}}^{\text{inner}}$ [MPa]	$K_{\text{tw}}^{\text{inner}}$ [-]
0/0	908	–	908	–
4/1,2	1046,0	0,6137	600,2	0,0641
8/2,4	984,4	0,7704	499,1	-0,0187
12/3,6	804,6	0,4633	–	–
16/4,8	674,1	0,2729	–	–
20/6,0	586,0	0,1909	–	–
24/7,2	523,0	0,1188	–	–
28/8,4	475,5	0,0862	–	–

It can be seen from Table 6 that an inner circular failure can be repaired better by inner reinforcement than by outer one. Both goals for failure criteria (3.3) and (3.87) can already be fulfilled by 8 layers of inner winding. The outer reinforcement with a low number of layers makes the situation worse and the pipe can only be fixed with a very high number of layers.

Table 7. Reduced stresses and failure coefficients for outer failure with 6 mm depth

Number of layers/ thickness [mm]	$\sigma_{\text{red max}}^{\text{outer}}$ [MPa]	$K_{\text{tw}}^{\text{outer}}$ [-]	$\sigma_{\text{red max}}^{\text{inner}}$ [MPa]	$K_{\text{tw}}^{\text{inner}}$ [-]
0/0	1009,7	–	1009,7	–
4/1,2	550,2	0,0704	1125,5	0,7026
8/2,4	499,2	0,0111	1017,3	0,8056
12/3,6	–	–	825,1	0,4745
16/4,8	–	–	692,3	0,2791
20/6,0	–	–	602,8	0,1807
24/7,2	–	–	539,4	0,1280
28/8,4	–	–	491,9	0,0974

This phenomenon can be explained by Figure 16. With a lower number of outer layers the e eccentricity is increased by the reinforcement which makes the M_{ti} local bending moment higher but a high enough number of layers can compensate this action. However the inner reinforcement creates an opposite bending moment by e_3 eccentricity which can balance the original bending moment.

Table 7 summarizes the numerical results for a 6 mm deep outer failure with 50 mm bandwidth reinforcement, in the left two columns for outer reinforcement and in the right two columns for inner reinforcement.

Table 7. Reduced stresses and failure coefficients for outer failure with 6 mm depth

Number of layers/ thickness [mm]	$\sigma_{\text{red max}}^{\text{outer}}$ [MPa]	$K_{\text{tw}}^{\text{outer}}$ [-]	$\sigma_{\text{red max}}^{\text{inner}}$ [MPa]	$K_{\text{tw}}^{\text{inner}}$ [-]
0/0	1009,7	–	1009,7	–
4/1,2	550,2	0,0704	1125,5	0,7026
8/2,4	499,2	0,0111	1017,3	0,8056
12/3,6	–	–	825,1	0,4745
16/4,8	–	–	692,3	0,2791
20/6,0	–	–	602,8	0,1807
24/7,2	–	–	539,4	0,1280
28/8,4	–	–	491,9	0,0974

When repairing outer circular failure the situation is the opposite to the previous case. It is seen from Table 7 that an outer circular failure can be repaired better by outer reinforcement than by inner one. Also in this case both failure criteria can already be fulfilled by 8 layers of outer winding. The inner reinforcement with a low number of layers makes the situation worse and the pipe can be fixed only with a very high number of layers. The argumentation for this phenomenon is the same as given at inner failures.

6. CONCLUSIONS

The numerical experience of the investigations is the following:

- From the engineering point of view the multilayered shell model is a suitable tool for numerical analysis of pipe failures and for investigation of repaired pipes.
- From the mechanical point of view the insulation layer is negligible.
- The experimental loading case is more hazardous than the normal working conditions.
- The critical strains and stresses are similar at inner and outer circular failures, however the character of deformations is different.
- It is sufficient to use only a few number of CFRP layers for repair of very deep circular failures, if they are applied from the failure side.
- The inner and outer failures have to be fixed by inner and outer reinforcement, respectively.
- The bandwidth in the investigated range of composite layers does not play an important role at the repair of circular failure.

Acknowledgements. The authors wish to acknowledge the assistance given by the Hungarian Agency for Research Fund Management and Research Exploitation (GVOP-3.1.1.-2004-05-0215/3.0) and by the Hungarian Scientific Research Fund (T 049126 and T 048359) for supporting this research.

REFERENCES

1. REDDY, J. N.: *Mechanics of Laminated Composite Plates and Shells, Theory and Analysis*, CRC Press, 2004.
2. MATTHEWS, F. L., DAVIES, G. A. O., HITCHINGS, D., SOUTIS, C.: *Finite Element Modelling of Composite Materials and Structures*, Woodhead Publishing Ltd, Cambridge, 2000.
3. BATHE, K. J.: *Finite Element Procedures*, Prentice Hall International Editions, 1996.
4. I-DEAS User' Guide, UGS PLM Solutions Inc., 2004.
5. ÉGERT, J., PERE, B., MOLNÁR-ÉGERT, É.: Mechanical aspects of fixing pipeline welding failures by reinforcements *EMT Technical Review*, (2008), 125–131. (in Hungarian)
6. PERE, B., ÉGERT, J.: Finite element modelling opportunities of artificial welding failures and outer damage of pipelines. *Proc. microCAD 2008 Int. Sci. Conf. 20-21 March 2008., Section F: Applied Mechanics*, 39–44.
7. LUKÁCS, J., NAGY, GY., TÖRÖK, I.: Investigation of some parts of a test pipe. *Conference Proceedings Integrity of hybride pipes reinforced by polymere matrix composites*. Miskolc-Egyetemváros, Hungary, (2008), 174–193. (in Hungarian)
8. CZÉL, G.: Special material test methods for polymere composite pipe materials. *Conference Proceedings Integrity of hybride pipes reinforced by polymere matrix composites*. Miskolc-Egyetemváros, Hungary, (2008), 17–24. (in Hungarian)

VIBRATION ANALYSIS OF A PIEZOELECTRIC CYLINDER PANEL

BÉLA KOVÁCS

Institute of Mathematics, University of Miskolc,
3515 Miskolc-Egyetemváros, Hungary
matmn@uni-miskolc.hu

[Received: August 31, 2006]

Abstract. A new iterative model is presented for the dynamic analysis of a piezoelectric cylinder panel. The differential equations which govern the free vibrations of a piezoelectric panel as well as the boundary conditions are derived from Hamilton's principle by taking the bending, shear and normal deformation into account. The author developed a new iterative process to successively refine the stress and strain fields and the electrical field in the panel. The model includes the effects of transverse shear and rotary inertia. The iterative model can be applied to predict the modal frequencies and the stress field in the piezoelectric medium under the conditions of cylindrical bending and periodic motion.

Mathematical Subject Classification:

Keywords: piezoelectric cylinder panel, stress and strain fields, electrical field, iterative model

1. INTRODUCTION

In recent years piezo-electric materials and their use in structural dynamic have become a growing area of research. These materials induce electric potential /charge when they are subjected to mechanical deformations by virtue of direct piezoelectric effect and are deformed due to the externally applied voltage by virtue of converse piezoelectric effect. The load-bearing structures fitted with piezoelectric layers, called intelligent structures, are subjected to the coupled action of electric and elastic fields.

The theory of piezoelectricity was first formulated by Voigt in 1894. The basic theory of linear piezoelectricity has been outlined by several authors [1, 2, 3]. Early computational studies of piezoelectric solids include those of Eer Nisse [4] and Holland [5] for electroelastic vibration analysis using Ritz method. The work of Tiersten [6] provided the theoretical foundations and numerous examples of the dynamic behavior of piezoelectric plates. Finite element modelling of the electroelastic behaviour of a piezoelectric sensor/actuator structural system was presented by Tzou and Tseng [7] and Tzou et al. [8]. Robbins and Reddy [9] developed the finite element models of a piezoelectrically actuated beam using four different displacement-based one-dimensional beam theories, derivable from the generalized laminated plate theory of

Reddy [10] to investigate the behaviour of a piezoelectrically actuated beam. Very few exact solutions of the three-dimensional field equations are available for the coupled response of piezoelectric elements to electromechanical loading. Ray et al. [10, 12] presented exact solutions for the static analysis of a simply-supported piezoelectric plate and a layered intelligent plate under cylindrical bending. A three-dimensional analysis of semi-infinite crack embedded in a transversely isotropic piezoelectric material was performed by Sosa and Pak [13]. Heylinger and Brooks [14] have presented exact solutions for the free vibration behavior of piezoelectric laminates in cylinder bending. The equations of motion, the charge equation, and the boundary and interface conditions are satisfied exactly. A discrete-layer laminate model is presented for the analysis of laminated piezoelectric composite shells in [15]. The variational formulation and corresponding finite element model are developed using the equations of motion and the charge equation. Páczelt and Kovács [16] have studied a semicircular planar prismatic beam subjected to bending moments resulting from piezoelectric actuator devices bonded to the parallel surfaces of the beam. The bending and torsional deformations are investigated with the Finite Element Method and the closed-form solution of the linear theory of 3D curved beams, respectively.

The predictor-corrector procedures appear to have high potential for the accurate prediction of vibration frequencies, stresses and deformations in multilayered composite plates and shells. Zapfe and Lesieutre [17] developed an iterative process to refine successively the shape of the stress/strain distribution for the dynamic analysis of laminated beams. The iterative model is used to predict the modal frequencies and damping of simply supported beams with integral viscoelastic layers. Noor and Burton [18] presented a predictor-corrector approach for the analysis of composite plates. The authors used a plate model based on first-order shear deformation theory, coupled with integration of the equilibrium equations, to refine the estimate of the local stress field through the thickness of the laminate. The refined stress field was also used to generate improved estimates of the shear correction factors in the first-order shear deformation model, leading to improved estimates of the plate displacements and natural frequencies. Lee and Cao [19] have presented a predictor-corrector approach for the numerical analysis of general thick laminated plates which ensures that the transverse shear stress distributions from both constitutive and equilibrium considerations are sufficiently close to each other before the computations of the displacements and stresses are considered sufficiently accurate. In the predictor phase, a linear or cubic zig-zag model is adopted and the layerwise polynomial approximation of the transverse shear stresses through the thickness is determined from the equilibrium equations of elasticity.

The present research extends the iterative model developed by Zapfe and Lesieutre to the dynamic analysis of a cylinder panel of piezoelectric medium. The current model is developed for the specific case of a simply supported cylinder panel under the conditions of cylindrical bending and periodic motion.

2. EQUATIONS OF MOTION

The geometry of interest and the notations are shown in Figure 1. We consider an infinitely long (perpendicular to the plane of paper) cylinder panel of piezoelectric medium. The free vibration of the cylinder panel is confined to the $r-\varphi$ plane. The z axis is out-of-plane, with the r and φ coordinates corresponding to the respective radial and circumferential directions of the panel. Owing to the cylinder panel is assumed to be infinitely long in the z - direction, the piezoelectric medium is under cylindrical bending (i.e. plane strain state) in the $r-\varphi$ plane. As indicated in the Figure, the panel ends are simply supported as described by the end conditions. The panel is considered to be thin and of radius of curvature R of the middle surface, and thickness h . The arc length s is measured along the middle surface of the panel in the circumferential direction, which is defined by s (Fig.1), where $s = R\varphi$. The length of the panel in the circumferential direction is denoted by L . In this case $L = R\vartheta$ where ϑ is the opening angle of the curved panel. The displacements of the panel in the φ - and r - directions are denoted by u and w respectively. Under the conditions of cylindrical bending (i.e. plane strain state), the displacements field takes the form $\mathbf{t} = w(r, \varphi, t)\mathbf{e}_r + u(r, \varphi, t)\mathbf{e}_\varphi$, and the electrostatic potential has the form $\Phi = \Phi(r, \varphi, t)$. Hence all variables are independent of the z coordinate, and terms containing a gradient in the z -direction vanish. For the analysis of the response of piezoelectric structural components we need to deal with two different field equations that are coupled to each other. One is the balance of the momentum equation and the other is the balance of the charge equation. These two field equations are coupled to each other through the constitutive equations of the material.

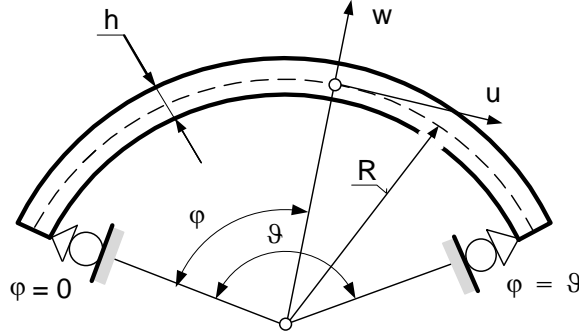


Figure 1. Parameters for a cylinder panel.

We start with a linear, anisotropic, and electro-elastic solid for which the coupled constitutive relation can be written as

$$\sigma_r = C_{11}\varepsilon_r + C_{12}\varepsilon_\varphi - e_{33}E_r, \quad (1)$$

$$\sigma_\varphi = C_{12}\varepsilon_r + C_{22}\varepsilon_\varphi - e_{31}E_r, \quad (2)$$

$$\tau_{r\varphi} = C_{33}\gamma_{r\varphi} - e_{15}E_\varphi, \quad (3)$$

$$D_r = e_{31}\varepsilon_\varphi + e_{33}\varepsilon_r + \varepsilon_{33}E_r, \quad (4)$$

$$D_\varphi = e_{15}\gamma_{r\varphi} + \varepsilon_{11}E_\varphi, \quad (5)$$

where σ_r, σ_φ and $\tau_{r\varphi}$ are the stresses, $\varepsilon_r, \varepsilon_\varphi$ and $\gamma_{r\varphi}$ are the strains, D_r and D_φ denote the electric displacements, E_r and E_φ are the electric fields, C_{11}, C_{12}, C_{22} and C_{33} are the elastic stiffnesses, e_{31}, e_{33} and e_{15} are the electric permittivity components while ε_{11} and ε_{33} stand for the dielectric constants of piezoelectric in the polar coordinate system (r, φ) .

In the present model the displacement field can be given in the following form

$$\begin{aligned} \mathbf{t}(r, \varphi, t) &= w(r, \varphi, t)\mathbf{e}_r + u(r, \varphi, t)\mathbf{e}_\varphi = \\ &= \left[v_0(\varphi, t) - \frac{r-R}{R} \left(\frac{\partial w_0}{\partial \varphi} - v_0(\varphi, t) \right) + f(r)v_1(\varphi, t) \right] \mathbf{e}_\varphi + \\ &\quad + [w_0(\varphi, t) + g(r)w_1(\varphi, t)] \mathbf{e}_r \end{aligned} \quad (6)$$

where $f(R) = 0$ and $g(R) = 0$ which means that (v_0, w_0) denote the displacement at a point (R, φ) on the centre-line along the circumferential and radial directions, respectively.

The terms $f(r)v_1(\varphi, t)$ and $g(r)w_1(\varphi, t)$ can be thought to be the corrections needed to account for the transverse shear and normal deformation effects, respectively. The functions $f(r)$ and $g(r)$ represent the shape of the corrections through the thickness of the cylinder panel, while $v_1(\varphi, t)$ and $w_1(\varphi, t)$ determine their distributions along the circumferential direction. The solution of a given problem requires the determination of the unknown functions $v_0(\varphi, t), v_1(\varphi, t), w_0(\varphi, t), w_1(\varphi, t), f(r)$ and $g(r)$. By using the standard expressions

$$\mathbf{t} = w\mathbf{e}_r + u\mathbf{e}_\varphi, \quad \varepsilon_\varphi = \frac{1}{r} \frac{\partial u}{\partial \varphi} + \frac{w}{r}, \quad \gamma_{r\varphi} = \frac{1}{r} \frac{\partial w}{\partial \varphi} + \frac{\partial u}{\partial r} - \frac{u}{r}, \quad \varepsilon_r = \frac{\partial w}{\partial r}$$

and using equation (6) we can determine the components of the strain tensor

$$\varepsilon_\varphi = \frac{1}{r} \left[\frac{\partial v_0}{\partial \varphi} - \frac{r-R}{R} \left(\frac{\partial^2 w_0}{\partial \varphi^2} - \frac{\partial v_0}{\partial \varphi} \right) + f(r) \frac{\partial v_1}{\partial \varphi} + w_0 + g(r)w_1(\varphi, t) \right], \quad (7)$$

$$\gamma_{r\varphi} = \left[\frac{df}{dr} - \frac{f(r)}{r} \right] v_1(\varphi, t) + \frac{g(r)}{r} \frac{\partial w_1}{\partial \varphi}, \quad (8)$$

$$\varepsilon_r = \frac{dg}{dr} w_1(\varphi, t), \quad (9)$$

where $f(r)$ and $g(r)$ are single-valued functions at each point through the thickness.

For a piezoelectric body we have two balance equations to satisfy simultaneously. The balance of momentum and balance of electric charge require the fulfilment of equations

$$\operatorname{div} \mathbf{T} = \rho \ddot{\mathbf{t}}, \quad (10)$$

$$\operatorname{div} \mathbf{D} = 0 \quad (11)$$

where ρ is the density, $\mathbf{D} = D_r(r, \varphi, t)\mathbf{e}_r + D_\varphi(r, \varphi, t)\mathbf{e}_\varphi$ is the electrical displacement, \mathbf{T} is the stress tensor and the partial derivative with respect to time is denoted by a dot over the letter.

Assume that the cylinder panel considered is in plane strain. Then the equations of motion (10) and the balance of electric charge (11) can be manipulated into the following forms

$$\frac{\partial}{\partial r} [r^2 \tau_{r\varphi}] + r \frac{\partial \sigma_\varphi}{\partial \varphi} = r^2 \rho \frac{\partial^2 u}{\partial t^2}, \quad (12)$$

$$r \frac{\partial \sigma_r}{\partial r} + \sigma_r + \frac{\partial \tau_{r\varphi}}{\partial \varphi} - \sigma_\varphi = r \rho \frac{\partial^2 w}{\partial t^2}, \quad (13)$$

$$\frac{\partial D_r}{\partial r} + \frac{D_r}{r} + \frac{1}{r} \frac{\partial D_\varphi}{\partial \varphi} = 0. \quad (14)$$

The components of the electric field are related to the electrostatic potential $\Phi(r, \varphi, t)$ via the relations

$$E_r = -\frac{\partial \Phi}{\partial r}, \quad E_\varphi = -\frac{1}{r} \frac{\partial \Phi}{\partial \varphi} \quad (15)$$

If the panel is in plain strain $E_z = 0$.

Here the electric potential can be given the following form

$$\Phi(r, \varphi, t) = p(r)q(\varphi, t). \quad (16)$$

In addition to these equations the boundary conditions on the upper and bottom surface of the panel must be specified. For the study of free vibration these two surfaces are assumed to be traction free. Consequently the following boundary conditions should be prescribed

$$\tau_{r\varphi}(r = R + \frac{h}{2}, \varphi, t) = \tau_{r\varphi}(r = R - \frac{h}{2}, \varphi, t) = 0, \quad (17)$$

$$\sigma_r(r = R + \frac{h}{2}, \varphi, t) = \sigma_r(r = R - \frac{h}{2}, \varphi, t) = 0 \quad (18)$$

In addition to the mechanical boundary conditions, the electric surface conditions should also be satisfied. This is accomplished in this study by specifying a homogeneous electrostatic potential:

$$\Phi(r = R + \frac{h}{2}, \varphi, t) = \Phi(r = R - \frac{h}{2}, \varphi, t) = 0 \quad (19)$$

Substitution of equation (16) into equation (19) yields the following boundary conditions on the upper and bottom surface of the panel

$$p(r = R + \frac{h}{2}) = p(r = R - \frac{h}{2}) = 0. \quad (20)$$

The Lagrangian for the cylinder panel is given by [6]:

$$L = \frac{1}{2} \int_{\varphi=0}^{\vartheta} \int_{R-h/2}^{R+h/2} \left[-\sigma_r \varepsilon_r - \sigma_\varphi \varepsilon_\varphi - \tau_{r\varphi} \gamma_{r\varphi} + D_\varphi E_\varphi + D_r E_r + \rho (\dot{\mathbf{t}})^2 \right] r dr d\varphi. \quad (21)$$

Substituting equations (7-9) and (15-16) into equations (1-5) and introducing the results into the Hamilton's principle $\delta \int_{t_1}^{t_2} L dt = 0$ one obtains

$$\begin{aligned}
& A_{1,1} \frac{\partial^4 w_0}{\partial \varphi^4} + A_{1,2} \frac{\partial^2 w_0}{\partial \varphi^2} + A_{1,3} \frac{\partial^2 w_1}{\partial \varphi^2} + A_{1,4} \frac{\partial^3 v_0}{\partial \varphi^3} + A_{1,5} \frac{\partial^3 v_1}{\partial \varphi^3} + \\
& + A_{1,6} \frac{\partial^2 q}{\partial \varphi^2} + A_{1,7} \frac{\partial v_0}{\partial \varphi} + A_{1,8} \frac{\partial v_1}{\partial \varphi} + A_{1,9} w_1 + A_{1,10} w_0 + A_{1,11} q = \\
& = D_{1,1} \frac{\partial^4 w_0}{\partial \varphi^2 \partial t^2} + D_{1,2} \frac{\partial^3 v_0}{\partial \varphi \partial t^2} + D_{1,3} \frac{\partial^3 v_1}{\partial \varphi \partial t^2} + D_{1,4} \frac{\partial^2 w_0}{\partial t^2} + D_{1,5} \frac{\partial^2 w_1}{\partial t^2} , \quad (22a)
\end{aligned}$$

$$\begin{aligned}
& A_{2,1} \frac{\partial^2 w_0}{\partial \varphi^2} + A_{2,2} \frac{\partial^2 w_1}{\partial \varphi^2} + A_{2,3} \frac{\partial^2 q}{\partial \varphi^2} + A_{2,4} \frac{\partial v_1}{\partial \varphi} + A_{2,5} \frac{\partial v_0}{\partial \varphi} + \\
& + A_{2,6} w_1 + A_{2,7} w_0 + A_{2,8} q = D_{2,1} \frac{\partial^2 w_0}{\partial t^2} + D_{2,2} \frac{\partial^2 w_1}{\partial t^2} , \quad (22b)
\end{aligned}$$

$$\begin{aligned}
& A_{3,1} \frac{\partial^3 w_0}{\partial \varphi^3} + A_{3,2} \frac{\partial^2 v_1}{\partial \varphi^2} + A_{3,3} \frac{\partial^2 v_0}{\partial \varphi^2} + A_{3,4} \frac{\partial w_0}{\partial \varphi} + A_{3,5} \frac{\partial w_1}{\partial \varphi} + \\
& + A_{3,6} \frac{\partial q}{\partial \varphi} + A_{3,7} v_1 = D_{3,1} \frac{\partial^2 v_1}{\partial t^2} + D_{3,2} \frac{\partial^2 v_0}{\partial t^2} + D_{3,3} \frac{\partial^3 w_0}{\partial \varphi \partial t^2} , \quad (22c)
\end{aligned}$$

$$\begin{aligned}
& A_{4,1} \frac{\partial^3 w_0}{\partial \varphi^3} + A_{4,2} \frac{\partial^2 v_0}{\partial \varphi^2} + A_{4,3} \frac{\partial^2 v_1}{\partial \varphi^2} + A_{4,4} \frac{\partial w_0}{\partial \varphi} + \\
& + A_{4,5} \frac{\partial w_1}{\partial \varphi} + A_{4,6} \frac{\partial q}{\partial \varphi} = D_{4,1} \frac{\partial^3 w_0}{\partial \varphi \partial t^2} + D_{4,2} \frac{\partial^2 v_0}{\partial t^2} + D_{4,3} \frac{\partial^2 v_1}{\partial t^2} , \quad (22d)
\end{aligned}$$

$$A_{5,1} \frac{\partial^2 w_0}{\partial \varphi^2} + A_{5,2} \frac{\partial^2 w_1}{\partial \varphi^2} + A_{5,3} \frac{\partial^2 q}{\partial \varphi^2} + A_{5,4} w_0 + A_{5,5} w_1 + A_{5,6} q = 0 , \quad (22e)$$

the equations of motion for the four unknown functions, $w_0(\varphi, t)$, $w_1(\varphi, t)$, $v_0(\varphi, t)$, $v_1(\varphi, t)$ and $q(\varphi, t)$. In equations (22a-22e) A_{ij} and D_{ij} are given in the Appendix.

The section stiffness K_{1-27} and the mass coefficients M_{1-8} are provided by the following equations

$$K_{[1,\dots,10]} = \int_{R-h/2}^{R+h/2} C_{22} \left[\frac{1}{r}, r, \frac{1}{r} f^2, \frac{1}{r} g^2, 1, \frac{1}{r} f, \frac{1}{r} g, f, g, \frac{1}{r} f g \right] dr , \quad (23a)$$

$$K_{[11]} = \int_{R-h/2}^{R+h/2} C_{11} r \left(\frac{dg}{dr} \right)^2 dr, \quad (23b)$$

$$K_{[12,\dots,15]} = \int_{R-h/2}^{R+h/2} C_{12} \left[\frac{dg}{dr}, r \frac{dg}{dr}, f \frac{dg}{dr}, g \frac{dg}{dr} \right] dr, \quad (23c)$$

$$K_{[16,\dots,18]} = \int_{R-h/2}^{R+h/2} C_{33} \left[r \left(\frac{df}{dr} - \frac{f}{r} \right)^2, \left(\frac{df}{dr} - \frac{f}{r} \right) g, \frac{1}{r} g^2 \right] dr, \quad (23d)$$

$$K_{[23]} = \int_{R-h/2}^{R+h/2} e_{33} r \left(\frac{dg}{dr} \right) \left(\frac{dp}{dr} \right) dr, \quad (23e)$$

$$K_{[24,25]} = \int_{R-h/2}^{R+h/2} e_{15} \left[p \left(\frac{df}{dr} - \frac{f}{r} \right), \frac{1}{r} gp \right] dr, \quad (23f)$$

$$K_{[26]} = \int_{R-h/2}^{R+h/2} \varepsilon_{11} \frac{1}{r} p^2 dr, \quad (23g)$$

$$K_{[27]} = \int_{R-h/2}^{R+h/2} \varepsilon_{33} r \left(\frac{dp}{dr} \right)^2 dr, \quad (23h)$$

$$M_{[1,\dots,8]} = \int_{R-h/2}^{R+h/2} \rho [r, r^2, r^3, rf, r^2f, rf^2, rg, rg^2] dr, \quad (23i)$$

The kinematic and natural boundary conditions specified at $\varphi = 0$ and $\varphi = \vartheta$, are given by

$$v_0 = 0, \quad F_{11} \frac{\partial^2 w_0}{\partial \varphi^2} + F_{12} \frac{\partial v_0}{\partial \varphi} + F_{13} \frac{\partial v_1}{\partial \varphi} + F_{14} w_0 + F_{15} w_1 + F_{16} q = 0 \quad (24a)$$

$$w_0 = 0, \quad F_{21} \frac{\partial^3 w_0}{\partial \varphi^3} + F_{22} \frac{\partial^2 v_0}{\partial \varphi^2} + F_{23} \frac{\partial^2 v_1}{\partial \varphi^2} + F_{24} \frac{\partial^3 w_0}{\partial \varphi^2 \partial t} + F_{25} \frac{\partial^2 v_0}{\partial t^2} + F_{26} \frac{\partial^2 v_1}{\partial t^2} + F_{27} \frac{\partial w_0}{\partial \varphi} + F_{28} \frac{\partial w_1}{\partial \varphi} + F_{29} \frac{\partial q}{\partial \varphi} = 0 \quad (24b)$$

$$v_1 = 0, \quad F_{31} \frac{\partial^2 w_0}{\partial \varphi^2} + F_{32} \frac{\partial v_0}{\partial \varphi} + F_{33} \frac{\partial v_1}{\partial \varphi} + F_{34} w_0 + F_{35} w_1 + F_{36} q = 0 \quad (24c)$$

$$\frac{\partial w_0}{\partial \varphi} = 0, \quad F_{41} \frac{\partial^2 w_0}{\partial \varphi^2} + F_{42} \frac{\partial v_0}{\partial \varphi} + F_{43} \frac{\partial v_1}{\partial \varphi} + F_{44} w_0 + F_{45} w_1 + F_{46} q = 0 \quad (24d)$$

$$w_1 = 0, \quad F_{51} \frac{\partial w_1}{\partial \varphi} + F_{52} v_1 + F_{53} \frac{\partial q}{\partial \varphi} = 0 \quad (24e)$$

$$q = 0, \quad F_{61} \frac{\partial w_1}{\partial \varphi} + F_{62} v_1 + F_{63} \frac{\partial q}{\partial \varphi} = 0 \quad (24f)$$

where F_{ij} are constants. For the special case of a simply supported curved panel, the first, third and fourth natural boundary conditions are combined with the kinematic condition, $w_0 = w_1 = q = 0$. In this case the edges of panel are assumed to be grounded.

3. SOLUTION FOR A SIMPLY SUPPORTED PANEL

The displacement functions and the potential function satisfying the boundary conditions can be given by

$$w_0(\varphi, t) = W_0 \sin(k_n \varphi) e^{i\omega_n t} \quad (25a)$$

$$w_1(\varphi, t) = W_1 \sin(k_n \varphi) e^{i\omega_n t} \quad (25b)$$

$$v_0(\varphi, t) = V_0 \cos(k_n \varphi) e^{i\omega_n t} \quad (25c)$$

$$v_1(\varphi, t) = V_1 \cos(k_n \varphi) e^{i\omega_n t} \quad (25d)$$

$$q(\varphi, t) = Q \sin(k_n \varphi) e^{i\omega_n t} \quad (25e)$$

where $k_n = (n\pi)/\vartheta$. Substitution of equations (25) into equations (22-23) results in a set of five simultaneous, homogeneous algebraic equations with symmetric coefficients. In matrix form, these equations are

$$[-\omega_n^2 [M] + [Y]] \{U\} = 0, \quad \{U\} = \{W_0, W_1, V_0, V_1, Q\} \quad (26)$$

where M_{ij} and Y_{ij} are given in the Appendix. While the assumed form of the correction functions $f^{(k)}(r)$, $g^{(k)}(r)$ and $p^{(k)}(r)$ will change from one iteration to the next, in each iteration step they can be treated as known functions. In this phase an estimation of the eigenvalues $W_0^{(k)}$, $W_1^{(k)}$, $V_0^{(k)}$, $V_1^{(k)}$ and $Q^{(k)}$ and frequency of vibration $\omega_n^{(k)}$ are obtained by solving equation (26). This approximation is then used in the corrector phase in order to improve the predictions for the correction functions $f^{(k+1)}(r)$, $g^{(k+1)}(r)$ and $p^{(k+1)}(r)$.

4. IMPROVED ESTIMATE FOR CORRECTION FUNCTIONS

An improved estimate for the correction functions $f^{(k+1)}(r)$, $g^{(k+1)}(r)$ and $p^{(k+1)}(r)$ is derived from the three-dimensional equilibrium equations and the three-dimensional constitutive relations. The transverse shear and normal stress are obtained by integrating the 3D equilibrium equations (12-13) in the thickness direction as follows:

$$\tau_{r\varphi}^{(k+1)} = \frac{1}{r^2} \int_{R-h/2}^r r^2 \rho \frac{\partial^2 u^{(k)}}{\partial t^2} - r \frac{\partial \sigma_\varphi^{(k)}}{\partial \varphi} dr + C_1, \quad (27)$$

$$\sigma_r^{(k+1)} = \frac{1}{r} \int_{R-h/2}^r r \rho \frac{\partial^2 w^{(k)}}{\partial t^2} + \sigma_\varphi^{(k)} - \frac{\partial \tau_{r\varphi}^{(k+1)}}{\partial \varphi} dr + C_2, \quad (28)$$

where $\sigma_\varphi^{(k)} = C_{12}\varepsilon_r^{(k)} + C_{22}\varepsilon_\varphi^{(k)} - e_{31}E_r^{(k)}$ is obtained from equation (2). The constants C_1 and C_2 can be determined from the stress boundary conditions imposed on the outer surfaces of the panel. Owing to equations (17) and (18) we have $C_1 = C_2 = 0$.

The transverse electric displacement D_r is calculated by integrating the 3D charge equation of electrostatic (14) in the thickness direction

$$D_r^{(k+1)} = \frac{1}{r} \int_{R-h/2}^r -\frac{\partial D_\varphi^{(k)}}{\partial \varphi} dr + C_3, \quad (29)$$

where $D_\varphi^{(k)} = e_{15}\varepsilon_{r\varphi}^{(k)} + \varepsilon_{11}E_\varphi^{(k)}$ is obtained from equation (5). The integration constant C_3 is obtained by setting $D_r^{(k+1)}$ at $r = R$ to be equal to the transverse electric displacement of the previous iteration $D_r^{(k)}$.

Substitution of equations (7-9), (15-16) and (25) in equations (1), (3) and (4) yield the following set of differential equations in terms of the new unknown correction functions $f^{(k+1)}(r)$, $g^{(k+1)}(r)$ and $p^{(k+1)}(r)$.

$$C_{11}W_1^{(k)} \frac{dg^{(k+1)}}{dr} - \frac{C_{12}}{r} k_n V_1^{(k)} f^{(k+1)}(r) + \frac{C_{12}}{r} W_1^{(k)} g^{(k+1)}(r) - e_{33}Q^{(k)} \frac{dp^{(k+1)}}{dr} =$$

$$= \sigma_r^{(k+1)} - \frac{C_{12}}{r}(-V_0^{(k)}k_n + \frac{r-R}{R}(k_n^2W_0^{(k)} - k_nV_0^{(k)}) + W_0^{(k)}) \quad (30a)$$

$$C_{33}V_1^{(k)}\frac{df^{(k+1)}}{dr} - \frac{C_{33}}{r}k_nV_1^{(k)}f^{(k+1)}(r) + \frac{C_{33}}{r}W_1^{(k)}k_ng^{(k+1)}(r) + \frac{e_{15}}{r}k_nQ^{(k)}p^{(k+1)} = \tau_r^{(k+1)} \quad (30b)$$

$$e_{33}W_1^{(k)}\frac{dg^{(k+1)}}{dr} - e_{33}Q^{(k)}\frac{dp^{(k+1)}}{dr} - \frac{e_{31}}{r}k_nV_1^{(k)}f^{(k+1)}(r) + \frac{e_{31}}{r}W_1^{(k)}g^{(k+1)}(r) = \\ = D_r^{(k+1)} - \frac{e_{31}}{r}(-V_0^{(k)}k_n + \frac{r-R}{R}(k_n^2W_0^{(k)} - k_nV_0^{(k)}) + W_0^{(k)}) \quad (30c)$$

where $\tau_r^{(k+1)}$, $\sigma_r^{(k+1)}$ and $D_r^{(k+1)}$ are obtained from equations (27-29). As implied above, in addition to these differential equations, the new correction functions must satisfy the following boundary conditions:

$$f^{(k+1)}(R) = g^{(k+1)}(R) = p^{(k+1)}(R - h/2) = p^{(k+1)}(R + h/2) = 0. \quad (31)$$

The distribution of the new correction functions in the thickness direction is obtained by integrating the equations (30) subject to the boundary conditions of equations (31). The integrals in equations (30) are evaluated numerically using a trapezoidal method. This new estimates of $f^{(k+1)}(r)$, $g^{(k+1)}(r)$ and $p^{(k+1)}(r)$ are used as the correction functions for the next iteration. As with any smeared laminate model,

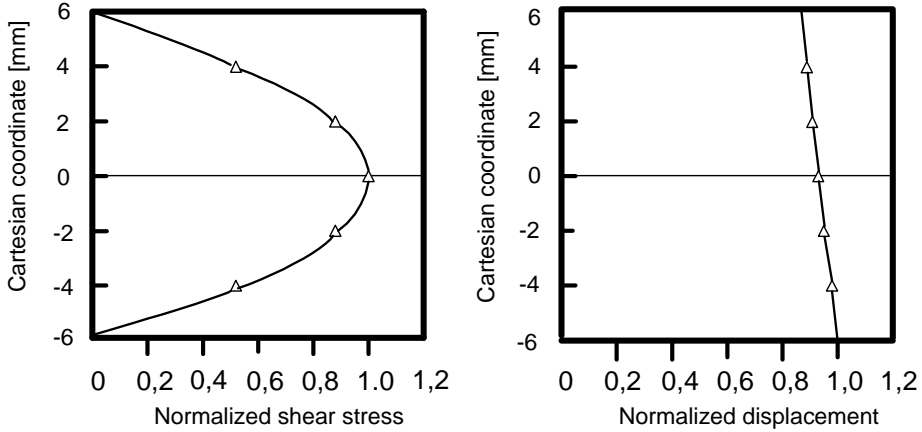


Figure 2. Through-thickness mode shapes for piezoelectric cylinder panel.

there are two distinct ways to calculate the shear stress distribution: from the material constitutive relations; or by elemental stress equilibrium. The ultimate goal of the iterative analysis is the determination of the functions, $f(r)$ and $g(r)$, that causes the two stress distributions to be equal. This defines the convergence point for

the iterative functions $f(r)$ and $g(r)$, the point at which the stresses and strains are self-consistent.

5. RESULTS AND DISCUSSION

We consider a layer of piezoelectric material. The input data used here were $h = 12.0$ mm, $R = 0.8$ m, $L = 0.8$ m, $\vartheta = 1.0$ rad, $C_{11} = 6.45 \cdot 10^{10}$ N/m², $C_{22} = 8.13 \cdot 10^{10}$ N/m², $C_{12} = 0.0432 \cdot 10^{10}$ N/m², $C_{33} = 2.56 \cdot 10^{10}$ N/m², $\rho = 2.7 \cdot 10^3$ kg/m³, $e_{33} = 15.8$ C/m², $e_{31} = -5.2$ C/m², $e_{15} = 12.72$ C/m², $\varepsilon_{11} = 1.51 \cdot 10^{-8}$ F/m, $\varepsilon_{33} = 1.3 \cdot 10^{-8}$ F/m. In the example the thickness-to-radius ratio was 0.015 i.e. the panel is considered to be thin and of radius of curvature R of the middle surface, and thickness h .

Table 1 Iteration improvement of frequency factor for the panel

Iteration number	frequency factor ω_n^2
1	$6.297877 \cdot 10^4$
2	$6.399191 \cdot 10^4$
3	$6.386247 \cdot 10^4$
4	$6.386247 \cdot 10^4$

For the minimum vibration frequencies ($n = 1$) representative through-thickness distributions of the elastic and electric field variables are shown.

These have been normalized by dividing through by the maximum value for each field variable. The through-thickness distributions for axial displacement u , transverse shear stress $\tau_{r\varphi}$, transverse normal stress σ_r , and transverse electric field E_r are shown in Fig. 2-3, respectively, associated with minimum vibration frequencies. The plot for the transverse displacement w is not shown because for the thin panel the distribution is essentially constant through the thickness.

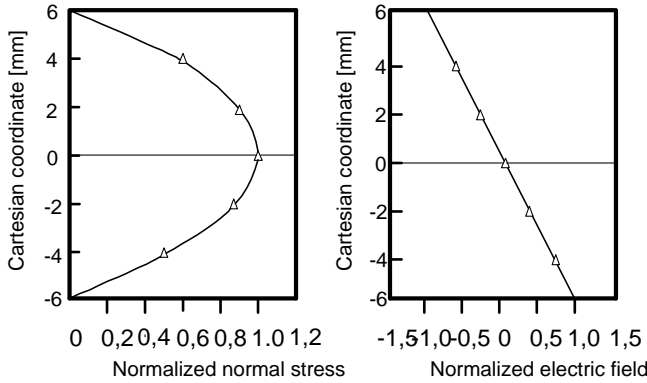


Figure 3. Through-thickness mode shapes for the piezoelectric cylinder panel.

Since $f(r)$ and $g(r)$ are determined from the previous iteration, the question arises as to what to use for the first iteration. Almost any reasonable displacement assumption is acceptable, however experience has shown that a quadratic shear stress distribution is a very good starting point. Table 1. shows the improvement in the prediction of the frequency factor ω_n^2 for the cylinder panel example using a quadratic shear stress as a starting point for the first iteration.

6. CONCLUSIONS

A new iterative model has been presented for a thin piezoelectric cylindrical panel that can accurately determine the dynamic stress distribution in the panel. This represents an advantage over previous smeared laminate models, in which accurate estimates of the stress field were only possible if the assumed displacement field was a reasonable approximation of the actual displacement field. Accurate determination of the stress and displacement fields is particularly important for "stress critical" calculations such as damping and delamination.

REFERENCES

1. CADY, W. G.: *Piezoelectricity* (rev. ed.) Dover, New York, 1964.
2. NYE, N. Y.: *Physical Properties of Crystal: Their Representation by tensors and Matrices*, Oxford University Press, Oxford, England, 1972.
3. PARTON V. Z. and KUNDRYAVTSEV, B. A.: *Electromagnetoelasticity*, Gordon and Breach, New York, 1988.
4. EER NISSE, E. P.: Resonances of one-nimensional composite piezoelectric and elastic structures. *IEEE Transactions on Sonics and Ultrasonics*, **14**, (1967), 59-67.
5. HOLLAND, R.: Resonant properties of piezoelectric ceramic rectangular parrallelepipeds. *Journal of the Acoustical Society of America*, **43** (1968), 988-997.
6. TIERSTEN H. F. *Linear Piezoelectric Plate Vibrations*. Plenum Press, New York, 1969.
7. TZOU, H. S. and TSENG C. I.: Distributed piezoelectric sensor/actuator design for dynamic measurement/control of distributed parameter systems: A piezoelectric finite element approach. *Journal of Sound and Vibration*, **138**, (1990), 17-34.
8. TZOU, H. S., TSENG C. I. and WAN, G. C.: Distributed structural dynamics control of flexible manipulators-II. Distributed sensor and active electromechanical actuator. *Computers and Structures*, **35**, (1990), 679-687.
9. ROBBINS D. H. and REDDY, J. N.: Analysis of piezoelectrically actuated beams using a layer-wise displacement theory.1991 *Computers and Structures*, **41**, (1991), 265-279.
10. REDDY, J. N.: A generalization of two-dimensional theories of laminated composite plates. *Communication Applied Numerical Mathamatics*, **3**, (1987), 173-???
11. RAY, M. C., RAO, K. M. and SAMANTA, B.: Exact analysis of coupled electroelastic behavior of a piezoelectric plate under cylinder bending. *Computers and Structures*, **45**, (1992), 667-677.
12. RAY, M. C., RAO, K. M. and SAMANTA, B.: Exact analysis for static analysis of an intelligent structure under cylinder bending. *Computers and Structures*, **47**, (1993), 1031-1042.

13. Sosa, H. A. and Pak, Y. E.: Three dimensional eigenfunction analysis of a crack in a piezoelectric material. *International Journal of Solids and Structures*, **26**, (1990), 1-15.
14. HEYLINGER, P. and BROOKS, S.: Free vibration of piezoelectric laminates in cylinder bending. *International Journal of Solids and Structures*, **32**, (1994), 2945-2960.
15. HEYLINGER, P., PEI, K. C. and SARAVANOS, D.: Layerwise mechanics and finite element model for laminated piezoelectric shells. *AIAA Journal*, **34**, (1996), 2353-2360.
16. KOVÁCS, P. Z. and PÁCZELT, I.: Investigation of the deformation of a multilayered piezoelectric semiring. *Journal of Computational and Applied Mechanics*, **4**, (2002), 159-173.
17. Zapfe, J. A. and Lesieutre G. A.: Vibration analyses of laminated beams using an iterative smeared laminate model. *Journal of Sound and Vibration*, **199**, (1997), 275-284.
18. Noor, A. K. and Burton, W. S.: Stress and free vibration analyses of multilayered composite plates. *Computers and Structures*, **11**, (1989), 183-204.
19. Lee, K.H. and Cao, L.: 1995 A predictor-corrector zig-zag model for the bending of laminated composite plates. *International Journal of Solids and Structures* **33**, (1995), 879-897.

APPENDIX A. CONSTANTS

Equations (22) to (23) in the main text are given in terms of A_{ij} and D_{ij} which are presented below:

$$\begin{aligned}
 A_{1,1} &= K_1 + K_2 - 2K_5/R, & A_{1,2} &= 2K_1 - 2K_5/R \\
 A_{1,3} &= K_7 + K_{12} - K_9/R - K_{13}/R \\
 A_{1,4} &= -K_2 + K_5/R, & A_{1,5} &= K_6 - K_8/R \\
 A_{1,6} &= K_{19} - K_{20}/R, & A_{1,7} &= K_5/R \\
 A_{1,8} &= K_6, & A_{1,9} &= K_{12} + K_7, & A_{1,10} &= K_1, & A_{1,11} &= K_{19} \\
 A_{2,1} &= -K_7 - K_{12} + K_9/R + K_{13}/R, & A_{2,2} &= K_{18}, & A_{2,3} &= K_{27}, \\
 A_{2,4} &= K_{17} - K_{10} - K_{14}, & A_{2,5} &= -K_9/R - K_{13}/R \\
 A_{2,6} &= -K_4 - K_{11} - K_{15} \\
 A_{2,7} &= -K_7 - K_{12}, & A_{2,8} &= -K_{22} - K_{23} \\
 A_{3,1} &= K_6 - K_8/R, & A_{3,2} &= K_3, & A_{3,3} &= K_8/R \\
 A_{3,4} &= K_6, & A_{3,5} &= K_{10} + K_{14} - K_{16} \\
 A_{3,6} &= K_{21} - K_{26}, & A_{3,7} &= -K_{16} \\
 A_{4,1} &= K_5/R - K_2, & A_{4,2} &= K_2, & A_{4,3} &= K_8/R, & A_{4,4} &= K_5/R \\
 A_{4,5} &= K_9/R + K_{13}/R, & A_{4,6} &= K_{20}/R \\
 A_{5,1} &= K_{20}/R - K_{19}, & A_{5,2} &= K_{27}, & A_{5,3} &= -K_{30}, & A_{5,4} &= -K_{19} \\
 A_{5,5} &= -K_{22} - K_{23}, & A_{5,6} &= K_{31} \\
 D_{1,1} &= M_1 - 2M_2/R + M_3/R^2 \\
 D_{1,2} &= M_2/R - M_3/R^2, & D_{1,3} &= M_4 - M_5/R \\
 D_{1,4} &= -M_1, & D_{1,5} &= -M_7, & D_{2,1} &= M_7, & D_{2,2} &= M_8 \\
 D_{3,1} &= M_6, & D_{3,2} &= M_5/R, & D_{3,3} &= M_4 - M_5/R \\
 D_{4,1} &= M_2/R - M_3/R^2, & D_{4,2} &= M_3/R^2, & D_{4,3} &= M_5/R.
 \end{aligned}$$

Equation (26) in the main text contain the quantities Y_{ij} and M_{ij} which are presented below:

$$\begin{aligned}
Y_{11} &= k_n^4 (K_1 + K_2 - 2K_5/R) - 2k_n^2 (K_1 - K_5/R) + K_1 \\
Y_{12} = Y_{21} &= K_7 + K_{12} - k_n^2 (K_7 + K_{12} - K_9/R - K_{13}/R), \\
Y_{13} = Y_{31} &= k_n^3 (K_5/R - K_2) - k_n K_5/R \\
Y_{14} = Y_{41} &= k_n^3 (K_6 - K_8/R) - k_n K_6 \\
Y_{15} = Y_{51} &= K_{19} - k_n^2 (K_{19} - K_{20}/R) \\
Y_{22} &= k_n^2 K_{18} + K_4 + K_{11} + K_{15}, \quad Y_{23} = Y_{32} = k_n (-K_9/R - K_{13}/R) \\
Y_{24} = Y_{42} &= k_n (K_{17} - K_{10} - K_{14}), \quad Y_{25} = Y_{52} = k_n^2 K_{27} + K_{22} + K_{23} \\
Y_{33} &= k_n^2 K_2, \quad Y_{34} = Y_{43} = k_n^2 K_8/R, \quad Y_{35} = Y_{53} = -k_n K_{20}/R \\
Y_{44} &= k_n^2 K_3 + K_{16}, \quad Y_{45} = Y_{54} = k_n (K_{26} - K_{21}), \quad Y_{55} = -K_{31} - k_n^2 K_{30} \\
M_{11} &= M_1 + k_n^2 (M_1 + M_3/R^2 - 2M_2/R), \quad M_{12} = M_{21} = M_7 \\
M_{13} &= M_{31} = k_n (M_2/R - M_3/R^2), \quad M_{14} = M_{41} = k_n (M_4 - M_5/R) \\
M_{33} &= M_3/R^2, \quad M_{34} = M_{43} = M_5/R, \quad M_{44} = M_6, \quad M_{22} = M_8 \\
M_{23} &= M_{32} = M_{24} = M_{42} = 0.
\end{aligned}$$

TOPOLOGY OPTIMIZATION IN THE CASE OF DIFFERENT BOUNDARY CONDITIONS BY AN ITERATIVE METHOD

JÁNOS LÓGÓ

Department of Structural Mechanics, Budapest University of Technology and Economics
H-1111 Budapest, Műegyetem rkp. 3, Hungary
`logo@ep-mech.me.bme.hu`

[Received: December 12, 2005]

Abstract. Optimal design with thousands of variables is a great challenge in engineering calculations. In this paper an iteration based topology design technique is introduced for the optimization of linearly elastic continuum type structures under single parametric static loading and different displacement boundary conditions. The support optimization is discussed briefly, as well. The investigated problem is utilized by minimization of the weight of the structure subjected to displacement constraints. The numerical procedure is based on an iterative formula which is formed by the use of the Kuhn-Tucker condition of the Lagrangian function of the constraint mathematical programming problem. The application is illustrated by numerical examples.

Mathematical Subject Classification: 74P15

Keywords: mathematical programming, topology optimization, optimal design

1. Introduction

The past century has produced impressive improvements in power and efficiency of mathematical programming techniques as applied to general structural design problem. These methods with their generality do not allow significant number of design variables and number of constraints. This tends to restrict their usefulness to problems with from tens to a few hundreds of design variables. Attempts to apply numerical search procedures to resize problem have failed due to the fact of the large number of design variables involved or the huge computational expenses. The special approaches which have solved such problems successfully are known from the literature as optimality criteria methods.

Recently the topology optimization is one of the most "popular" topic in the expanding field of optimal design. A great number of papers indicates the importance of the topic [1,3-5,7,9,11,23,25,27,28]. The popularity comes one part from the needs of the industry (car, airplane, etc.) and other part from the complexity of the problem which is a great challenging for the researchers. In present stage the field of topology optimization can be divided into two subfields: optimal design of skeletal structures (trusses, grids, etc.) deals with the simultaneous optimization of the member sizes

and geometry (coordinates of joints). This field is named layout optimization. The other subfield is called generalized shape optimization which deals with the simultaneous optimization of the topology and shape of the internal boundaries of the continuum type structures made of composite or porous materials. This subfield is based on the use on the Finite Element method and in the fundamental problem class the optimal structure is “built up” from empty (no material) and solid (filled with given isotropic material) elements.

The history of the topology optimization is approximately 100 years old. At the first 80 years a skeletal structure (usually a truss) was the object of the optimization problem. Exactly one hundred years ago Michell [13] used the full stress design (FSD) criteria on statically determinate structures to obtain the minimum weight structure. In 1957 Barta [2] extended this method to statically indeterminate structures and found that FSD did not converge to the minimum weight design. The other important intuitive method was the uniform strain energy density design. Formal methods of the calculus of variation, applied by Taylor [29], Prager and his co-workers [see e.g. 15,16,17] to specific distributed parameter problems, showed great promise, suggesting that implementation to discretized (e.g., FEM) models could lead to a new class of general purpose optimization methods. The first discretized optimality criteria methods were based on strain energy distributions characterizing optimum structural designs for stress constraints. As Prager and Taylor [15] showed, if the work of the applied loads is limited as an equality constraint, the optimum structure with uniform material properties has uniform energy density distribution.

The origin of the classical optimality criteria method (COC) is dated back into the 70-es. Turning attention to certain stiffness constraints theoretically valid optimality criteria were derived for skeletal structures with displacement constraints employing classical Lagrangian multiplier methods of mathematical programming optimization. To satisfy the optimality criteria an algorithm (an iterative formula) was proposed by Berke [6] based on the attitude that this formula theoretically correctly guaranteeing at least a local optimum when satisfied. Berke also suggested that the design variables and constraints should be separated into a passive and an active sets. In 1991 Kaliszky and Lógó [10] presented a new type of application for the optimal design of dynamically loaded reinforced concrete frames under displacement and deformation constraint. The solution based on Berke’s optimality criteria method with multiple constraints and a penalty parameter was used in the iterative formulation. The finite element based topology optimization was first explored in 1973 by Rossow and Taylor [18] and later Cheng and Olhoff [8]. In 1988 a new generation of problem formulation were created by Bendsoe and Kikuchi [3] using homogenization. A detailed description of continuum-type optimality criteria method was reported in Rozvany’s books [20, 23] and several reports [21, 22, 25, 30]. Their work opened a new “road” in research named topology optimization, but the common thing is that all of them use the basic idea of the classical optimality criteria.

It can be seen that it was enough a half decade to develop a new direction in field of structural optimization. At the beginning of 90-es the topology optimization method was split into two main parts: one part is based on the SIMP type method (Solid

Isotropic Microstructures with Penalty) the other part is used homogenization. Allaire and Khons' work [1, 23] gives a clear description of the homogenization technique.

In the following an iterative technique (which is named SIMP method) and the connected numerical examples will be discussed in detail. The standard FEM computer program with quadrilateral membrane and truss elements is applied in the numerical calculation. The object of the design (so-called ground structure) is a rectangular disk with given loading (one parametric static) and support conditions (fix or/and elastic bars). The material is linearly elastic. The design variables are the thickness or/and cross-sectional area of the finite elements. To obtain the correct optimal topology some filtering method has to be applied to avoid the so-called "checker-board pattern".

2. Optimization problem

2.1. Problem statement. For illustration purposes an engineering design problem is investigated. Let's given a design space (space means a volume which has to fill with structural elements), where the structure is constructed by truss and membrane elements. By the use of the FEM (Finite Element Method) definitions, let's consider the simple case of

- a 2D structure consisting of disk' ground elements ($g = 1, \dots, G$) which must have a constant thickness (t_g) of either $t_g = t_{\min} = 0$ or $t_g = t_{\max} = 1$, such that each ground elements (g) contains one or several sub-elements ($e = 1, \dots, E_s$), whose stiffness coefficients are linear homogeneous functions of the ground element thickness t_g , (Practically it means that the meshing consists of two parts, a primary and a secondary one.)
- The truss elements are given by their length and cross-sectional area. The above "thickness" normalization is used for the cross-sectional areas, as well. (The cross-sectional area is multiplied by t_g .)
- A single static loading with given boundary conditions and
- displacement constraints ($d = 1, \dots, D$).

Using the above-normalized determination, the structure can easily be transformed to problems with a different prescribed maximum thickness $t_g = t_{\max}$. Due to the linear relations this is done by multiplying all loads by t_{\max} , whilst stresses, strains and displacements do not alter their value.

2.1.1. The applied finite element technique. The design domain is discretized in the usual way. (Figure 1.) As it was mentioned 4 nodes disk elements (Figure 2) and 2D truss elements are used. In that way numerically the two types of element can be handled easily.

The nodes are interconnected by disk or/and bar elements. The applied shape functions of the disk's element are given as follows: $N_1(\xi, \eta) = \frac{1}{4}(1 - \xi)(1 - \eta)$; $N_2(\xi, \eta) = \frac{1}{4}(1 + \xi)(1 - \eta)$; $N_3(\xi, \eta) = \frac{1}{4}(1 + \xi)(1 + \eta)$; $N_4(\xi, \eta) = \frac{1}{4}(1 - \xi)(1 + \eta)$. The displacement boundary conditions are given in form of fix supports, elastic springs

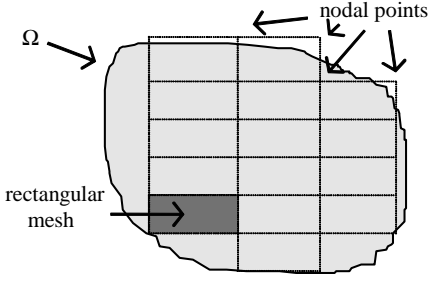


Figure 1. Discretization of the design domain

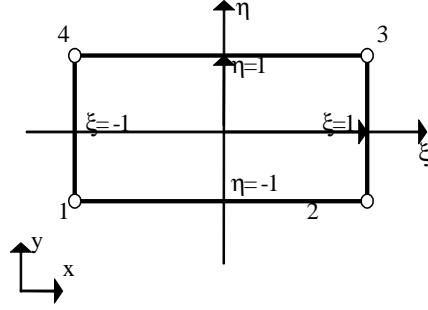


Figure 2. Local coordinate system and basic disk element

and elastic bars, respectively. The system stiffness matrix can be constructed by applying the assembling rule for iso-parametric elements.

2.1.2. Mathematical programming formulation. The structure is constructed by G piece of ground elements, where $G = N_{Disk} + N_{Bar}$. Here N_{Disk} is the number of the ground disk elements and N_{Bar} is the number of the bar elements.

The weight (W) of the structure is given by

$$W = \sum_{id=1}^{ndisc} \gamma_{id} A_{id} t_{id} + \sum_{ib=1}^{nbar} \gamma_{ib} A_{ib} \ell_{ib} t_{ib}. \quad (1a)$$

Here γ_{id} and γ_{ib} the specific weight of the disk and bar elements, respectively. A_{id} is the area of the id -th disk element, A_{ib} is cross-section area and ℓ_{ib} the length of the ib -th bar element. If an artificial variable A_g is introduced (in case of disk it means the area of the element $A_g = A_{id}$, while in case of bar elements it has the following meaning: $A_g = A_{ib} \ell_{ib}$) the weight calculation can be expressed by the following compact form:

$$W = \sum_{g=1}^G \gamma_g A_g t_g, \quad (1b)$$

where γ_g is the specific weight of the ground element g .

The displacement constraint can be expressed as

$$\hat{\mathbf{u}}_d^T \mathbf{K} \mathbf{u} - \Delta_d \leq 0; (d = 1, \dots, D) \quad (2)$$

where $\hat{\mathbf{u}}_d$ is the virtual nodal displacement vector caused by the virtual loads (e.g. “unit dummy loads”) associated with the displacement constraints, \mathbf{K} is the system stiffness matrix, \mathbf{u} is the nodal displacement vector associated with the real load and Δ_d is the prescribed limit on the displacement value in constraint d .

The side constraints can be stated as

$$\begin{aligned} -t_g + t_{\min} &\leq 0; & (\text{for } g = 1, \dots, G), \\ t_g - t_{\max} &\leq 0; & (\text{for } g = 1, \dots, G). \end{aligned} \quad (3)$$

In order to suppress the intermediate thicknesses, the weight calculation formulation is replaced by $\tilde{W} = \sum_{g=1}^G \gamma_g A_g t_g^{\frac{1}{p}}$ (where p is the penalty parameter and $p \geq 1$). This gives the correct weight value for $t_g = 0$ and $t_g = 1$. The use of the penalty parameter has similar effect in the later formulations as it was the role of the penalty parameter in the classical optimality criteria method.

The optimization problem is to minimize the penalized weight of the structure which is subjected to a given single displacement and side constraints.

$$\begin{aligned} \tilde{W} = \sum_{g=1}^G \gamma_g A_g t_g^{\frac{1}{p}} = \min! \\ \text{subject to } \begin{cases} \mathbf{u}^T \mathbf{K} \mathbf{u} - \Delta \leq 0; \\ -t_g + t_{\min} \leq 0; & (\text{for } g = 1, \dots, G), \\ t_g - t_{\max} \leq 0; & (\text{for } g = 1, \dots, G). \end{cases} \end{aligned} \quad (4)$$

In equation (4) the nodal displacement vector \mathbf{u} associated with the real load \mathbf{P} is calculated from the linear system of equations $\mathbf{K} \mathbf{u} = \mathbf{P}$.

2.1.3. Lagrange function. Using the Lagrange multipliers ν, α_g, β_g and slack variables h_1, h_{2g}, h_{3g} for the constraints in problem (4), the following Lagrange function can be formed:

$$\begin{aligned} \mathcal{L}(t_g, \nu, \alpha_g, \beta_g, h_1, h_{2g}, h_{3g}) = \sum_{g=1}^G \gamma_g A_g t_g^{\frac{1}{p}} + \nu (\mathbf{u}^T \mathbf{K} \mathbf{u} - \Delta + h_1^2) + \\ \sum_{g=1}^G \alpha_g (-t_g + t_{\min} + h_{2g}^2) + \sum_{g=1}^G \beta_g (t_g - t_{\max} + h_{3g}^2). \end{aligned} \quad (5)$$

2.1.4. Kuhn-Tucker conditions. Neglecting the details, one can obtain

$$\begin{aligned} \frac{\partial \mathcal{L}}{\partial t_g} = \frac{1}{p} \gamma_g A_g t_g^{\frac{1-p}{p}} + \nu \left(\frac{\partial \mathbf{u}^T}{\partial t_g} \mathbf{K} \mathbf{u} + \mathbf{u}^T \frac{\partial \mathbf{K}}{\partial t_g} \mathbf{u} + \mathbf{u}^T \mathbf{K} \frac{\partial \mathbf{u}}{\partial t_g} \right) - \alpha_g + \beta_g = 0 \\ (g = 1, \dots, G). \end{aligned} \quad (6a)$$

Due to symmetry of the stiffness matrix \mathbf{K} and other simplifications equation (4) can be replaced by the following relation

$$\frac{\partial \mathcal{L}}{\partial t_g} = \frac{1}{p} \gamma_g A_g t_g^{\frac{1-p}{p}} - \nu \sum_{e=1}^{E_s} u_{ge}^T \frac{\partial K_{ge}}{\partial t_g} u_{ge} - \alpha_g + \beta_g = 0; \quad (g = 1, \dots, G), \quad (6b)$$

where the subscript ge refers to the g -th finite element of the g -th ground element.

If the “normalized” element stiffness matrix is $\tilde{\mathbf{K}}_{ge}$ (e.g. calculated for a unit thickness ($t_g = 1$)), then the element stiffness matrix \mathbf{K}_{ge} for actual thickness t_g is expressed by $\mathbf{K}_{ge} = t_g \tilde{\mathbf{K}}_{ge}$ due to the linear relation and $\frac{\partial \mathbf{K}_{ge}}{\partial t_g} = \tilde{\mathbf{K}}_{ge}$. Introducing

the following notation $R_g = t_g^2 \sum_{e=1}^{E_g} \mathbf{u}_{ge}^T \tilde{\mathbf{K}}_{ge} \mathbf{u}_{ge}$ equation (5) becomes very simple

$$\frac{1}{p} \gamma_g A_g t_g^{\frac{1-p}{p}} - \nu \frac{R_g}{t_g^2} - \alpha_g + \beta_g = 0. \quad (6c)$$

Continuing the derivations:

$$\frac{\partial \mathcal{L}}{\partial \nu} = \mathbf{u}^T \mathbf{K} \mathbf{u} - \Delta + h_1^2 = 0 \quad \text{and} \quad \frac{\partial \mathcal{L}}{\partial h_1} = 2\nu h_1 = 0, \quad (7)$$

$$\frac{\partial \mathcal{L}}{\partial \alpha_g} = -t_g + t_{\min} + h_{2g}^2 = 0 \quad \text{and} \quad \frac{\partial \mathcal{L}}{\partial h_{2g}} = 2\alpha_g h_{2g} = 0, \quad (8)$$

$$\frac{\partial \mathcal{L}}{\partial \beta_g} = t_g - t_{\max} + h_{3g}^2 = 0 \quad \text{and} \quad \frac{\partial \mathcal{L}}{\partial h_{3g}} = 2\alpha_g h_{3g} = 0. \quad (9)$$

Omitting the details from equations (6c), (7), (8) and (9) the values of the Lagrange multipliers, slack variables and the thickness values t_g can be calculated iteratively.

As it is in COC type methods, before the calculation of the Lagrange multiplier ν , one needs to define a range for the thickness: a set of active and passive thicknesses.

There exist three possibilities:

If $t_{\min} < t_g < t_{\max}$ (or the ground element is “active”, $g \in \mathcal{A}$) then $\alpha_g = \beta_g = 0$ and by (6c) the following formula can be obtained

$$t_g = \left(\frac{\nu p R_g}{A_g \gamma_g} \right)^{\frac{p}{p+1}} \quad (10)$$

In case of $t_g = t_{\min}$ the corresponding Lagrange multipliers are $\alpha_g \geq 0$, $h_{2g} = 0$ and (6c) implies

$$t_g \geq \left(\frac{\nu p R_g}{A_g \gamma_g} \right)^{\frac{p}{p+1}} \quad (11)$$

This means that if (10) gives a t_g - value which is smaller than t_{\min} then (6c) is satisfied by $t_g = t_{\min}$. Similarly, in case of $t_g = t_{\max}$ the corresponding Lagrange multipliers are $\beta_g \geq 0$, $h_{3g} = 0$ and then (6c) implies

$$t_g \leq \left(\frac{\nu p R_g}{A_g \gamma_g} \right)^{\frac{p}{p+1}} \quad (12)$$

which allows $t_g = t_{\max}$ when (10) gives a t_g - value which is greater than t_{\max} . If $t_g = t_{\min}$ or $t_g = t_{\max}$ we call the ground element “passive” ($g \in \mathcal{P}$).

2.1.5. Calculation of the final iterative formulas. In order to keep the number and layout of ground elements constant and avoid the ill-conditioned stiffness matrix, one can replace the zero element thickness (t_{\min}) with a small but finite value (e.g.

$t_{\min} = 10^{-6}$). If the single displacement constraint is active in problem (4) (e.g. satisfies the equality sign) the following form holds

$$\Delta - \sum_{g=1}^G \frac{R_g}{t_g} = 0. \quad (13)$$

Since the thickness value for passive elements ($g \in \mathcal{P}$) is given and for active elements ($g \in \mathcal{A}$), it can be calculated from (10) that

$$\Delta - \sum_{g \in \mathcal{P}} \frac{R_g}{t_g} = \sum_{g \in \mathcal{A}} \frac{R_g}{t_g} = \sum_{g \in \mathcal{A}} \frac{R_g}{\left(\frac{\nu p R_g}{A_g \gamma_g} \right)^{\frac{p}{p+1}}} \quad (14)$$

implying

$$\nu^{\frac{p}{p+1}} = \frac{\sum_{g \in \mathcal{A}} \left(\frac{A_g \gamma_g}{p} \right)^{\frac{p}{p+1}} R_g^{\frac{1}{p+1}}}{\Delta - \sum_{g \in \mathcal{P}} \frac{R_g}{t_g}} \quad (\text{for } \mathcal{A} \neq \emptyset). \quad (15)$$

The optimal solution can be obtained by evaluating iteratively the thickness values t_g and the Lagrange-multiplier from (10) and (15).

2.1.6. *The Applied SIMP Algorithm can be defined as follows:*

1. Specify the Max and Min value of t_g , ($t_{g \max} = 1$, $t_{g \min} = 10^{-6}$).
2. Specify a maximum displacement Δ (single displacement).
3. Set the penalty value, $p = 1$, later this value will be incremented to $p = 1.5, 2$, etc.
4. Specify design domain, including supports and loading.
5. Carry out FEM.
6. Extract displacement field for entire structure \mathbf{u}^T .
7. Calculate R_g with displacement vector based on current element solution set t_g , but using the stiffness matrix for the elements as if it had $t_g = 1$.
8. Calculate Lagrange multiplier ν :

$$\nu = \frac{\sum_{g \in \mathcal{A}} \left(\frac{A_g \gamma_g}{p} \right)^{\frac{p}{p+1}} R_g^{\frac{1}{p+1}}}{\left(\Delta - \sum_{g \in \mathcal{P}} \frac{R_g}{t_g} \right)^{\frac{p+1}{p}}} \quad (\text{for } \mathcal{A} \neq \emptyset).$$

9. Calculate new element solution set:

$$t_{g, \text{new}} = \left(\frac{\nu p R_g}{A_g \gamma_g} \right)^{\frac{p}{p+1}}$$

where $\nu^{\frac{p}{p+1}}$ is the Lagrange multiplier calculated in step 8 with the correct power.

10. Determine set of *active* and *passive* elements by the following element limit set:

$$\begin{array}{lll}
 t_{g,new} = t_{\min} & \text{if} & t_{g,new} \leq t_{\min} = 10^{-6}; & e \in \mathcal{P}, \\
 t_{g,new} = t_{\max} & \text{if} & t_{g,new} \geq t_{\max} = 1; & e \in \mathcal{P}, \\
 t_{g,new} = t_{g,new} & \text{if} & t_{\min} \leq t_g \leq t_{\max} = 1; & e \in \mathcal{A}.
 \end{array}$$
11. If active set has changed from the previous iteration, go to step 5, else if *active* set has not changes from pervious iteration go to step 12.
12. Increment p until all the elements become passive or reach the limit for p , using following formula: $p = p + \text{increment}$ (step size is controlled).

In topology optimization the checker-board pattern -what is a numerical artifacts with artificially high stiffness is a big problem. To avoid it as an optimal solution there are several techniques (see e.g. Sigmund and Petersson [28]). Here a simple procedure was used which was published by Gáspár, Lógó and Rozvany [9]. The key point is that all the ground elements in case of disk (a primary meshing provides the so-called ground elements) should sub-divide into further finite elements (secondary elements). For the subdivision it is enough to use 2 by 2 elements. Further number of sub-elements can not improve significantly the final result.

3. Numerical examples

The 100 years old Michell's theory on least-weight trusses [13] provides an optimality criteria formula for a continuum in case of low volume fraction. Since his solution usually consists of an infinite number of members, Prager [16] termed Michell's frameworks "truss-like" structures. The Michell's theory was generalized to other structures by Prager and Rozvany (e.g. [17]). During this century several researcher added further result to this topic, but among them Rozvany's school made the most intensive research on it and published many papers with very significant results (e.g. Rozvany [21,22,24,27]). In this Chapter some new optimal topologies are introduced. The computer program is based on the above mentioned algorithm. 4-nodes quadrilateral and 2 nodes truss FE's are used. In each case the normalized "thickness" of the finite elements is used as design variable and a unit Young's Modulus is applied. The displacement limit is always 150% of initial displacement obtained from the initial design at the load location.

3.1. Example 1. "MBB beam". Consider a rectangular ground structure with hinge support in one end and roller support at the other end (Figure 3). The aspect ratio (height over length) at the initial design is 1 to 4.

The total number of the finite elements is 9600. The applied load is 100 unit at the middle of the top of the design domain. Only 4-nodes quadrilateral FE's are used The penalty parameter p was run from $p = 1$ to $p = 3$ with smooth increasing (increment is 0.25). The Poisson ratio is 0. The exact analytical solution (e.g. Rozvany et al. [21]) is shown in Figure 4.

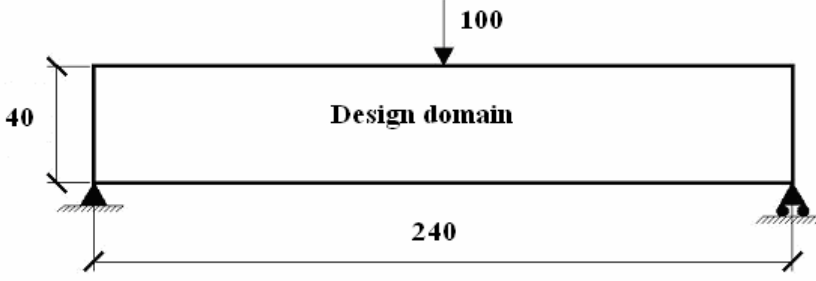


Figure 3. Design domain with boundary conditions



Figure 4. Exact analytical solution after Rozvany et al.

The solution in Figure 5 agrees closely with the exact analytical solution with zero volume fraction. One can see that by the use of 2×2 4-nodes FE's per ground element the checkerboard pattern is completely suppressed (Figure 2).



Figure 5. Optimal topology obtained by numerical calculation

3.2. Example 2. Rectangular domain with unequal point loads and unsymmetrical location. An intensively investigated test structure is rectangular domain with two hinge supports and two point loads [12,21,27]. The usual aspect (height/length) ratio is 0.5 and the supports are located at the middle of the left and right edges, respectively. Sometimes this ratio is not enough because the active zone reaches the top and the bottom edges of the design domain. To avoid this effect the height of the design domain is increased and the aspect ratio is 0.7 (Fig.4.).

In this example the effect of the unsymmetrical location and magnitude of the right hand point loading is investigated. The ratio of magnitudes of the unequal point loads is 2 (left load is 100 units, right load is 50 units). The left hand load is always located at $1/4$ of the horizontal dimension while the location of the right load is varied from

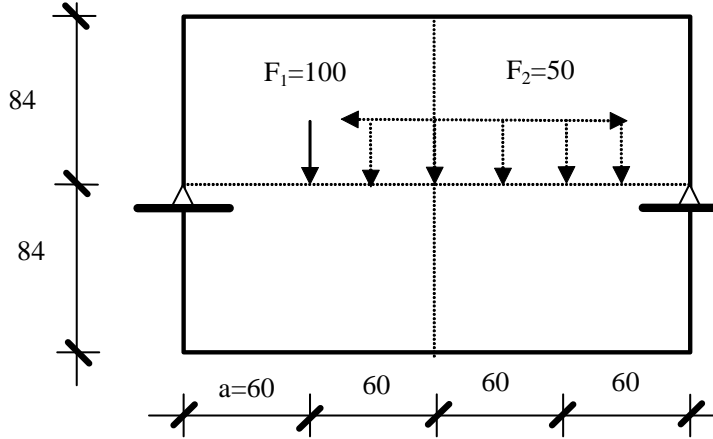


Figure 6. Design domain for variable location of \mathbf{F}_2

2/8 to 7/8 of the horizontal dimension. Total number of finite elements is 40320 by the use of 84×120 ground elements and 2×2 sub-elements. The Poisson ratio is equal to 0. The same type of penalty parameter p was applied (from $p = 1$ to $p = 1.5$ with smooth increasing (increment is 0.1) and later to $p = 3.5$ with increment=0.25).

The pictures of the optimal topologies in function of the right force location can be found in Table 1. The exact analytical solution for zero volume fraction can be seen in Fig.5. after Melchers [12]. The obtained numerical solutions are in good agreement with the analytical solutions.

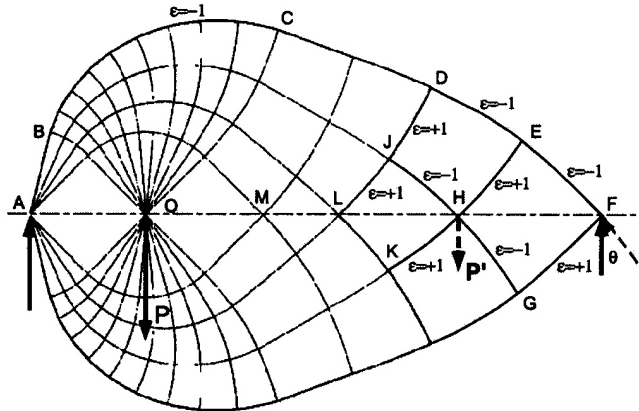
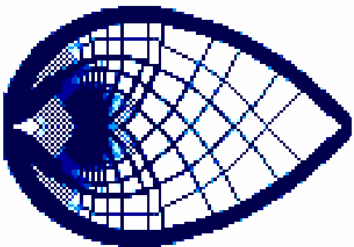
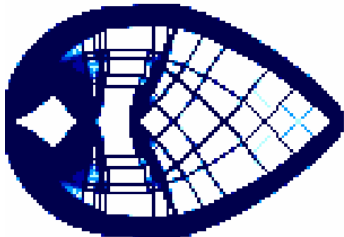
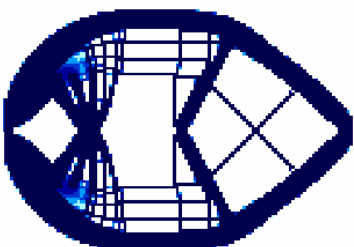
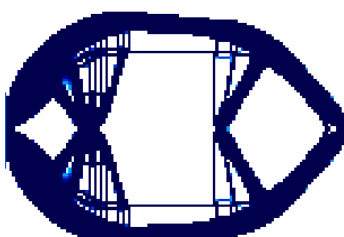
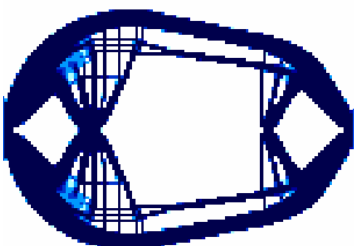
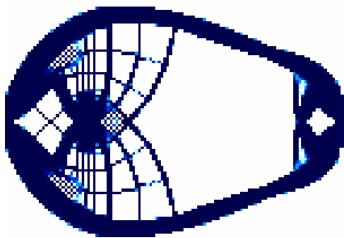


Figure 7. Exact analytical solution after Melchers.

Table 1. Optimal topologies for unsymmetrical loading conditions

Locat ion of F_2	Optimal Solution	Locat ion of F_2	Optimal Solution
1.0a		1.5a	
2.0a		2.5a	
2.5a		3.0	

To demonstrate the evolution of the optimal topologies during the major iterations the intermediate results (correspond to different penalties) are displayed. One can see in Figure that enough a few major iterations to reach the final topologies which proves the robustness of the applied algorithm. At the beginning there are intermediate thicknesses (light colours), what disappears at the end of the program (only two thicknesses exist: 1or 0) .

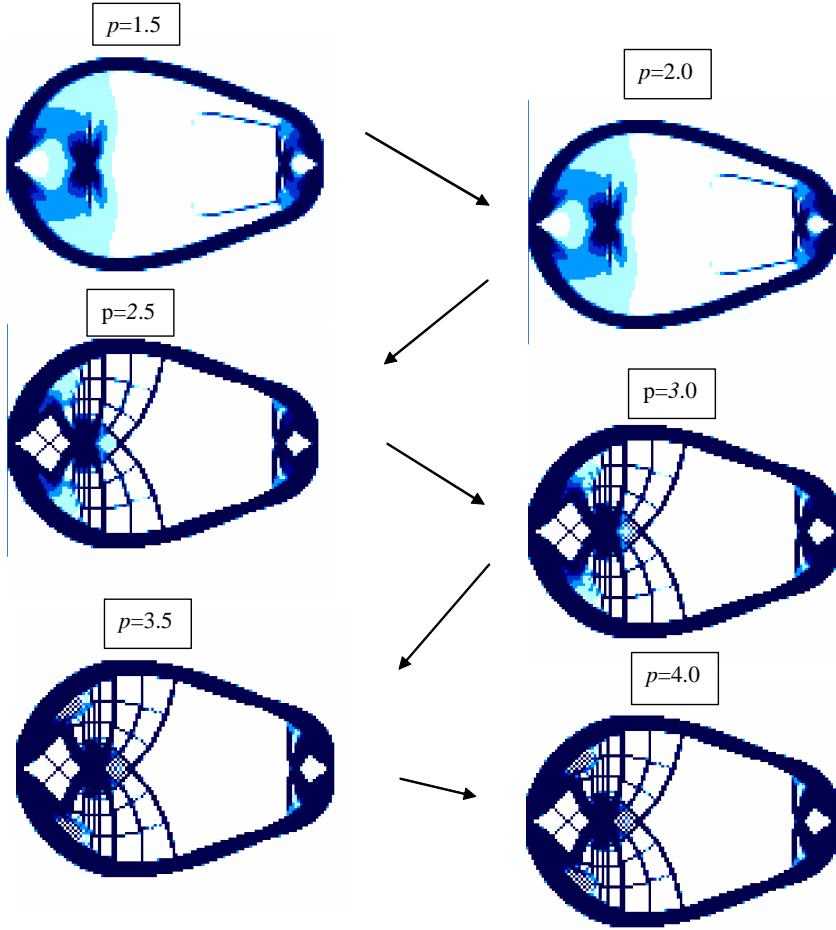


Figure 8. Evolution of the optimal topology in function of the penalty parameter

3.3. Example 3. Topology optimization for variable external forces of nonzero cost. Classical theories of variable force (mostly support) optimization, based on optimality criteria and adjoint displacement fields, were developed in the mid-seventies (see e.g. Rozvany and Mroz [19]. More recently, Buhl [7] and Pomezanski [14], Rozvany et al. [26]) developed numerical methods for topology optimization with allowance for the cost of supports. This example discusses the problem of optimizing structural topologies when some of the external forces are variable and they have a nonzero cost. Such forces may represent a reaction at a support, a force generated by passive control or a ballast (weight) used for increasing cantilever action or modifying natural frequencies. In the presented examples, it is assumed that the cost

of external forces depends on their magnitude and in this way it is proportional to the volume of the optimal topology.

Assuming the same permissible stress in tension and compression, in the objective function of optimization problem (4) the formulation for bars can be reformulate as follows:

$$\min \left(\sum_i k \ell_i |F_i| t_i^{\frac{1}{p}} + \sum_j b \ell_j |R_j| t_j^{\frac{1}{p}} \right); \quad (16)$$

where k and b are given constants, F_i are bar forces and R_j are reaction forces. Replace all supports with a set of bars, such that in the direction of any potential reaction force. (At roller support, for example, we have only one fictitious bar and at a pin support, we have an infinite number of fictitious bars in all possible directions.) It is easy to proof that the optimality conditions become the same as was indicated before.

Let's consider a rectangular design domain with a single point load at middle of the right edge (Figure 10.) On the left side there are fix hinges at the top and the bottom corners and there are pin supports at the 1/4 and 3/4 of the left side, respectively. (Here the "infinite number" of bars means at the pin support that initially there is a

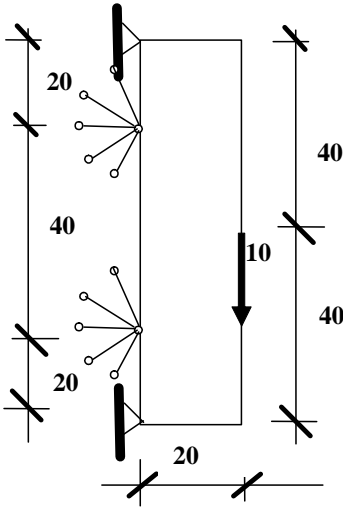


Figure 9. Design domain for variable supports

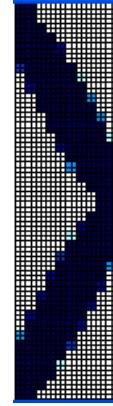


Figure 10. Optimal topology in Case A.

bar in every five degree direction.) The cost of the supports are varied from 1 (no cost) to 10000 (expensive). To demonstrate the method and the algorithm, three cases are presented: Case A: the bars have high cost while the hinges have no cost; Case B: all supports have cost, but the bars have three times more cost than the hinges, Case C: all the supports have same unit cost. For the continuum design domain 4-nodes quadrilateral FE's are used Total number of finite elements is 1600 by the use of 10×40 ground elements and 2×2 sub-elements. The Poisson ration is 0.

Same type of penalty parameter p was applied (from $p = 1$ to $p = 1.5$ with smooth increasing (increment is 0.1) and later to $p = 4.0$ with increment=0.25). The numerical results can be seen in Figures 10-11. They are in good agreement with the expected ones. In Figures 12-13. among the bar supports only one member at the bottom and one member at above are active. Their directions are 135 and 225 degree, respectively.

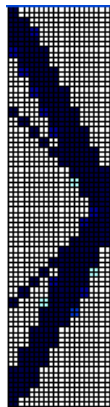


Figure 11. Optimal topology in Case B.



Figure 12. Optimal topology in Case C.

4. Conclusion

A very efficient iterative algorithm was presented for topology design of continuum type structures by the use of displacement constraint. The derived algorithm is suitable for support design as well. The applied meshing provides a good technique to avoid the checkerboard pattern. By the use of the smooth penalization increment the obtained numerical solutions are in good agreement with the existing and proved analytical solutions. Conceptually this topology design is simple, since the algorithm does not require intensive mathematics. The number of the design variables (thousands) significantly exceeds the maximum number of variables what can be used in any kind of mathematical programming algorithm. The main disadvantage is that the buckling and other constraints are not taken into consideration during the optimization procedure but the obtained numerical topologies are a good starting points for further optimal design. The support optimization technique is suitable to demonstrate the effects of strengthening of structures.

Acknowledgement. The present study was supported by the Hungarian National Scientific and Research Foundation (OTKA) (grant T 037922) and the Bolyai Janos Scholarship.

References

1. ALLAIRE, G.; KOHN, R.: *Topology Optimization and Optimal Shape Design Using Homogenization*. In: Bendsoe, M.P.; Mota Soares, C.A. (eds.) *Topology Design of Structures* (Proc. NATO ARW, Sesimbra, Portugal 1992), Dordrecht: Kluwer, (1993), 207-218.

2. BARTA, J.: On the minimum weight of certain redundant structures, *Acta Tech. Acad. Sci. Hung.*, V.18, (1957), 67-76.
3. BENDSOE, M. P. and KIKUCHI, N.: Generating optimal topologies in structural design using a homogenization method. *Comp. Meth. Appl. Mech. Eng.* **71**, (1988), 197-224.
4. BENDSOE, M.P. and MOTA SOARES, C. A.: *Topology Design of Structures* (Proc. NATO ARW, Sesimbra, Portugal, 1992), Dordrecht, Kluwer, 1993.
5. BENDSOE, M. P. and SIGMUND, O.: *Topology Optimization: Theory, Methods and Applications*. Berlin: Springer, 2003.
6. BERKE, L.: *An Efficient Approach to the Minimum Weight Design of Deflection Limited Design*, AFFDL-TM-70-4-FDTR, (1970), Wright-Patterson AFB.
7. BUHL, T.: Simultaneous topology optimization of structure and supports. *Struct. Multidisc. Optim.*, **23**, (2002), 336-346.
8. CHENG, K. T. and OLHOFF, N.: An investigation concerning optimal design of solid elastic plates. *Int. J. Solids Struct.*, **17**, (1981), 305-323.
9. GÁSPÁR, Zs., LÓGÓ, J. and ROZVANY, G. I. N.: On design-dependent constraints and singular topologies. *Struct. and Multidisc. Opt.*, **24**(4), (2002), 338-342.
10. KALISZKY, S. and LÓGÓ, J.: Optimal design of dynamically loaded reinforced concrete frames under displacement and rotation constraints. *Journal of Structural Optimization*, **3**, (1991), 121-131.
11. LÓGÓ, J. and GHAEMI, M.: *Topology optimization by SIMP method*. Proc. of the Conference on Numerical Methods and Computational Mechanics, Miskolc, Hungary, July 15-19, (2002), 165-166.
12. MELCHERS, R. E.: On extending the range of michell-like optimal topologies structures. *Structural and Multidisc. Optimization*, **29**(2), (2005), 85-92.
13. MICHELL, A. G. M.: The limits of economy of material in frames structures. *Phil. Mag.*, **8**, (1904), 589-597.
14. POMEZANSKI, V.: Changing the connections of structural elements during an optimization process, *Journal of Computational and Applied Mechanics*, **5**(1), (2004), 117-127.
15. PRAGER, W. and TAYLOR, J. E.: Problems of optimal structural design. *J. Appl. Mech. ASME*, **35**, (1968), 122-106.
16. PRAGER, W.: *Introduction to Structural Optimization*. CISM Courses and Lectures Notes 212, Springer Verlag, Wien-New York, 1974.
17. PRAGER, W. and ROZVANY, G. I. N.: Optimal layout of grillages. *J. Struct. Mech.*, **5**, (1977), 1-18.
18. ROSSOW, M. P. and TAYLOR, J. E.: A finite element method for the optimal design of variable thickness sheets. *J. AIAA*, **11**, (1973), 1566-1569.
19. ROZVANY, G. I. N. and MROZ, Z.: Column design: Optimization of support conditions and segmentation. *J. Struct. Mech.*, **5**, (1977), 279-290.
20. ROZVANY, G. I. N.: *Structural Design via Optimality Criteria*. Kluwer Academic Publisher, Dordrecht, 1989.
21. ROZVANY, G. I. N., BENDSOE, M. P. and KIRSH U.: Layout optimization of structures. *Appl. Mech. Reviews.*, **48**(2), (1995), 41-118.

-
22. ROZVANY, G. I. N.: Some shortcomings in Michell's truss theory, *Struct. Optim.*, **12**, (1996) 244-250.
 23. ROZVANY, G. I. N.: *Optimization in Structural Mechanics*. CISM Courses and Lectures Notes 374, Springer Verlag, Wien-New York, 1997.
 24. ROZVANY, G. I. N., GOLLUB, W. and ZHOU, M.: Exact Michell trusses for various combinations of line supports. Part II, *Struct. Optim.*, **14**, (1997), 138-149.
 25. ROZVANY, G. I. N.: stress ratio and compliance based methods in topology optimization - a critical review. *Structural and Multidisc. Optimization*, **21**, (2001), 109-119.
 26. ROZVANY, G. I. N., LÓGÓ, J. and KALISZKY, S.: *Topology Optimization for Variable External Forces of Nonzero Cost*. Proc. of 5th World Congress of Structural and Multidisciplinary ptimization, May 19-23, 2003, Lido di Jesolo, Venice, Italy. 323-324.
 27. ROZVANY, G. I. N., LÓGÓ, J. and QUERIN, O. M.: *New Classes of Analytically Derived Optimal Topologies and Their Numerical Confirmation*, XXI International Congress of Theoretical and Applied Mechanics, Warsaw, Poland, August 15-21, 2004.
 28. SIGMUND, O. and PETERSSON, J.: Numerical Instabilities in Topology Optimization: A Survey on Procedures Dealing with Checkerboards, Mesh-dependencies and Local Minima. *Struct. Optim.* **16**, (1998), 68-75.
 29. TAYLOR, J. E.: Strongest column: an energy approach. *J. APPL. MECH.*, **89**(2), (1967), 486-487.
 30. ZHOU M. and ROZVANY, G. I. N.: The COC Algorithm, Part II: Topological, Geometrical and Generalized Shape Optimization. *Comp. Meth. Appl. Mech. Eng.* **89**, (1991), 309-336.

QUADRATIC FLOW PAST AXIALLY SYMMETRIC BODIES AT LOW REYNOLDS NUMBER: A NEW APPROACH

DEEPAK KUMAR SRIVASTAVA, NIRMAL SRIVASTAVA

Department of Mathematics, B.S.N.V. Post Graduate College(University of Lucknow)
Station Road, Charbagh, Lucknow(U.P.)-226001, India
dksflow@hotmail.com, nirmalsri.25@gmail.com

RAJA RAM YADAV

Department of Mathematics, University of Lucknow, Lucknow(U.P.)-226007, India
yadav_rr2@yahoo.co.in

[Received: September 27, 2012]

Abstract. In this paper, a new approach to tackle the quadratic flow past axially symmetric bodies at low Reynolds number is presented. Firstly, a new method for the evaluation of drag based on DS conjecture (Datta and Srivastava, [1, 1999]) and surface average velocity defined by Chwang and Wu (part 2 and 3 [2, 3, 1975]) on a body placed in quadratic flows like parabolic and stagnation like parabolic is presented. Later on, these general values of drag are utilized for bodies like sphere, spheroid and egg-shaped in both axial and transverse situations. Author claims that the proposed method is easy and very handy to study the quadratic flow past not only for a isolated body but also for assemblage of bodies situated along the axis of symmetry in comparison to complicated methods like distribution of basic singularities which is not applicable to all axially symmetric bodies except sphere and spheroidal bodies. Numerical values of drag in every flow situation have been calculated and presented in Tables 1-9. The respective variations with respect to eccentricity 'e' are depicted via figures. Limiting cases of slender spheroid and flat circular disk are also discussed.

Mathematical Subject Classification: 76D07

Keywords: Quadratic flows, parabolic flow, stagnation like parabolic flow, Stokes drag

1. INTRODUCTION

In physical and biological science, and in engineering, there is a wide range of problems of interest like sedimentation problem, lubrication processes etc. concerning the flow of a viscous fluid in which a solitary or a large number of bodies of microscopic scale are moving, either being carried about passively by the flow, such as solid particles in sedimentation, or moving actively as in the locomotion of micro-organisms. In the case of suspensions containing small particles, the presence of the particles will influence the bulk properties of the suspension, which is a subject of general interest in Rheology. In the motion of micro-organisms, the propulsion velocity depends critically on their body shapes and modes of motion, as evidenced in the flagellar and

cilliary movements and their variations. A common feature of these flow phenomena is that the motion of the small objects relative to the surrounding fluid has a small characteristic Reynolds number Re . Typical values of Re may range from order unity, for sand particles settling in water, for example, down to 10^{-2} to 10^{-6} , for various micro-organisms. In this low range of Reynolds numbers, the inertia of the surrounding fluid becomes insignificant compared with viscous effects and is generally neglected and the Navier-Stokes equations of motion reduce to the Stokes equations as a first approximation. The zero Reynolds number flow is called Stokes flow. The hydromechanics of low Reynolds number flows play an important role in the study of rheology, lubrication theory, micro-organism locomotion and many areas of biophysical and geophysical interest. In the case when the inertial effects are negligible compared with the viscous forces, the Navier-stokes equations are usually simplified to Stokes equations as a first approximation. Determination of the solutions for the Stokes flows, however, is still recognized to be difficult in general for arbitrary body shapes. As a consequence, not many exact solutions are known. Of the few analytical methods available for solving Stokes flow problems, one is the boundary value method, which is based on the choice of an appropriate co-ordinate system to facilitate separation of the variables for the body geometry under consideration. Another is the singularity method, whose accuracy depends largely on whether the correct types of singularity are used and how their spatial distributions are chosen. The boundary value method seems to have been widely adopted in practice, more so than the singularity method. Stokes flow of an arbitrary body is of interest in biological phenomena and chemical engineering. In fact, the body with simple form such as sphere or ellipsoid is less encountered in practice. The body, which is presented in science and technology, often takes a complex arbitrary form. For example, under normal condition, the erythrocyte is a biconcave disk in shape, which can easily change its form and present different contour in blood motion due to its deformability. In second half of twentieth century, a considerable progress has been made in treating the Stokes flow of an arbitrary body.

An exact solution for the motion of a spheroidal particle placed in a quadratic as well as in a linear flow of incompressible viscous fluid is very useful in the study of blood flow and general suspension rheology. In particular, a correct description of the behavior of a spheroidal particle in a paraboloidal or Poiseuille flow will facilitate accurate calculation of the bulk flow properties of tube flows of dilute or concentrated suspensions of blood cells, long-chain polymers or any other biological supra-macromolecules. When the Reynolds number based on the particle size, the local flow velocity and the kinematic viscosity of the surrounding fluid is very small, as in the case of microcirculation of blood cells, the inertial effects of the fluid can be neglected and the Navier-Stokes equations of motion reduce to the Stokes equations as a first approximation.

All these motions are characterized by low Reynolds numbers and are described by the solution of the Stokes equations. Although the Stokes equations are linear, to obtain exact solutions to them for arbitrary body shapes or complicated flow conditions is still a formidable task. There are only relatively few problems in which it is possible

to solve exactly the creeping motion equations for flow around a single isolated solid body. Stokes [4, 1851] calculated the flow around a solid sphere undergoing uniform translation through a viscous fluid whilst Oberbeck [5, 1876] solved the problem in which an ellipsoid translates through liquid at a constant speed in an arbitrary direction. Edwards [6, 1892], applying the same technique, obtained the solution for the steady motion of a viscous fluid in which an ellipsoid is constrained to rotate about a principal axis. The motion of an ellipsoidal particle in a general linear flow of viscous fluid at low Reynolds number has been solved by Jeffery [7, 1922], whose solution was also built up using ellipsoidal harmonics. The analysis described by Jeffery extended further by Taylor [8, 1923]. Goldstein [9, 1929] obtained a force on a solid body moving through viscous fluid. Lighthill [10, 1952] studied the problem of squirming motion of nearly spherical deformable bodies through liquids at very small Reynolds number. Hill and Power [11, 1956] have obtained arbitrarily closed approximations of drag by proving a complimentary pair of extremum principles for a Newtonian viscous fluid in quasi-static flow.

In a series of studies over low-Reynolds-number-flow, Chwang and Wu [12, part 1, 1974] have developed an effective method of solution for arbitrary body shapes. In this first part authors have considered the viscous flow generated by pure rotation of an axisymmetric body having an arbitrary prolate form, the inertia forces being assumed to have a negligible effect on the flow. The method of solution explored in this paper is based on a spatial distribution of singular torques, called rotlets, by which the rotational motion of a given body can be represented. Exact expressions of torque are determined in closed form for a number of body shapes, including the dumbbell profile, elongated rods and some prolate forms. Chwang and Wu [2, part 2, 1975] explored the fundamental singular solutions for Stokes flow that could be useful for constructing solutions over a wide range of free-stream profiles and body shapes. Authors have employed these fundamental singularities (Stokeslet and their derivatives like rotlets, stresslets, potential doublets and higher orderpoles) to construct exact solutions to a number of exterior and interior Stokes-flow problems for several specific body shapes translating and rotating in a viscous fluid which may itself be providing a primary flow. The different primary flows considered here include the uniform stream, shear flows, parabolic profiles and extensional flows(hyperbolic profiles), while the body shapes cover prolate spheroids, spheres and circular cylinders. Chwang [3, part 3, 1975] has been found exact solutions in closed form (expressions of drag) using singularity method for various quadratic flows of an unbounded incompressible viscous fluid at low Reynolds numbers past a prolate spheroid with an arbitrary orientation with respect to the fluid. The quadratic flows considered here include unidirectional paraboloidal flows, with either an elliptic or a hyperbolic velocity distribution, and stagnation-like quadratic flows as typical representations. Chwang and Wu [13, part 4, 1975] have analyzed the problem of a uniform transverse flow past a prolate spheroid of arbitrary aspect ratio at low Reynolds numbers by the method of matched asymptotic expansions. They have found expressions of drag depending on two Reynolds numbers, one based on the semi-minor axis b , $R_b = Ub/\nu$, and the other on the semi-major axis a , $R_a = Ua/\nu$. Ho and Leal [15, 1976] considered the

migration of a rigid sphere in a two-dimensional unidirectional shear flow of a second order fluid. Chan and Leal [31, 1977] wrote a note on the motion of a spherical particle in a general quadratic flow of a second order fluid. Parker [16, 1977] considered the two-dimensional motion of a projectile experiencing a constant gravitational force and a fluid drag force which is quadratic in the projectiles speed. Johnson and Wu [14, part 5, 1979] elucidated the characteristics of the general stokes flow for slender bodies of finite centre-line curvature. The singularity method for Stokes flow has been employed by authors to construct the solutions to the flow past a slender torus.

Majhi and Vasudevaiah [17, 1982] considered the axisymmetric parabolic shear flow past a spinning sphere in an unbounded viscous medium using the matching technique and taking the non-uniform shear as the dominant feature, where the Reynolds number based on parabolic shear $Re \leq 1$ and rotational Reynolds number based on the angular rotation of sphere $Ro \leq 1$ are such that $Ro^2/Re = O(1)$. Kaloni [18, 1983] studied the motion of a rigid sphere, suspended in micropolar fluid which is undergoing a slow unidirectional two-dimensional flow. Keh and Anderson [19, 1984] obtained the configurational distribution function of dumbbell macromolecules (rigid and linearly elastic) in a quadratic rectilinear flow. Yuan and Wu [20, 1987] obtained the analytic expressions in closed form for flow field by distributing continuously the image Sampsonlets with respect to the plane and by applying the constant density, linear and the parabolic approximation. Yang and Hong [21, 1988] found exact solutions in closed form using the eigen function-expansion method for various linear and quadratic flows of an unbounded incompressible viscous liquid at low Reynolds number past a porous sphere with a uniform permeability distribution. Seki [22, 1996] studied the motion of a rigid ellipsoidal particle freely suspended in a Poiseuille flow (parabolic flow) of an incompressible Newtonian fluid through a narrow tube numerically in the zero-Reynolds-number limit. Haber and Brenner [23, 24, 1984, 1999] investigated analytically the quasi-steady hydrodynamic Stokes drag force and torque exerted on each of N non-identical particles immersed in a general quadratic undisturbed flow field at infinity. Datta & Srivastava [1, 1999] advanced a new approach to evaluate the drag force in a simple way on a restricted axially symmetric body placed in a uniform stream (i) parallel to its axis, (ii) transverse to its axis, when the flow is governed by the Stokes equations under no-slip boundary conditions. Authors have evaluated the analytic closed form expressions of drag for spheroids, deformed sphere, cycloidal body, an egg-shaped body. Palaniappan and Daripa [25, 2000] have found exact analytical solutions for the steady state creeping flow in and around a vapor-liquid compound droplet, consisting of two orthogonally intersecting spheres of arbitrary radii (a and b), submerged in axisymmetric extensional (hyperbolic) and paraboloidal flows of fluid with viscosity μ . Lin et al. [26, 2005] studied the hydrodynamic interaction between two neutrally-buoyant smooth spheres moving at negligible Reynolds numbers in an unbounded plane Poiseuille flow calculated by three-dimensional boundary element (BEM) simulations. Pasol et al. [27, 2006] provided comprehensive results for the creeping flow around a spherical particle in a viscous fluid close to a plane wall, when the external velocity is parallel to the wall and varies as a second degree polynomial in the coordinates. By using bipolar coordinates technique, authors have

concluded that by linearity of Stokes equations, the solution is a sum of flows for typical unperturbed flows: a pure shear flow, a ‘modulated shear flow’, for which the rate of shear varies linearly in the direction normal to the wall, and a quadratic flow. Prakash et al. [28, 2012] studied the hydrodynamics of a porous sphere in an oscillatory viscous flow of an incompressible Newtonian fluid. Authors have derived the Faxen’s law for drag and torque acting on the surface of the porous sphere. In the later part of the paper, examples of uniform flow, oscillating Stokeslets, oscillatory shear flow and quadratic shear flow are discussed.

In the present paper, author tried to advanced the own conjecture (Datta & Srivastava [1, 1999]) to evaluate the closed form analytic expressions of drag over axisymmetric bodies placed under different primary flows including uniform stream, parabolic profiles and stagnation like parabolic profiles by considering the surface average of the primary flow velocity. This conjecture is briefly explained in Section 2. Reader is advisable to go through the author’s (Srivastava et al., [29, 2012]) recently published paper for complete detail regarding its application to class of oblate bodies.

2. BODY GEOMETRY AND METHOD

2.1. Geometry of the body. Let us consider the axially symmetric body of characteristic length L placed along its axis (x-axis, say) in a uniform stream U of viscous fluid of density ρ_1 and kinematic viscosity ν . When the Reynolds number UL/ν is small, the motion is governed by the Stokes equations (Happel and Brenner, [30, 1964]),

$$\mathbf{0} = - \left(\frac{1}{\rho_1} \right) \text{grad } p + \nu \nabla^2 \mathbf{u}, \quad \text{div } \mathbf{u} = 0 \quad (2.1)$$

subject to the no-slip boundary condition.

We have taken up the class of those axially symmetric bodies which possesses continuously turning tangent, placed in a uniform stream U along the axis of symmetry (which is x-axis), as well as constant radius b of maximum circular cross-section at the mid of the body. This axi-symmetric body is obtained by the revolution of meridional plane curve (depicted in Figure 1) about axis of symmetry which obeys the following limitations:

- i. Tangents at the points A, on the x-axis , must be vertical,
- ii. Tangents at the points B, on the y-axis , must be horizontal,
- iii. The semi-transverse axis length ‘b’ must be fixed.

The point P on the curve is may be represented by the Cartesian coordinates (x, y) or polar coordinates (r, θ) respectively , PN and PM are the length of tangent and normal at the point P. The symbol R stands for the intercepting length of normal between the point on the curve and point on axis of symmetry and symbol α is the slope of normal PM which can be vary from 0 to π .

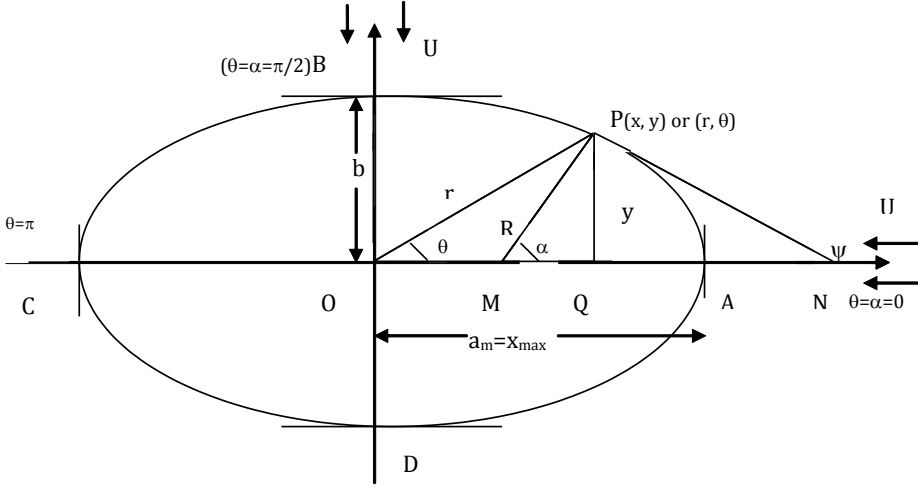


Figure 1. Geometry of the axially symmetric body

2.2. Axial flow. The expression of Stokes drag on such type of axially symmetric bodies placed in axial flow (uniform flow parallel to the axis of symmetry) is given by (Datta & Srivastava [1, 1999])

$$F_{||} = \frac{1}{2} \frac{\lambda b^2}{h_{||}}, \quad \text{where} \quad \lambda = 6\pi\mu U_{||} \quad (2.2)$$

and

$$h_{||} = \left(\frac{3}{8}\right) \int_0^\pi R \sin^3 \alpha \, d\alpha. \quad (2.3)$$

where the suffix $||$ has been introduced to assert that the force is in the axial direction.

Sometimes it will be convenient to work in Cartesian co-ordinates. Therefore, referring to Figure 1 for the profile geometry, we have

$$y = R \sin \alpha, \quad \tan \alpha = - \left(\frac{dy}{dx} \right)^{-1} = - \frac{dx}{dy} = -x'. \quad (2.4)$$

Using above transformation, we may express (2.3) as

$$h_{||} = -\frac{3}{4} \int_0^a \frac{yy''}{(1 + (y')^2)^2} dx \quad (2.5)$$

where $2a_m$ represents the axial length of the body and dashes represents derivatives with respect to x . In the sequel, it will be found simpler to work with y as the independent variable. Thus, $h_{||}$ assumes the form

$$h_{||} = -\frac{3}{4} \int_0^b \frac{y(x')^2 x''}{(1 + (x')^2)^2} dy \quad (2.6)$$

where dashes represents derivatives with respect to y .

2.3. Transverse flow. The expression of Stokes drag on such type of axially symmetric bodies placed in transverse flow (uniform flow perpendicular to the axis of symmetry) is given by (Datta & Srivastava [1, 1999])

$$F_{\perp} = \left(\frac{1}{2}\right) \frac{\lambda b^2}{h_y} \quad \text{where} \quad \lambda = 6\pi\mu U_{\perp}, \quad (2.7)$$

and

$$h_{\perp} = \left(\frac{3}{16}\right) \int_0^{\pi} R (2 \sin \alpha - \sin^3 \alpha) d\alpha. \quad (2.8)$$

According to the same manner as we did in axial flow equation (2.8) may also be written in Cartesian form as (in both cases having x and y treated as independent)

$$h_{\perp} = -\frac{3}{8} \int_0^a \frac{yy'' [1 + 2(y')^2]}{[1 + (y')^2]^2} dx, \quad (2.9)$$

and

$$h_{\perp} = -\frac{3}{8} \int_0^b \frac{yx'' [2 + (x')^2]}{[1 + (x')^2]^2} dy \quad (2.10)$$

In (2.9) and (2.1) the dashes represents derivatives with respect to x and y respectively. The suffix \perp has been placed to designate the force due to the external flow along the y -axis, the transverse direction.

The proposed conjecture is, of, course, subject to restrictions on the geometry of the meridional body profile $y(x)$ of continuously turning tangent implying that $y'(x)$ is continuous together with $y''(x) \neq 0$, thereby avoiding corners or sharp edges or other kind of nodes and straight line portions, $y = ax + b$, $x_1 \leq x \leq x_2$. Also, it should be noted here that the method holds good for convex axially symmetric bodies which possesses fore-aft symmetry about the equatorial axis perpendicular to the axis of symmetry(polar axis). Apart from this argument, It is interesting to note here that the proposed conjecture is applicable also to those axi-symmetric bodies which fulfills the condition of continuously turning tangent but does not possesses fore-aft symmetry like egg shaped body (Datta & Srivastava [1, 1999]). By using these formulae of drag, Srivastava et al. [30, (2012)] have calculated the expressions of drag on the deformed sphere up to second order deformation parameter and later on oblate spheroid and flat circular disk as a special case. This conjecture is much simpler to evaluate the numerical values of drag than other existing numerical methods like Boundary Element Method (BEM), Finite Element Analysis (FEA) etc. as it can be applied to a large set of convex axi-symmetric bodies possessing fore-aft symmetry about maximal radius situated in the middle of the body for which analytical solution is not available or impossible to evaluate.

Since both axial and transverse flows have been considered in a free stream results of the force at an oblique angle of attack may be resolved into its components to get

the required result. The present analysis can be extended to generate a drag formula for axi-symmetric bodies for more complex flows like paraboloidal flow for which free stream may be represented by surface average velocity (Chwang and Wu [2, part 2, 1974]). The present analysis may be extended to generate a drag formula for axi-symmetric bodies for more complex flows like paraboloidal flow and stagnation like paraboloidal flow for which free stream may be represented by surface average velocity (Chwang and Wu [2, part 2, 1974]).

3. FORMULATION OF THE PROBLEM

(Chwang and Wu [2, part 2, 1974]) have constructed the exact solutions to a number of exterior and interior Stokes-flow problems by employing fundamental singularities (Stokeslets, rotlets, stresslets, potential doublets and higher order poles) for several specific body shapes translating and rotating in a flow other than primary flow include the uniform stream, shear flows, parabolic profiles and extensional flows(hyperbolic profiles), while the body shapes cover prolate spheroids, spheres and circular cylinders. Just after this paper, Chwang [3, part 3, 1975]) extended the analysis and considered the quadratic flows including unidirectional paraboloidal flows, with either an elliptic or a hyperbolic velocity distribution, and stagnation-like quadratic flows as typical representations. Each of these exact solutions (in closed form) regarding the types of singularities required the construction of a solution in each specific form; their distribution densities are not easily attainable always.

The immediate aim of this problem is to reduce this complexity and to evaluate the exact solution(closed form) by using the DS conjecture (Datta & Srivastava [1, 1999]). In Section 2, we have briefly explained the formulas for evaluating drag on axially symmetric bodies placed under axial flow (flow is along the axis of symmetry) and transverse flow(along the direction perpendicular to axis of symmetry) and in **Section 4**, we explain the extension of this conjecture further for quadratic flows including parabolic flow (Figures 2 and 3) and stagnation like parabolic flow Figures 5 and ??).

4. QUADRATIC FLOW PAST AXIALLY SYMMETRIC BODIES

4.1. Axial paraboloid flow(or unbounded longitudinal paraboloidal flow).

We consider an axi-symmetric body placed under a flow (Figure 2) with a paraboloidal velocity profile

$$U_{\text{paraboloid}} = K(y^2 + z^2) \quad (4.1)$$

$$\text{or } = K(\alpha y^2 + z^2) \quad (4.2)$$

along the axis of symmetry which is the x -axis, where K is arbitrary constant and α is also arbitrary constant may be positive or negative indicating that paraboloidal flow is either elliptic or hyperbolic. When α vanishes, the paraboloidal flow degenerates into a two-dimensional parabolic flow. For arbitrary positive values of α , it represents Hagen-Poiseuille flow through a pipe of elliptic cross-section. If $\alpha = 1$, it becomes

a paraboloidal flow of revolution which corresponds to Heigen-Poiseuille flow in a circular tube. Hyperbolic paraboloidal flow ($\alpha < 0$) may not exist physically, but it can certainly serve as a local component of a more complicated flow field.

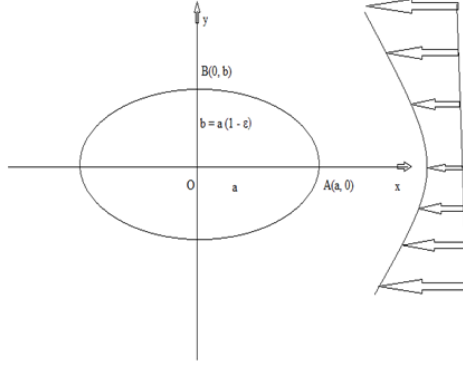


Figure 2. A longitudinal or axial paraboloidal flow past axisymmetric body

By DS-conjecture (Datta & Srivastava [1, 1999]), the expression of drag on axially symmetric body placed in axial uniform stream U (from equations (2.2) and (2.3)) is

$$F_x = \frac{1}{2} \frac{\lambda b^2}{h_x}, \quad \text{where} \quad \lambda = 6\pi\mu U_x \quad (4.3)$$

and

$$h_x = \left(\frac{3}{8}\right) \int_0^\pi R \sin^3 \alpha d\alpha. \quad (4.4)$$

where the suffix x has been introduced to assert that the force is in the axial direction. Now equation (4.1) may be re-written as

$$F_x = \frac{1}{2} \frac{(6\pi\mu) b^2}{h_x} U_x = \frac{3\pi\mu b^2}{h_x} U_e, \quad (4.5)$$

where U_e is precisely the surface average of the primary flow velocity

$$U = K r^2 = K(y^2 + z^2) \quad (4.6)$$

over a surface of axi-symmetric body (conjectured by Chwang and Wu [2, part 2, 1975], b is largest cross-section radius situated at the middle of the body and h_x is given by equation (4.2).

4.2. Transverse paraboloid flow. We consider an axi-symmetric body placed under a flow (Figure 3) with a paraboloidal velocity profile

$$U_{\text{paraboloid}} = K(x^2 + z^2) \quad (4.7)$$

$$\text{or} = (\beta x^2 + z^2) \quad (4.8)$$

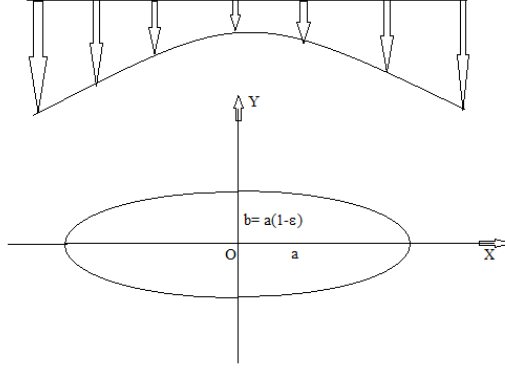


Figure 3. A transverse paraboloid flow past axisymmetric body

along axis of symmetry which is y -axis, where K and β are arbitrary constants.

The expression of Stokes drag on such type of axially symmetric bodies placed in transverse flow (uniform flow perpendicular to the axis of symmetry) is given by (Datta & Srivastava [1, 1999])

$$F_y = \frac{1}{2} \frac{\lambda b^2}{h_y} \quad \text{where} \quad \lambda = 6\pi\mu U_y, \quad (4.9)$$

and

$$h_y = \left(\frac{3}{16} \right) \int_0^\pi R (2 \sin \alpha - \sin^3 \alpha) d\alpha. \quad (4.10)$$

Now equation (4.7) may be re-written as

$$F_y = \frac{1}{2} \frac{(6\pi\mu) b^2}{h_y} U_y = \frac{3\pi\mu b^2}{h_y} U_e, \quad (4.11)$$

where U_e is precisely the surface average of the primary flow velocity

$$U = Kr^2 = K(x^2 + z^2) \quad (4.12)$$

over a surface of axis-symmetric body (conjectured by Chwang and Wu [2, part 2, 1975]), b is largest cross-section radius situated at the middle of the body, and h_y is given by equation (4.8).

Now, we apply the expressions (4.3) and (4.9) to evaluate drag on axially symmetric bodies like sphere, spheroid and egg-shaped body placed under longitudinal unbounded paraboloid and transverse unbounded paraboloid flows.

5. SPHERE

5.1. Axial Flow. We shall consider a sphere having a radius a placed under axial paraboloidal flow velocity $U_{\text{paraboloid}} = K(y^2 + z^2)$, by considering the surface average velocity $U_e = 2Ka^2/3$, over a spherical surface $R = a$, the value of $h_x = a/2$ (from equation (4.2)), the expression of drag on comes out to be (with the use of equation (4.3))

$$F_x = \frac{3\pi\mu b^2}{h_x} U_e = \frac{3\pi\mu a^2}{\frac{a}{2}} \left(\frac{2}{3} Ka^2 \right) = 4\pi\mu Ka^3. \quad (5.1)$$

which matches with that obtained by Chwang and Wu ([2, part 2, 1975, p. 807, Eq. (69)]) treated with singularity method.

5.2. Transverse flow. Here we shall consider again a sphere having a radius a placed under transverse paraboloidal flow velocity $U_{\text{paraboloid}} = K(x^2 + z^2)$, by considering the surface average velocity $U_e = 2Ka^2/3$, over a spherical surface $R = a$, the value of $h_y = a/2$ (from equation (4.8)), the expression of drag on sphere comes out to be (with the use of equation (4.3))

$$F_y = \frac{3\pi\mu b^2}{h_y} U_e = \frac{3\pi\mu a^2}{\frac{a}{2}} \left(\frac{2}{3} Ka^2 \right) = 4\pi\mu Ka^3. \quad (5.2)$$

6. PROLATE SPHEROID

6.1. Axial Flow. We consider a prolate spheroid

$$\frac{x^2}{a^2} + \frac{\rho^2}{b^2} = 1, \quad \rho^2 = y^2 + z^2, \quad a \geq b, \quad c = \sqrt{a^2 - b^2} = ea, \quad 0 \leq e \leq 1 \quad (6.1)$$

having semi-major axis a and semi-minor axis b , e as eccentricity, and c as distance of focus from centre, placed under axial paraboloidal flow velocity $U_{\text{paraboloid}} = (\alpha y^2 + z^2)$ along x-axis, and for $\alpha \neq 1$, the surface average velocity U_e , over a spheroidal surface (6.1) is

$$U_e = \frac{1}{3} (1 + \alpha) (1 - e^2) a^2, \quad (6.2)$$

the value of h_x (from equation (4.2)) is

$$h_x = \frac{3b^2}{16ae^3} [-2e + (1 + e^2) L], \quad L = \log \frac{1+e}{1-e}. \quad (6.3)$$

For $\alpha \neq 1$, the expression of drag on prolate spheroid (6.1) in axial or longitudinal paraboloid flow may be obtained from (4.3) by utilizing the values of U_e from (6.2) and h_x from (6.3) as

$$F_x = \frac{16\pi\mu (1 + \alpha) e^3 a^3 (1 - e^2)}{3 [-2e + (1 + e^2) L]}, \quad (6.4a)$$

the expression of drag coefficient, for $\alpha \neq 1$, with respect to sphere drag, $4\pi\mu a^3$, may be written as

$$C_{F_x} = \frac{F_x}{4\pi\mu a^3} = \frac{4(1 + \alpha) e^3 (1 - e^2)}{3 [-2e + (1 + e^2) L]} \quad (6.4b)$$

the corresponding variation of drag coefficient with respect to eccentricity for various values of α are given in Table 1 and depicted in Figure 6.

For $\alpha = 1$, the case of axi-symmetrical paraboloidal flow, this expression of drag (6.4) reduces to the closed form [by using surface average velocity $U_e = 2a^2(1-e^2)/3 = 2b^2/3$] as

$$F_x = \frac{32\pi\mu e^3 a^3 (1-e^2)}{3[-2e + (1+e^2)L]} , \quad (6.5a)$$

which immediately reduces to $4\pi\mu a^3$, i.e., the drag on sphere having radius a in longitudinal paraboloid axisymmetric flow, as $e \rightarrow 0$ ($b = a$). This limiting value of drag on sphere may be used to write the expression of drag coefficient C_{F_x} as

$$C_{F_x} = \frac{F_x}{4\pi\mu a^3} = \frac{8e^3 (1-e^2)}{3[-2e + (1+e^2)L]} . \quad (6.5b)$$

Equation (6.5b) may be directly obtained by using (6.4b) and setting α to 1.

6.2. Transverse flow. We consider a prolate spheroid having semi-major axis a and semi-minor axis b , e as eccentricity, and c as distance of focus from centre, placed under transverse paraboloidal flow velocity $U_{\text{paraboloid}} = (\beta x^2 + z^2)$ along y -axis, and for $\beta \neq 1$, the surface average velocity U_e , over a spheroidal surface (6.1) is

$$U_e = \frac{1}{3} (1 + \beta - e^2) a^2 , \quad (6.6)$$

the value of h_y (from equation (4.8)) is

$$h_y = \frac{3b^2}{32ae^3} [2e + (3e^2 - 1)L] , \quad L = \log \frac{1+e}{1-e} . \quad (6.7)$$

For $\beta \neq 1$, the expression of drag on prolate spheroid (6.1) may be obtained from (4.9) by utilizing the values of U_e from (6.6) and h_y from (6.7) as

$$F_y = \frac{32\pi\mu e^3 a^3 (1 + \beta - e^2)}{3[2e + (3e^2 - 1)L]} , \quad (6.8a)$$

the expression of drag coefficient, for $\beta \neq 1$, with respect to sphere drag, $4\pi\mu a^3$, may be written as

$$C_{F_y} = \frac{F_y}{4\pi\mu a^3} = \frac{8e^3 (1 + \beta - e^2)}{3[2e + (3e^2 - 1)L]} , \quad (6.8b)$$

the corresponding variation of drag coefficient with respect to eccentricity for various values of β are given in Table 2 and depicted in Figure 7.

For $\beta = 1$, the case of axi-symmetrical paraboloidal flow, this expression of drag (6.8) reduces to the closed form [by using surface average velocity $U_e = a^2(2-e^2)/3 = (a^2 + b^2)/3$] as

$$F_y = \frac{32\pi\mu e^3 a^3 (2 - e^2)}{3[2e + (3e^2 - 1)L]} , \quad (6.9a)$$

which immediately reduces to $4\pi\mu a^3$, i.e. the drag on sphere having radius a in transverse paraboloid axisymmetric flow, as $e \rightarrow 0$, ($b = a$). This limiting value of drag on sphere may be used to write the expression of drag coefficient C_{F_y} as

$$C_{F_y} = \frac{F_y}{4\pi\mu a^3} = \frac{8e^3(2 - e^2)}{3[2e + (3e^2 - 1)L]} . \quad (6.9b)$$

This expression (6.9b) may be directly obtained by (6.8b), by taking $\beta = 1$.

7. OBLATE SPHEROID

7.1. Axial Flow. We consider an oblate spheroid

$$\frac{x^2}{b^2} + \frac{\rho^2}{a^2} = 1, \quad \rho^2 = y^2 + z^2, \quad a \geq b, \quad c = \sqrt{a^2 - b^2} = ea, \quad 0 \leq e \leq 1 \quad (7.1)$$

[on interchanging the roles of a and b in equation (6.1)], e as eccentricity, and c as distance of focus from centre, placed under axial paraboloidal flow velocity $U_{\text{paraboloid}} = (\alpha y^2 + z^2)$ along x -axis, and for $\alpha \neq 1$ the surface average velocity U_e , over a spheroidal surface (7.1) is

$$U_e = \frac{1}{3}(1 + \alpha)a^2, \quad (7.2)$$

the value of h_x (from equation (4.2)) is

$$h_x = \frac{3a}{8e^3} \left[e\sqrt{1 - e^2} - (1 - 2e^2)\sin^{-1}e \right], \quad L = \log \frac{1 + e}{1 - e}. \quad (7.3)$$

For $\alpha \neq 1$ the expression of drag on oblate spheroid (7.1) may be obtained from equation (4.3) by utilizing the values of U_e from (7.2) and h_x from (7.3) as

$$F_x = \frac{8\pi\mu e^3 a^3 (1 + \alpha)}{3[e\sqrt{1 - e^2} - (1 - 2e^2)\sin^{-1}e]}, \quad (7.4a)$$

the expression of drag coefficient, for $\alpha \neq 1$, with respect to sphere drag, $4\pi\mu a^3$, may be written as

$$C_{F_x} = \frac{F_x}{4\pi\mu a^3} = \frac{2e^3(1 + \alpha)}{3[e\sqrt{1 - e^2} - (1 - 2e^2)\sin^{-1}e]} \quad (7.4b)$$

the corresponding variation of drag coefficient with respect to eccentricity for various values of α are given in Table 3 and depicted in Figure 8.

For $\alpha = 1$, the case of axi-symmetrical paraboloidal flow, this expression of drag (7.4) reduces to the closed form [by using surface average velocity $U_e = 2a^2/3$] as

$$F_x = \frac{16\pi\mu e^3 a^3}{3[e\sqrt{1 - e^2} - (1 - 2e^2)\sin^{-1}e]}, \quad (7.5a)$$

which immediately reduces to $4\pi\mu a^3$, i.e. the drag on sphere having radius a in longitudinal paraboloid axisymmetric flow, as $e \rightarrow 0$ ($b = a$). This limiting value of drag on sphere may be used to write the expression of drag coefficient C_{F_x} as

$$C_{F_x} = \frac{F_x}{4\pi\mu a^3} = \frac{4e^3}{3[e\sqrt{1 - e^2} - (1 - 2e^2)\sin^{-1}e]} \quad (7.5b)$$

Expression (7.5b) may be directly obtained by (7.4b), by taking $\alpha = 1$.

7.2. Transverse flow. We consider a oblate spheroid having semi-major axis b and semi-minor axis a , e as eccentricity, and c as distance of focus from centre, placed under axial paraboloidal flow velocity $U_{\text{paraboloid}} = (\beta x^2 + z^2)$ along y -axis, and for $\beta \neq 1$, the surface average velocity U_e , over a spheroidal surface (6.1) is

$$U_e = \frac{1}{3} (1 + \beta - e^2) b^2, \quad (7.6)$$

the value of h_y (from equation (4.8)) is

$$h_y = \frac{3a}{16e^3} \left[(1 + 2e^2) \sin^{-1} e - e\sqrt{1 - e^2} \right], \quad L = \log \frac{1 + e}{1 - e}. \quad (7.7)$$

For $\beta \neq 1$, the expression of drag on oblate spheroid (7.1) may be obtained from (4.9) by utilizing the values of U_e from (7.6) and h_x from (7.7) as

$$F_y = \frac{16\pi\mu e^3 a^3 (1 + \beta - e^2)}{3 [(1 + 2e^2) \sin^{-1} e - e\sqrt{1 - e^2}]}, \quad (7.8a)$$

the expression of drag coefficient, for $\beta \neq 1$, with respect to sphere drag, $4\pi\mu a^3$, may be written as

$$C_{F_y} = \frac{F_y}{4\pi\mu a^3} = \frac{4e^3 (1 + \beta - e^2)}{3 [(1 + 2e^2) \sin^{-1} e - e\sqrt{1 - e^2}]} \quad (7.8b)$$

the corresponding variation of drag coefficient with respect to eccentricity for various values of β are given in Table 4 and depicted in Figure 9.

For $\beta = 1$, the case of axi-symmetrical paraboloidal flow, this expression of drag (7.8) reduces to the closed form [by using surface average velocity $U_e = b^2(2 - e^2)/3 = (a^2 + b^2)/3$] as

$$F_y = \frac{16\pi\mu e^3 ab^2 (2 - e^2)}{3 [(1 + 2e^2) \sin^{-1} e - e\sqrt{1 - e^2}]}, \quad (7.9a)$$

which immediately reduces to $4\pi\mu a^3$, i.e. the drag on sphere having radius a in transverse paraboloid axisymmetric flow, as $e \rightarrow 0$ ($b = a$). This limiting value of drag on sphere may be used to write the expression of drag coefficient C_{F_x} as

$$C_{F_y} = \frac{F_y}{4\pi\mu a^3} = \frac{4e^3 (2 - e^2)}{3 [(1 + 2e^2) \sin^{-1} e - e\sqrt{1 - e^2}]}. \quad (7.9b)$$

This expression (7.9b) may be directly obtained by (7.8b), by taking $\beta = 1$.

8. EGG-SHAPED BODY

8.1. Axial flow. We consider a body of revolution whose left half is semi-sphere with radius b

$$x = b \cos t, \quad r = b \sin t, \quad \pi \leq t \leq \pi/2, \quad (8.1a)$$

and right half is semi-spheroid (prolate) having semi-major axis length a and semi-minor axis length b

$$x = a \cos t, \quad r = b \sin t, \quad \pi/2 \leq t \leq 0 \quad (8.1b)$$

placed under unbounded longitudinal or axial flow with parabolic velocity profile

$$U_{\text{paraboloid}} = \alpha y^2 + z^2$$

along x -axis, and for $\alpha \neq 1$, the surface average velocity U_e over egg-shaped body (8.1) is

$$U_e = \frac{1}{6} (1 + \alpha) [b^2 + a^2 (1 - e^2)] , \quad (8.2)$$

the value of h_x (from equation (4.2)) is

$$h_x = \frac{3}{8} \left\{ \frac{2b}{3} + \frac{b^2}{4ae^3} [-2e + (1 + e^2) L] \right\} , \quad L = \log \frac{1+e}{1-e} . \quad (8.3)$$

For $\alpha \neq 1$, the expression of drag on egg-shaped body (8.1) may be obtained from (4.3) by utilizing the values of U_e from (8.2) and h_x from (8.3) as

$$F_x = \frac{8\pi\mu a\sqrt{1-e^2}}{\frac{2}{3} + \frac{\sqrt{1-e^2}}{4e^3} [-2e + (1 + e^2) L]} \left\{ \frac{1}{6} (1 + \alpha) [b^2 + a^2 (1 - e^2)] \right\} , \quad (8.4a)$$

the expression of drag coefficient, for $\alpha \neq 1$, with respect to sphere drag, $4\pi\mu a^3$, may be written as [with the help of $b^2 = a^2(1 - e^2)$]

$$C_{F_x} = \frac{F_x}{4\pi\mu a^3} = \frac{4(1 - e^2)^{3/2}}{2 + 3\frac{\sqrt{1-e^2}}{4e^3} [-2e + (1 + e^2) L]} \quad (8.4b)$$

the corresponding variation of drag coefficient with respect to eccentricity for various values of α are given in Table 5 and depicted in Figure 10.

For $\alpha = 1$, equation (8.4a) reduces to, by using the fact $b^2 = a^2(1 - e^2)$, the form

$$F_x = \frac{16}{3} \frac{\pi\mu a^3 (1 - e^2)^{3/2}}{\left\{ \frac{2}{3} + \frac{\sqrt{1-e^2}}{4e^3} [-2e + (1 + e^2) L] \right\}} , \quad (8.5a)$$

which immediately reduces to the expression of drag on sphere having radius b , i.e. $4\pi\mu b^3$, as $e \rightarrow 0$. This limiting value of drag on sphere may be used to write the expression of drag coefficient C_{F_x} as

$$C_{F_x} = \frac{F_x}{4\pi\mu a^3} = \frac{4}{3} \frac{(1 - e^2)^{3/2}}{\left\{ \frac{2}{3} + \frac{\sqrt{1-e^2}}{4e^3} [-2e + (1 + e^2) L] \right\}} \quad (8.5b)$$

This expression (8.5b) may be directly obtained by (8.4b), by taking $\alpha = 1$.

As the drag on sphere and spheroid in paraboloid flow, $U_{\text{paraboloid}} = \alpha y^2 + z^2$, has already been calculated independently in (5.1), (6.4) and (6.5), the expression of drag on egg-shaped body in paraboloid flow, for $\alpha \neq 1$, may be expressed in the combination of both as

$$F_x = \pi\mu (1 + \alpha) b^3 + \frac{\pi\mu (1 + \alpha) [8e^3 a^3 (1 - e^2)]}{3 [-2e + (1 + e^2) L]} , \quad (8.6)$$

for $\alpha = 1$, this expression (8.6) reduces to the form, with the aid of $b^2 = a^2(1 - e^2)$,

$$F_x = 2\pi\mu \frac{b^3 [-2e + (1 + e^2)L + 8e^3a^3(1 - e^2)]}{-2e + (1 + e^2)L}, \quad (8.7)$$

which immediately reduces to the expression of drag on sphere having radius b placed in axial axis-symmetric paraboloidal flow, i.e. $\pi\mu b^3$, as $e \rightarrow 0$ ($a = b$).

8.2. Transverse flow. We shall consider a body whose left half is semi-sphere with radius b

$$x = b \cos t, \quad r = b \sin t, \quad \pi \leq t \leq \pi/2, \quad (8.8a)$$

and right half is semi-spheroid(prolate) having semi-major axis length a and semi-minor axis length b

$$x = a \cos t, \quad r = b \sin t, \quad \pi/2 \leq t \leq 0, \quad (8.8b)$$

placed under unbounded transverse flow with parabolic velocity profile

$$U_{\text{paraboloid}} = \beta x^2 + z^2$$

along y -axis, and for $\beta \neq 1$, the surface average velocity U_e over egg-shaped body (8.8) is

$$U_e = \frac{\frac{1}{3}(1 + \beta)b^2 + \frac{1}{3}(1 + \beta - e^2)b^2}{2} = \frac{b^2}{6} [2(1 + \beta) - e^2] \quad (8.9)$$

from where if $\beta = 1$ it follows

$$U_e = \frac{b^2}{6} (4 - e^2) \rightarrow \frac{2}{3}b^2$$

which is the average surface velocity on a sphere with radius $R = b$ as $e \rightarrow 0$ ($b = a$).

The value of h_y from equation (4.8)) is

$$h_y = \frac{3}{16} \left[\frac{4}{3} + \frac{\sqrt{1 - e^2}}{4e^3} \{2e + (3e^2 - 1)L\} \right], \quad L = \log \frac{1 + e}{1 - e}. \quad (8.10)$$

For $\beta \neq 1$, the expression of drag on egg-shaped body (8.8) may be obtained from (4.9) by utilizing the values of U_e from (8.9) and h_y from (8.10) as [with the aid of $b^2 = a^2(1 - e^2)$]

$$\begin{aligned} F_y &= \frac{16\pi\mu a \sqrt{1 - e^2}}{\left[\frac{4}{3} + \frac{\sqrt{1 - e^2}}{4e^3} \{2e + (3e^2 - 1)L\} \right]} \left[\frac{b^2}{6} \{2(1 + \beta) - e^2\} \right] = \\ &= \frac{8\pi\mu a^3 (1 - e^2)^{3/2} [2(1 + \beta) - e^2]}{3 \left[\frac{4}{3} + \frac{\sqrt{1 - e^2}}{4e^3} \{2e + (3e^2 - 1)L\} \right]} \quad (8.11a) \end{aligned}$$

the expression of drag coefficient, for $\beta \neq 1$, with respect to sphere drag, $4\pi\mu a^3$, may be written as

$$C_{F_y} = \frac{F_y}{4\pi\mu a^3} = \frac{2(1 - e^2)^{3/2} [2(1 + \beta) - e^2]}{3 \left[\frac{4}{3} + \frac{\sqrt{1 - e^2}}{4e^3} \{2e + (3e^2 - 1)L\} \right]}, \quad (8.11b)$$

the corresponding variation of drag coefficient with respect to eccentricity for various values of α are given in Table 6 and depicted in Figure 11.

If $\beta = 1$, equation (8.11a) reduces to

$$F_y = \frac{8\pi\mu a^3 (1 - e^2)^{3/2} [4 - e^2]}{3 \left[\frac{4}{3} + \frac{\sqrt{1-e^2}}{4e^3} \{2e + (3e^2 - 1)L\} \right]}, \quad (8.12a)$$

which immediately reduces to the expression of drag on sphere having radius b , i.e. $4\pi\mu b^3$, as $e \rightarrow 0$ ($b = a$). This limiting value of drag on sphere may be used to write the expression of drag coefficient C_{F_y} as

$$C_{F_y} = \frac{F_y}{4\pi\mu a^3} = \frac{2 (1 - e^2)^{3/2} [4 - e^2]}{3 \left[\frac{4}{3} + \frac{\sqrt{1-e^2}}{4e^3} \{2e + (3e^2 - 1)L\} \right]}. \quad (8.12b)$$

Equation (8.12b) can also be obtained directly from (8.11b) by setting β to 1.

As the drag on sphere and spheroid in transverse paraboloid flow having velocity, $U_{\text{paraboloid}} = \beta x^2 + z^2$, has already been calculated independently in (5.2), (6.8) and (6.9), the expression of drag on egg-shaped body in transverse paraboloid flow may be expressed in the combination of both as

$$F_y = \pi\mu (1 + \beta) b^3 + \frac{16\pi\mu e^3 a^3 (1 + \beta - e^2)}{3 [2e + (3e^2 - 1)L]}. \quad (8.13)$$

If $\beta = 1$ equation (8.13) takes the form

$$F_y = \frac{2\pi\mu [3b^3 \{2e + (3e^2 - 1)L\} + 8e^3 a^3 (2 - e^2)]}{3 [2e + (3e^2 - 1)L]}, \quad (8.14)$$

which immediately reduces to the drag expression of drag on sphere having radius a placed in transverse axis-symmetric paraboloidal flow, i.e. $4\pi\mu a^3$, as $e \rightarrow 0$ ($b = a$).

9. STAGNATION LIKE QUADRATIC FLOW PAST AXIALLY SYMMETRIC BODIES

9.1. Axial stagnation like paraboloid flow (or unbounded longitudinal stagnation paraboloidal flow). We consider an axis-symmetric body placed in a longitudinal stagnation-like quadratic flow (Figure 5) with velocity

$$\mathbf{u} = x^2 \mathbf{e}_x - 2xy \mathbf{e}_y \quad (9.1)$$

$$u = |\mathbf{u}| = (x^4 + 4x^2 y^2)^{1/2} \quad (9.2)$$

along axis of symmetry which is x -axis, which obviously satisfies the Stokes equations (2.1) if the pressure associated with it is $2\mu x$. The stagnation plane is the centre-plane $x = 0$. In the half-space $x < 0$ the flow is towards the stagnation plane while in the half-space $x > 0$ it is away from this plane. This type of quadratic flow is important since it can serve as a component in the general study of the motion of a spheroidal particle placed in a paraboloidal flow whose direction does not coincide with any one of the principal axes of the spheroid.

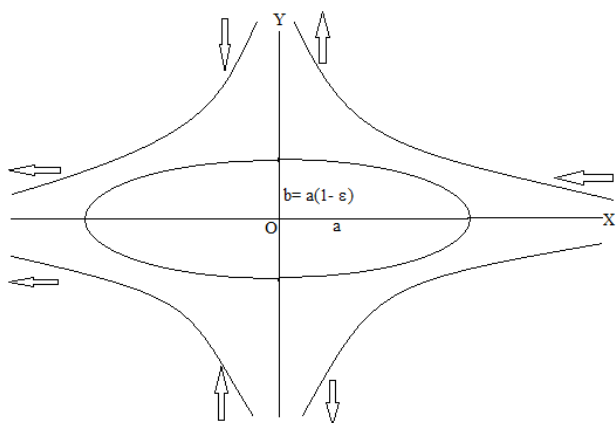


Figure 4. A longitudinal or axial stagnation like parabolic flow past axisymmetric body

9.2. Transverse stagnation like paraboloid flow. We consider an axi-symmetric body placed in a longitudinal stagnation-like quadratic flow (Figure 05) with velocity

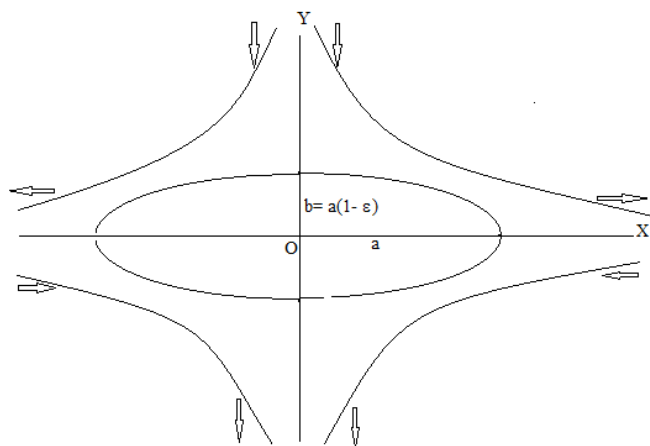


Figure 5. A longitudinal or axial stagnation like parabolic flow past axisymmetric body

10. SPHERE

10.1. Axial Flow. We consider a sphere with radius b and placed under axial stagnation like paraboloidal flow having velocity $U = |\mathbf{U}| = (x^4 + 4x^2y^2)^{1/2}$, by considering the surface average velocity $U_e = b^2/3$, over a spherical surface $R = b$, the value of $h_x = b/2$ (from equation (4.2)), the expression of drag on sphere comes out to be (with the use of equation (4.3))

$$F_x = \frac{3\pi\mu b^2}{h_x} U_e = \frac{3\pi\mu b^2}{\frac{a}{2}} \left(\frac{1}{3} b^2 \right) = 2\pi\mu b^3, \quad (10.1)$$

which matches with that obtained by Chwang [3, part 3, 1975, p. 28, eq. 42] treated with singularity method.

10.2. Transverse flow. We consider a sphere having radius b placed under transverse stagnation like paraboloidal flow velocity $U = |\mathbf{U}| = (y^4 + 4x^2y^2)^{1/2}$, by considering the surface average velocity $U_e = (1/3)b^2$, over a spherical surface $R = b$, the value of $h_y = b/2$ (from equation (4.8)), the expression of drag on sphere in transverse stagnation like paraboloidal flow comes out to be (with the use of equation (4.9))

$$F_y = \frac{3\pi\mu b^2}{h_y} U_e = \frac{3\pi\mu b^2}{\frac{b}{2}} \left(\frac{1}{3} b^2 \right) = 2\pi\mu b^3, \quad (10.2)$$

which matches with that obtained by Chwang [3, part 3, 1975, p. 28, eq. 42] treated with singularity method and is exactly the same as obtained in axial situation (10.1). The reason behind it is the fore and aft symmetry of the spherical body.

11. PROLATE SPHEROID

11.1. Axial Flow. details – which is subjected to an axial stagnation like a paraboloidal flow with a velocity $U = |\mathbf{U}| = (x^4 + 4x^2y^2)^{1/2}$ along x -axis. The surface average velocity U_e , over a spheroidal surface is

$$U_e = \frac{1}{3} a^2 \quad (11.1)$$

The value of h_x can easily be obtained from equation (4.2) and coincides with equation (6.3).

The expression for drag on a prolate spheroid (6.1) in axial stagnation like a paraboloid flow may be obtained from (4.3) by utilizing the values of U_e from (11.1) and h_x from (6.3) as

$$F_x = \frac{16\pi\mu e^3 a^3}{3[-2e + (1 + e^2)L]}, \quad (11.2a)$$

The above expression takes the form $2\pi\mu a^3$, i.e., that of the drag on a sphere with radius a and placed in axial stagnation type parabolic flow with velocity $U = |\mathbf{U}| =$

$(x^4 + 4x^2y^2)^{1/2}$, as $e \rightarrow 0$. The expression of drag coefficient, with respect to sphere drag $2\pi\mu a^3$, may be written as

$$C_{F_x} = \frac{F_x}{2\pi\mu a^3} = \frac{8e^3}{3[-2e + (1 + e^2)L]} \quad (11.2b)$$

the corresponding variation of drag coefficient with respect to eccentricity are given in Table 7 and depicted in Figure 12.

11.2. Transverse flow. Assume that the prolate spheroid is placed under transverse stagnation like a paraboloid flow having velocity $U = |\mathbf{U}| = (y^4 + 4x^2y^2)^{1/2}$ along y -axis. The surface average velocity U_e over a spheroidal surface is

$$U_e = \frac{1}{3}b^2 = \frac{1}{3}a^2(1 - e^2). \quad (11.3)$$

The value of h_y (obtainable from equation (4.8)) coincides with the right side of equation (6.7).

The expression of drag on prolate spheroid (6.1) in transverse stagnation like paraboloid flow can be obtained from (4.9) by utilizing the values of U_e from (11.3) and h_y from (6.7) as

$$F_y = \frac{32\pi\mu e^3 a}{2e + (3e^2 - 1)L} \frac{a^2(1 - e^2)}{3} = \frac{32\pi\mu e^3 a^3(1 - e^2)}{3[2e + (3e^2 - 1)L]}, \quad (11.4a)$$

which immediately reduces to $2\pi\mu a^3$, the drag on sphere having a radius a placed in transverse stagnation type parabolic flow with velocity $U = |\mathbf{U}| = (y^4 + 4x^2y^2)^{1/2}$, as $e \rightarrow 0$. The expression of drag coefficient, with respect to sphere drag, $2\pi\mu a^3$ may be written as

$$C_{F_y} = \frac{F_y}{2\pi\mu a^3} = \frac{16e^3(1 - e^2)}{3[2e + (3e^2 - 1)L]} \quad (11.4b)$$

the corresponding variation of drag coefficient with respect to eccentricity are given in Table 7 and is depicted in Figure 12.

12. OBLATE SPHEROID

12.1. Axial Flow. We consider an oblate spheroid – see equation (7.1). If we interchange the roles of a and b in equation (6.1) – e is eccentricity and c is the distance of focus from centre – assuming axial paraboloidal flow velocity $U = |\mathbf{U}| = (x^4 + 4x^2y^2)^{1/2}$ along x -axis, the surface average velocity U_e , over the spheroidal surface (7.1) is

$$U_e = \frac{1}{3}b^2. \quad (12.1)$$

The value of h_x (obtainable from equation (4.2)) coincides with the right side of equation (7.3).

The expression of drag on oblate spheroid (7.1) in axial stagnation like paraboloid flow can be obtained from (4.3) by utilizing the values of U_e from (11.1) and h_x from

(7.3) as

$$F_x = \frac{8\pi\mu a e^3}{e\sqrt{1-e^2} - (1-2e^2)\sin^{-1}e} \frac{b^2}{3} = \frac{8\pi\mu a^3 e^3 (1-e^2)}{3 [e\sqrt{1-e^2} - (1-2e^2)\sin^{-1}e]}. \quad (12.2a)$$

Equation of drag (12.2a) reduces to the closed form, $2\pi\mu b^3$, the drag on sphere having radius b placed in axial stagnation type parabolic flow with velocity $U = |\mathbf{U}| = (x^4 + 4x^2y^2)^{1/2}$ as $e \rightarrow 0$ ($b = a$). The expression of drag coefficient, with respect to sphere drag, $2\pi\mu a^3$, may be written as

$$C_{F_x} = \frac{F_x}{2\pi\mu a^3} = \frac{4e^3 (1-e^2)}{3 [e\sqrt{1-e^2} - (1-2e^2)\sin^{-1}e]} \quad (12.2b)$$

the corresponding variation of drag coefficient with respect to eccentricity are given in Table 8 and depicted in Figure 13.

12.2. Transverse flow. We consider an oblate spheroid (7.1), e as eccentricity, and a as distance of focus from centre, placed under transverse stagnation like paraboloid flow having velocity $U = U|\mathbf{U}| = (y^4 + 4x^2y^2)^{1/2}$ along y -axis. The surface average velocity U_e , over a spheroidal surface (7.1), is

$$U_e = \frac{1}{3} a^2, \quad (12.3)$$

the value of h_y (obtainable from equation (4.2)) coincides with the right side of equation (7.7).

The expression of drag on oblate spheroid (7.1) in transverse stagnation like paraboloid flow may be obtained from (4.9) by utilizing the values of U_e from (12.3) and h_y from (7.7) as

$$F_y = \frac{16\pi\mu e^3 a}{(1+2e^2)\sin^{-1}e - e\sqrt{1-e^2}} \frac{a^2}{3} = \frac{16\pi\mu e^3 a^3}{3 [(1+2e^2)\sin^{-1}e - e\sqrt{1-e^2}]}, \quad (12.4a)$$

which immediately reduces to $2\pi\mu b^3$, the drag on sphere having radius b placed in transverse stagnation type parabolic flow with velocity $U = |\mathbf{U}| = (y^4 + 4x^2y^2)^{1/2}$, as $e \rightarrow 0$ ($b = a$). The expression of drag coefficient, with respect to sphere drag, $\pi\mu a^3$, may be written as

$$C_{F_y} = \frac{F_y}{\pi\mu a^3} = \frac{8e^3}{3 [(1+2e^2)\sin^{-1}e - e\sqrt{1-e^2}]} \quad (12.4b)$$

the corresponding variation of drag coefficient with respect to eccentricity are given in Table 8 and depicted in Figure 13.

13. EGG-SHAPED BODY

13.1. Axial flow. We consider again the body described by equations (8.1) and placed under unbounded longitudinal or axial stagnation flow with parabolic velocity

profile $U = |\mathbf{U}| = (x^4 + 4x^2y^2)^{1/2}$ along x -axis. The surface average velocity U_e over egg-shaped body (8.1) is

$$U_e = \frac{1}{6} [b^2 + a^2 (1 - e^2)] \quad (13.1)$$

The value of h_x (obtainable from equation (4.2)) coincides with the right side of equation (8.2).

The expression of drag on egg-shaped body (8.1) may be obtained from (4.3) by utilizing the values of U_e from (13.1) and h_x from (8.2) as

$$F_x = \frac{8\pi\mu a\sqrt{1-e^2}}{\frac{2}{3} + \frac{\sqrt{1-e^2}}{4e^2} \{-2e + (1+e^2)L\}} \frac{1}{6} [b^2 + a^2 (1 - e^2)] . \quad (13.2)$$

Equation (??) reduces to, by using the fact $b^2 = a^2(1 - e^2)$, the form

$$F_x = \frac{16}{3} \frac{\pi\mu a^3 (1 - e^2)^{3/2}}{\frac{2}{3} + \frac{\sqrt{1-e^2}}{4e^2} [-2e + (1+e^2)L]} , \quad (13.3a)$$

The expression of drag coefficient, with respect to sphere drag, $2\pi\mu a^3$, may be written as

$$C_{F_x} = \frac{F_x}{2\pi\mu a^3} = \frac{8(1 - e^2)^{3/2}}{3 \left\{ \frac{2}{3} + \frac{\sqrt{1-e^2}}{4e^2} [-2e + (1+e^2)L] \right\}} \quad (13.3b)$$

the corresponding variation of drag coefficient with respect to eccentricity are given in Table 9 and depicted in Figure 14.

Equation (13.3a) immediately reduces to the expression of drag on sphere having radius b placed in axial stagnation like paraboloid flow, i.e., $2\pi\mu b^3$, as $e \rightarrow 0$ ($b = a$). As the drag on sphere and spheroid in axial stagnation type paraboloid flow, $U = |\mathbf{U}| = (x^4 + 4x^2y^2)^{1/2}$, has already been calculated independently in (10.1) and (11.2, 11.4)), the expression of drag on egg-shaped body in axial stagnation like paraboloid flow may be expressed in the combination of both as

$$F_x = \pi\mu b^3 + \frac{8\pi\mu e^3 a^3}{3[-2e + (1+e^2)L]} , \quad (13.4)$$

which immediately reduces to the drag expression of drag on sphere having radius 'b' placed in axial stagnation like paraboloidal flow i.e. $2\pi\mu b^3$, as $e \rightarrow 0$, ($b = a$).

13.2. Transverse flow. We consider again the body described by equations (8.8) and placed under unbounded longitudinal or axial stagnation flow with under unbounded transverse stagnation like flow with parabolic velocity profile $U = |\mathbf{U}| = (y^4 + 4x^2y^2)^{1/2}$ along y -axis. The surface average velocity U_e over egg-shaped body (8.8) is

$$U_e = \frac{b^2}{6} (2 - e^2) = \frac{1}{3} b^2 , \quad (13.5)$$

i.e. the average surface velocity on sphere placed in stagnation like flow, as $e \rightarrow 0$.

The value of h_x (obtainable from equation (4.2)) coincides with the right side of equation (8.10).

The expression of drag on egg-shaped body (8.8) may be obtained from (4.9) by utilizing the values of U_e from (13.5) and h_y from (8.10) as

$$F_y = \frac{16\pi\mu a\sqrt{1-e^2}}{\frac{4}{3} + \frac{\sqrt{1-e^2}}{4e^3} [2e + (3e^2 - 1)L]} \frac{b^2}{6} (2 - e^2) = \frac{8\pi\mu a^3 (1 - e^2)^{3/2} (2 - e^2)}{3 \left\{ \frac{4}{3} + \frac{\sqrt{1-e^2}}{4e^3} [2e + (3e^2 - 1)L] \right\}}, \quad (13.6a)$$

which immediately reduces to the expression of drag on sphere having radius b placed in transverse stagnation like flow of paraboloidal velocity, $U = |\mathbf{U}| = (y^4 + 4x^2y^2)^{1/2}$, i.e. $2\pi\mu b^3$, as $e \rightarrow 0$.

The expression of drag coefficient, with respect to sphere drag, $2\pi\mu a^3$, may be written as

$$C_{F_y} = \frac{F_y}{2\pi\mu a^3} = \frac{4(1 - e^2)^{3/2} (2 - e^2)}{3 \left\{ \frac{4}{3} + \frac{\sqrt{1-e^2}}{4e^3} [2e + (3e^2 - 1)L] \right\}}, \quad (13.6b)$$

the corresponding variation of drag coefficient with respect to eccentricity are given in Table 9 and depicted in Figure 14.

As the drag on sphere and spheroid in transverse stagnation like flow of paraboloidal velocity, $U = |\mathbf{U}| = (y^4 + 4x^2y^2)^{1/2}$, has already been calculated independently in (10.2) and (11.4a), the expression of drag on egg-shaped body in transverse stagnation like paraboloid flow may be expressed in the combination of both as

$$F_y = \pi\mu b^3 + \frac{16\pi\mu e^3 a^3 (1 - e^2)}{3 [2e + (3e^2 - 1)L]}, \quad (13.7)$$

which immediately reduces to the drag on sphere having radius b placed in transverse stagnation like paraboloidal flow, $U = |\mathbf{U}| = (y^4 + 4x^2y^2)^{1/2}$, i.e. $2\pi\mu b^3$, as $e \rightarrow 0$, ($b = a$).

14. NUMERICAL DISCUSSION

The numerical values of drag coefficient for axi-symmetric bodies like sphere, spheroid and egg-shaped body placed in axial and transverse quadratic (parabolic) flow have been calculated with respect to eccentricity e and presented in Tables 1-6 respectively for various values of flow constants α and β (varies from 1 to 5). In all these calculations, the flow constants α and β are equal to one which represents the case of axi-symmetric quadratic Stokes flow. In Table 1, the values of C_{F_x} (drag coefficient for prolate spheroid placed in axial parabolic flow, Figure 2 decreases from corresponding drag values of sphere (1.0, 1.5, 2.0, 2.5, 3.0 for $\alpha = 1, 2, 3, 4, 5$) to 0 with respect to increasing values of eccentricity e (from 0 to 1). In Table 1, it is interesting to note that the maximum difference between the two values of C_{F_x} for two successive values of flow constant α never exceeded by 0.5 which in every case decreases further to 0. For $e = 1$, the case of slender or needle shaped body, C_{F_x} comes out to be 0 which is justified. In comparison to axi-symmetric flow (for $\alpha = 1$), the non-symmetric flow situations (for $\alpha = 2, 3, 4, 5, \dots$) create maximum difference

by values 0.5, 1.0, 1.5, 2.0 and so on. All the respective values of C_{Fx} have been calculated from equation (6.4b)). All these variations are depicted in Figure 6.

In Table 2, the values of C_{Fy} (drag coefficient for prolate spheroid placed in transverse parabolic flow, Figure 3) decreases from corresponding drag values of sphere (1.0, 1.5, 2.0, 2.5, 3.0 for $\beta = 1, 2, 3, 4, 5$) to 0 with respect to increasing values of eccentricity e (from 0 to 1). In Table 2, it is interesting to note that the maximum difference between the two values of C_{Fy} for two successive values of flow constant β never exceeded by 0.5 which in every case decreases further to 0. For $e = 1$, the case of slender or needle shaped body, C_{Fy} comes out to be 0 which is justified. In comparison to axi-symmetric flow (for $\beta = 1$), the non-symmetric flow situations (for $\beta = 2, 3, 4, 5, \dots$) create maximum difference by values 0.5, 1.0, 1.5, 2.0 and so on. All the respective values of C_{Fy} have been calculated from equation (6.8b). On comparing the values of drag coefficient in Table 1 and Table 2, it may be observed that the transverse values are always greater than axial values at every stage. This fact is also justified as the broader part of the prolate body faces the transverse flow. All these variations are depicted in Figure 7.

In Table 3, the values of C_{Fx} (drag coefficient for oblate spheroid placed in axial parabolic flow, Figure 2) decreases from corresponding drag values of sphere (1.0, 1.5, 2.0, 2.5, 3.0 for $\alpha = 1, 2, 3, 4, 5$) with respect to increasing values of eccentricity e (from 0 to 1). In Table 3, it is interesting to note that the maximum difference between the two values of C_{Fx} for two successive values of flow constant α never exceeded by 0.5 which in every case decreases further. For $e = 1$, the case of flat circular disk, C_{Fx} comes out to be non-zero which is justified again. In comparison to axi-symmetric flow (for $\alpha = 1$), the non-symmetric flow situations (for $\alpha = 2, 3, 4, 5, \dots$) create maximum difference by values 0.5, 1.0, 1.5, 2.0 and so on. All the respective values of C_{Fx} have been calculated from equation (7.4b). All these variations are depicted in Figure 8.

In Table 4, the values of C_{Fy} (drag coefficient for oblate spheroid placed in transverse parabolic flow, Figure 2) decreases from corresponding drag values of sphere (1.0, 1.5, 2.0, 2.5, 3.0 for $\beta = 1, 2, 3, 4, 5$) with respect to increasing values of eccentricity e (from 0 to 1). In Table 4, it is interesting to note that the maximum difference between the two values of C_{Fy} for two successive values of flow constant α never exceeded by 0.5 which in every case decreases further. For $e = 1$, the case of flat circular disk, C_{Fy} comes out to be non-zero which is justified again. In comparison to axi-symmetric flow (for $\alpha = 1$), the non-symmetric flow situations (for $\alpha = 2, 3, 4, 5, \dots$) create maximum difference by values 0.5, 1.0, 1.5, 2.0 and so on. All the respective values of C_{Fx} have been calculated from equation (7.4b). On comparing the numerical values of drag coefficients for flat circular disk in axial and transverse flow cases, it may be observed that drag in axial flow is greater than drag in transverse flow. It is also justified the fact that broader part of oblate spheroid faces the axial paraboloid flow whereas the thinner portion faces the transverse paraboloid flow. All these variations are depicted in Figure 9. In Table 5 and 6, the numerical values of drag on egg-shaped body consisting of semi-spherical and semi-spheroidal part are presented.

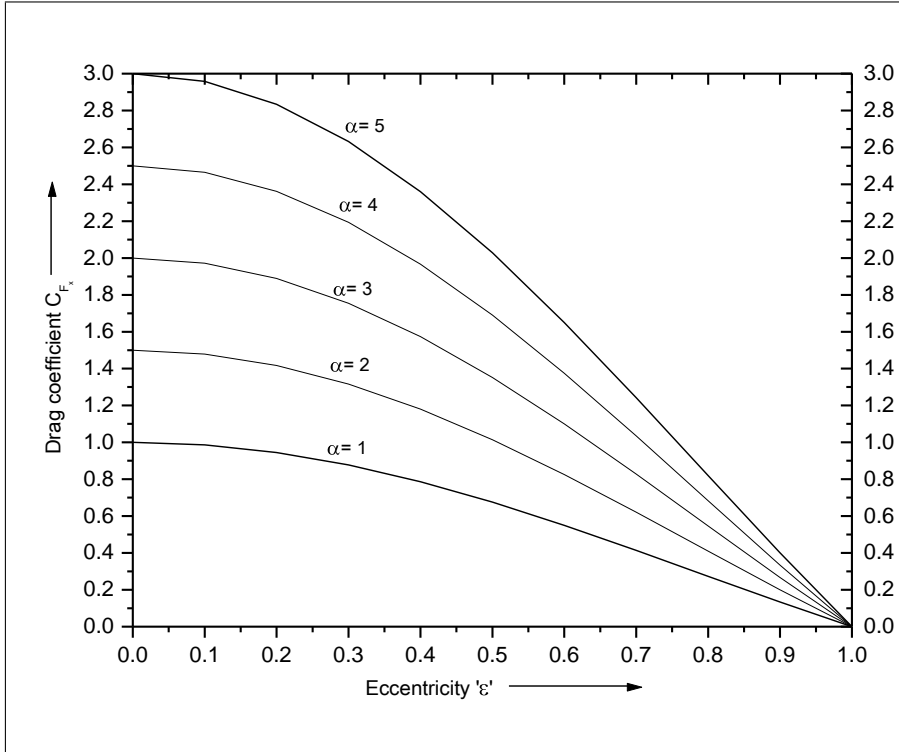


Figure 6. Variation of drag coefficient with respect to the eccentricity e for various values of the constant α

Table 1. Numerical values of drag coefficient(axial parabolic flow) for prolate spheroid with respect to eccentricity e for various values of constant α (depicted in Figure 6) [Calculated from equation (6.4b)]

	$\alpha = 1$	$\alpha = 2$	$\alpha = 3$	$\alpha = 4$	$\alpha = 5$
e	C_{Fx}	C_{Fx}	C_{Fx}	C_{Fx}	C_{Fx}
0.0	1.000000	1.50000	2.0000	2.50000	3.00000
0.1	0.986041	1.47906	1.9721	2.46513	2.95812
0.2	0.944659	1.41699	1.8893	2.36165	2.83398
0.3	0.877349	1.31602	1.7547	2.19337	2.63205
0.4	0.786635	1.17995	1.5732	1.96659	2.35993
0.5	0.676056	1.01408	1.3521	1.69014	2.02817
0.6	0.550093	0.82514	1.1002	1.37523	1.65028
0.7	0.413956	0.62093	0.8279	1.03489	1.24187
0.8	0.273257	0.40989	0.5465	0.68314	0.81977
0.9	0.133576	0.20036	0.2672	0.33394	0.40073
1.0	0	0	0	0	0

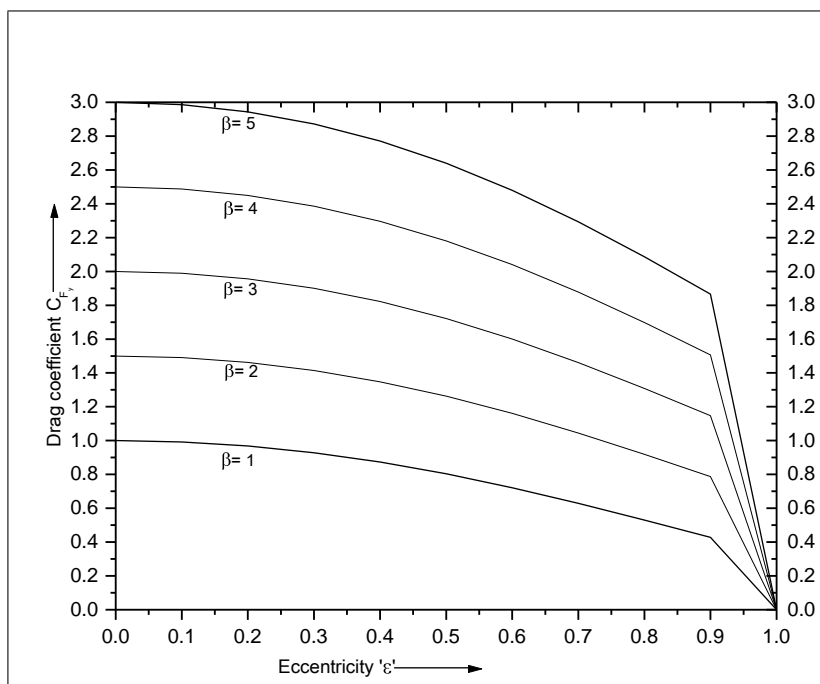


Figure 7. Variation of drag coefficient with respect to the eccentricity e for various values of the constant β

Table 2. Numerical values of drag coefficient (transverse parabolic flow) for prolate spheroid with respect to eccentricity e for various values of constant β (depicted in Figure 7) [Calculated from equation (6.8b)]

	$\beta = 1$	$\beta = 2$	$\beta = 3$	$\beta = 4$	$\beta = 5$
e	C_{Fy}	C_{Fy}	C_{Fy}	C_{Fy}	C_{Fy}
0.0	1.00000	1.50000	2.00000	2.50000	3.00000
0.1	0.992002	1.49049	1.98899	2.48748	2.98597
0.2	0.968035	1.46193	1.95583	2.44972	2.94362
0.3	0.928246	1.41424	1.90023	2.38622	2.87222
0.4	0.873064	1.34756	1.82205	2.29654	2.77103
0.5	0.803443	1.26255	1.72166	2.18077	2.63989
0.6	0.721095	1.16079	1.60048	2.04017	2.47986
0.7	0.628631	1.04494	1.46125	1.87757	2.29388
0.8	0.529529	0.918889	1.30825	1.69761	2.08697
0.9	0.427866	0.787417	1.14697	1.50652	1.86607
1.0	0	0	0	0	0

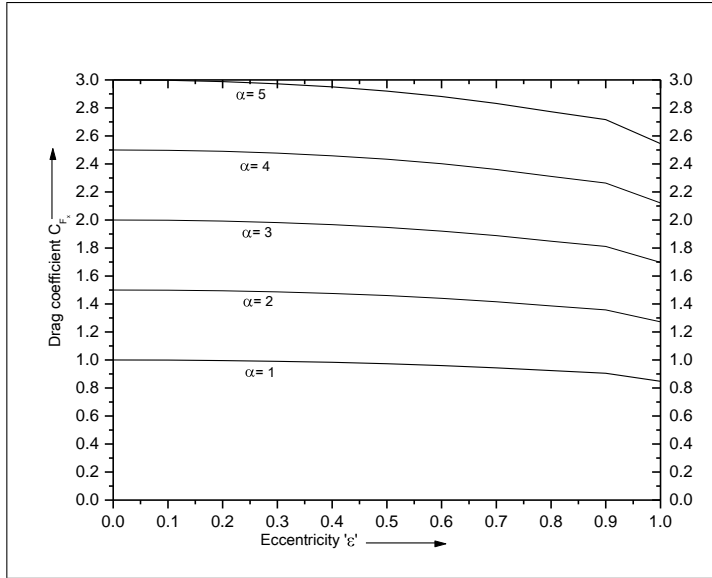


Figure 8. Variation of drag coefficient with respect to the eccentricity e for various flow constant α

Table 3. Variation of drag coefficient (axial parabolic flow) for oblate spheroid with respect to eccentricity e for various values of constant α (depicted in Figure 8) [Calculated from equation (7.4b)]

	$\alpha = 1$	$\alpha = 2$	$\alpha = 3$	$\alpha = 4$	$\alpha = 5$
e	C_{Fx}	C_{Fx}	C_{Fx}	C_{Fx}	C_{Fx}
0.0	1.00000	1.50000	2.0000	2.50000	3.00000
0.1	0.998998	1.49856	1.9985	2.49749	2.99699
0.2	0.995964	1.49395	1.9919	2.48991	2.98789
0.3	0.990812	1.48622	1.9816	2.47703	2.97244
0.4	0.983382	1.47507	1.9668	2.45846	2.95015
0.5	0.973406	1.46011	1.9468	2.43351	2.92022
0.6	0.960476	1.44071	1.9210	2.40119	2.88143
0.7	0.944111	1.41617	1.8882	2.36028	2.83233
0.8	0.924349	1.38652	1.8487	2.31087	2.77305
0.9	0.905344	1.35802	1.8107	2.26336	2.71603
1.0	0.848484	1.27272	1.6968	2.12125	2.54526

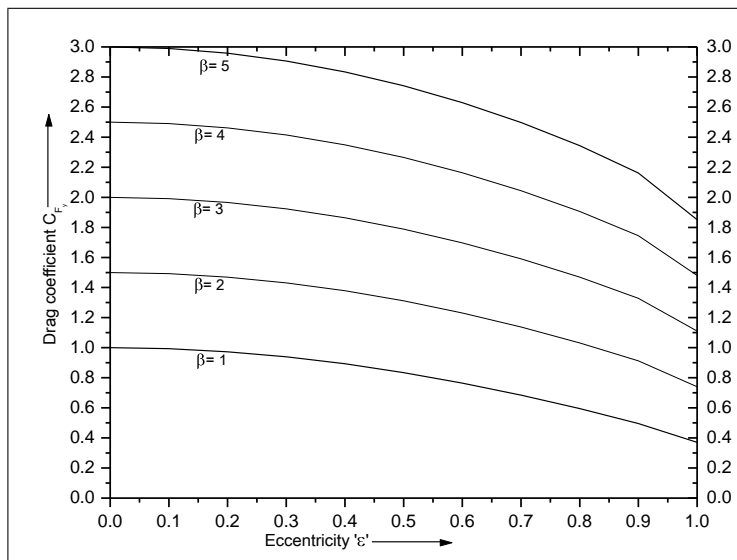


Figure 9. Variation of drag coefficient C_{Fx} with respect to the eccentricity e for various flow constant β

Table 4. Numerical values of drag coefficient(transverse parabolic flow) for oblate spheroid with respect to eccentricity e for various values of constant β (depicted in Figure 9)[Calculated from equation (7.8b)]

	$\beta = 1$	$\beta = 2$	$\beta = 3$	$\beta = 4$	$\beta = 5$
e	C_{Fx}	C_{Fx}	C_{Fx}	C_{Fx}	C_{Fx}
0.0	1.000000	1.50000	2.00000	2.50000	3.00000
0.1	0.993195	1.49229	1.99138	2.49047	2.98957
0.2	0.972874	1.46924	1.96564	2.46197	2.95833
0.3	0.939316	1.43114	1.92289	2.41468	2.90647
0.4	0.892978	1.37829	1.86361	2.34892	2.83423
0.5	0.834493	1.31135	1.78826	2.26505	2.74196
0.6	0.764651	1.23095	1.69715	2.16344	2.62965
0.7	0.684369	1.13759	1.59082	2.04404	2.49727
0.8	0.594571	1.03176	1.46894	1.90612	2.34331
0.9	0.495601	0.91207	1.32854	1.74501	2.16149
1.0	0.370187	0.74037	1.11056	1.48074	1.85093

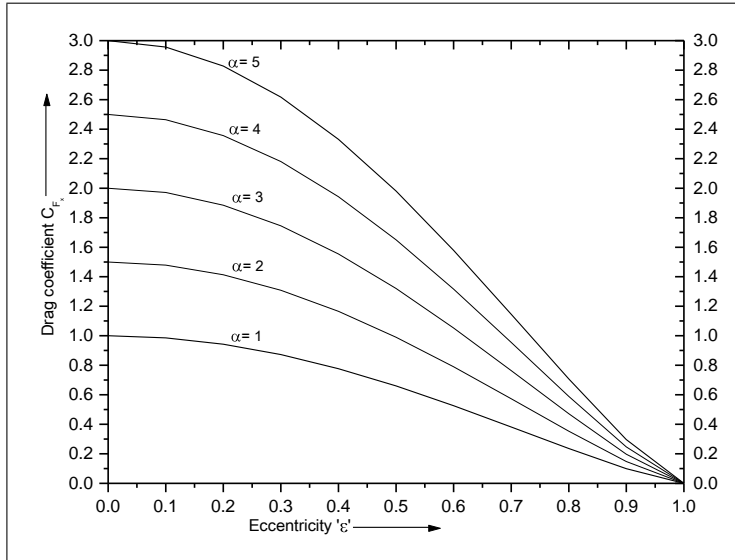


Figure 10. Variation of drag coefficient with respect to the eccentricity e for various values of the constant α

Table 5. Numerical values of drag coefficient (axial parabolic flow) for egg-shaped body with respect to eccentricity e for various values of constant α (depicted in Figure 10)[Calculated from equation (8.4b)]

	$\alpha = 1$	$\alpha = 2$	$\alpha = 3$	$\alpha = 4$	$\alpha = 5$
e	C_{Fx}	C_{Fx}	C_{Fx}	C_{Fx}	C_{Fx}
0.0	1.000000	1.50000	2.00000	2.50000	3.00000
0.1	0.985534	1.47834	1.97107	2.46383	2.9568
0.2	0.942545	1.41382	1.88509	2.35636	2.82763
0.3	0.872297	1.30845	1.74459	2.18074	2.61689
0.4	0.777018	1.16533	1.55404	1.94255	2.33105
0.5	0.660082	0.99012	1.32016	1.65024	1.98025
0.6	0.526246	0.78936	1.05249	1.31561	1.57874
0.7	0.381933	0.57295	0.76386	0.95483	1.14586
0.8	0.235596	0.35339	0.47119	0.58899	0.70679
0.9	0.098860	0.14829	0.19772	0.24715	0.29658
1.0	0	0	0	0	0

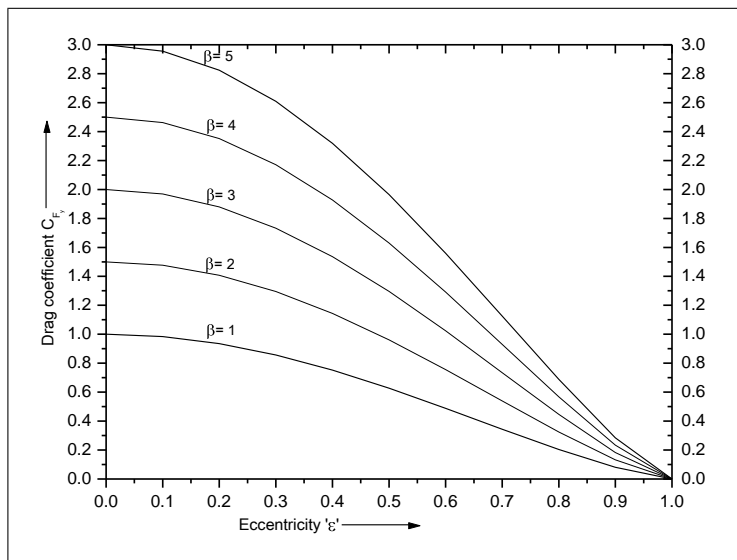


Figure 11. Variation of drag coefficient with respect to the eccentricity e for various values of the constant β

Table 6. Numerical values of drag coefficient (transverse parabolic flow) for egg-shaped body with respect to eccentricity e for various values of constant β (depicted in Figure 11) [Calculated from equation (8.11b)]

	$\beta = 1$	$\beta = 2$	$\beta = 3$	$\beta = 4$	$\beta = 5$
e	C_{Fx}	C_{Fx}	C_{Fx}	C_{Fx}	C_{Fx}
0.0	1.000000	1.50000	2.00000	2.50000	3.00000
0.1	0.983564	1.47658	1.96959	2.46261	2.95562
0.2	0.935017	1.40725	1.87948	2.35171	2.82394
0.3	0.856634	1.29481	1.73299	2.17116	2.60934
0.4	0.752191	1.14396	1.53572	1.92749	2.31926
0.5	0.626971	0.96136	1.29574	1.63013	1.96451
0.6	0.487834	0.75587	1.02391	1.29195	1.55998
0.7	0.343286	0.53888	0.73448	0.93008	1.12568
0.8	0.203567	0.32474	0.44591	0.56708	0.68825
0.9	0.081137	0.13201	0.18288	0.23375	0.28462
1.0	0	0	0	0	0

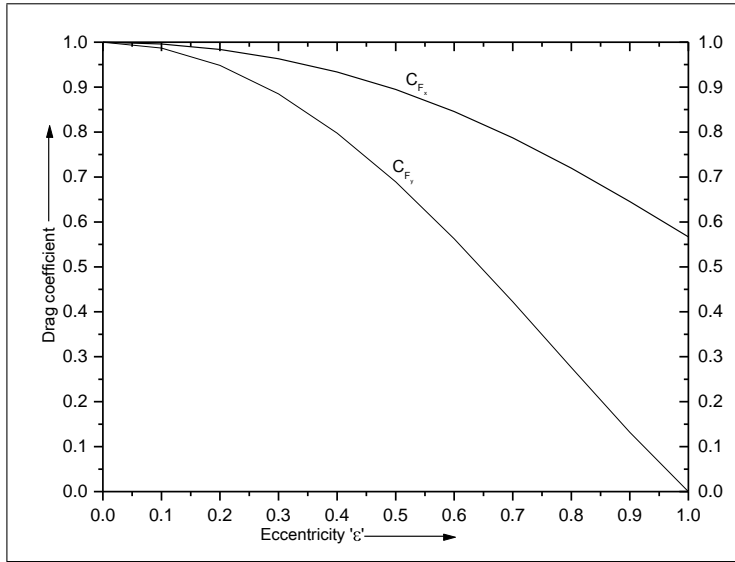


Figure 12. Variation of drag coefficient with respect to the eccentricity e for prolate spheroid body placed in axial and transverse stagnation like quadratic flow

Table 7. Numerical values of drag coefficient (axial and transverse stagnation like quadratic flow) for prolate spheroid with respect to eccentricity e (depicted in Figure 12)[Calculated from equations (11.2b) and (??)]

	Axial	Transverse
	stagnation	
e	C_{F_x}	C_{F_y}
0	1.000000	1.000000
0.1	0.995990	0.987022
0.2	0.983847	0.948350
0.3	0.963242	0.884779
0.4	0.933688	0.797685
0.5	0.894658	0.689195
0.6	0.845791	0.562531
0.7	0.787188	0.422511
0.8	0.719729	0.276000
0.9	0.645306	0.131863
1	0.566800	0.000000

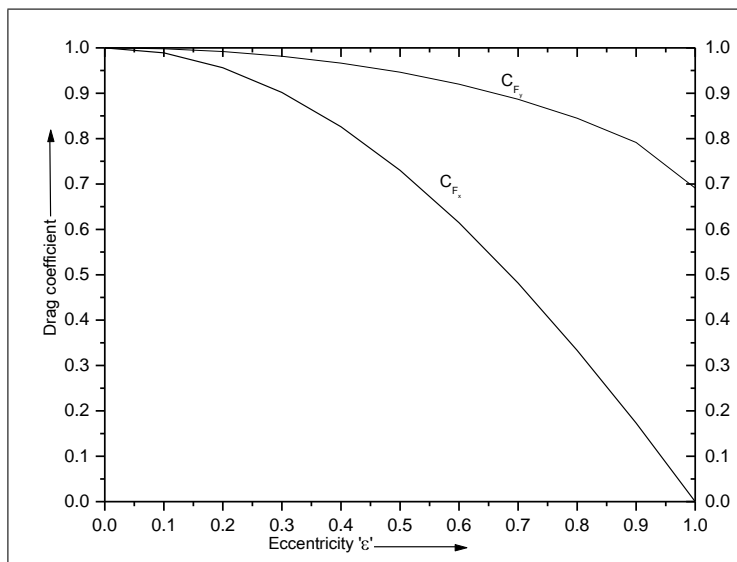


Figure 13. Variation of drag coefficient with respect to the eccentricity e for oblate spheroid body placed in axial and transverse stagnation like quadratic flow

Table 8. Numerical values of drag coefficient (axial and transverse stagnation like quadratic flow) for oblate spheroid with respect to eccentricity e (depicted in Figure 13)[Calculated from equations (12.2b) and (??)]

	Axial	Transverse
	stagnation	stagnation
e	C_{Fx}	C_{Fy}
0	1.000000	1.000000
0.1	0.989008	0.997994
0.2	0.956124	0.991909
0.3	0.901627	0.981531
0.4	0.82599	0.966489
0.5	0.729928	0.946228
0.6	0.614529	0.919985
0.7	0.481472	0.886711
0.8	0.333281	0.844916
0.9	0.173193	0.791535
1	0.000000	0.6910

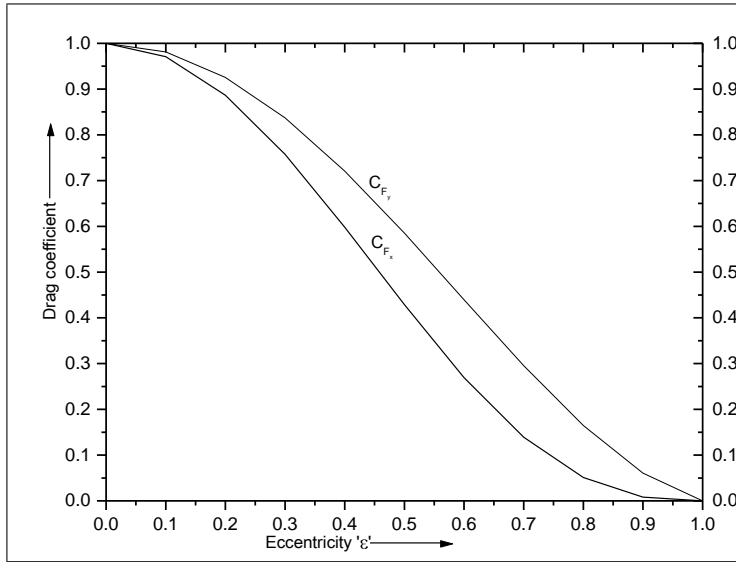


Figure 14. Variation of drag coefficient with respect to the eccentricity e for egg-shaped body placed in axial and transverse stagnation like quadratic flow

Table 9. Numerical values of drag coefficient (axial and transverse stagnation like quadratic flow) for egg-shaped body with respect to eccentricity e (depicted in Figure 14)[Calculated from equations (13.3b) and (13.6b)]

	Axial	Transverse
	stagnation	
e	C_{Fx}	C_{Fy}
0	1.0000000	1.000000
0.1	0.9707880	0.981099
0.2	0.8865610	0.925572
0.3	0.7572270	0.836916
0.4	0.5982050	0.72085
0.5	0.4287360	0.585173
0.6	0.2694380	0.439583
0.7	0.1391050	0.295358
0.8	0.05088870	0.164792
0.9	0.00818752	0.0605348
1	0.0000000	0.0000000

For axisymmetric case ($\alpha=1$), drag value decreases from 1 to 0 with respect to increasing eccentricity from 0 to 1. For non-symmetric cases ($\alpha = 2$ to 5), for specific body, drag value increases on moving from left to right in table. In both the flows (axial and transverse), for $e = 1$, the limiting case of slender body, drag comes out to be 0, which is again justified. It clearly indicates that for uniform and parabolic flows the drag on slender needle shaped body, drag comes out to be same. The variation of these drag values with respect to eccentricity e for various flow parameters α and β are depicted in Figure 10 and 11, respectively.

In Table 7, the numerical values of drag on prolate spheroid in axial and transverse stagnation like quadratic flow have been calculated with respect to eccentricity e . It is found that drag values decreases from 1 to 0.56680 in axial flow situation and decreases from 1 to 0 in transverse situation as eccentricity e increases from 0 to 1. It is interesting to observe that in the limiting case as $e = 1$, the case of slender or needle case, drag comes out to be non-zero ($= 0.56680$) while its value is zero in transverse flow situation. The variation of these drag values with respect to eccentricity e are depicted in Figure 12.

In Table 8, the numerical values of drag on oblate spheroid in axial and transverse stagnation like quadratic flow have been calculated with respect to eccentricity e . It is found that drag values decreases from 1 to 0 in axial flow situation and decreases from 1 to 0.6910 in transverse situation as eccentricity e increases from 0 to 1. It is interesting to observe that in the limiting case as $e = 1$, the case of flat circular disk, drag comes out to be 0 while its value is non-zero ($= 0.6910$) in transverse flow situation. The variation of these drag values with respect to eccentricity e are depicted in Figure 13.

In Table 9, the numerical values of drag on egg-shaped body in axial and transverse stagnation like quadratic flow have been calculated with respect to eccentricity e . It is found that drag values decreases from 1 to 0 in both axial and transverse stagnation flow situation as eccentricity e increases from 0 to 1. It is interesting to observe that in the limiting case as $e = 1$, the case of slender spheroid or needle like body, drag comes out to be 0. The variation of these drag values with respect to eccentricity e are depicted in Figure 14.

15. CONCLUSION

The authors have further developed the conjecture published in paper [1, 1999] by Datta and Srivastava and evaluated the general expressions of drag on axially symmetric bodies under the restrictions imposed in Section 2 placed in unbounded axial and transverse paraboloid as well as axial and transverse stagnation like paraboloid flows with appropriate choice of surface average velocity on body surface defined by Chwang and Wu [2, 3, 1975, parts 2 and 3]. These general expressions have been successfully applied not only to sphere and spheroid but also to egg-shaped body having left half semi-spherical and right half semi-spheroidal. The same may be applied to check on egg-shaped body when left half is spheroidal and right half is semi-spherical that the values of drag remains the same. The reason behind it is that the Stokes

flow does not distinguish the fore and aft symmetry of the body. It may be easily analyzed that the proposed new analytical technique is very easy in comparison to the singularity method provided by other workers in the past for quadratic flow. Authors are searching the avenues of this analysis further for non-linear Stokes flow and other type of quadratic complex flows.

Acknowledgements. First author convey his sincere thanks to University Grants Commission, New Delhi, India, for providing financial assistance under major research project scheme[F.N. 39-55/2010(SR), 24-12-2010] at the Department of Mathematics, B.S.N.V. Post Graduate College, Lucknow(U.P.), India. Authors are also thankful to the authorities of B.S.N.V. Post Graduate College, Lucknow, to provide basic infrastructure facilities during the preparation of the paper.

REFERENCES

1. DATTA, S. AND SRIVASTAVA, D. K.: *Stokes drag on axially symmetric bodies: a new approach*, Proc. Indian Acad. Sci.(Math. Sci.), **109**(4), (1999), 441-452.
2. CHWANG, A. T. AND WU, T. Y.: *Hydromechanics of low reynolds number flow. Part 2. Singularity method for stokes flows*, J. Fluid Mech., **67**(4), (1975), 787-815.
3. CHWANG, A. T.: *Hydromechanics of low Reynolds number flow. Part 3. Motion of a spheroidal particle in quadratic flows*, J. Fluid Mech., **72**, (1975), 17-34.
4. STOKES, G. G.: *On the effect of internal friction of fluids on pendulums*, Trans. Camb. Philos. Soc., **9**, (1851), 8-106.
5. OBERBECK, A.: *Über stationäre flüssigkeitsbewegungen mit berücksichtigung der inneren, Reibung*. J. reine angew. Math., **81**, (1876), 62-80.
6. EDWARDS, D.: *Steady motion of a viscous liquid in which ellipsoid is constrained to rotate about a principal axis*, Quart. J. Math., **26**, (1982), 70-78.
7. JEFFERY, G. B.: *The motion of ellipsoidal particles in a viscous fluid*, Proc. Roy. Soc. A. **102**, (1922), 161-179.
8. TAYLOR, G. I.: *The motion of ellipsoidal particles in a viscous fluid*, Proc. Roy. Soc. Lond., Ser. A, **103**(720), April 03 (1923), 58-61.
9. GOLDSTEIN, S.: *The forces on a solid body moving through viscous fluid*, Proc. Roy. Soc. Lond., Ser. A, **123**(791), March 06, (1929), 216-225.
10. LIGHTHILL, M. J.: *On the squirming motion of nearly spherical deformable bodies through liquids at very small Reynolds numbers*, Comm. Pure Appl. Math., **5**, 5, (1952), 109-118.
11. HILL, R. AND POWER, G.: *Extremum principles for slow viscous flow and the approximate calculation of drag*, Quart. J. Mech. Appl. Math., **9**(3), (1956), 313-319.
12. CHWANG, A. T. AND WU, T. Y.: *Hydromechanics of low reynolds number flow. Part 1. Rotation of axisymmetric prolate bodies*, J. Fluid Mech., **63**(3), (1974), 607-622.
13. CHWANG, A. T. AND WU, T. Y.: *Hydromechanics of low reynolds number flow. Part 4. Translation of spheroids*, J. Fluid Mech., **75**(4), (1976), 677-689.
14. JOHNSON, R. E. AND WU, T. Y.: *Hydromechanics of low Reynolds number flow, Part 5. Motion*, J. Fluid Mech., **95**(2), (1979), 263-277.

15. HO, B. P. AND LEAL, L. G.: *Migration of rigid spheres in a two-dimensional unidirectional shear flow of a second-order fluid*, J. Fluid Mech., **76**, (1976), 783-799.
16. PARKER, G. W.: *Projectile motion with air resistance quadratic in the speed*, American J. Physics, **45**(7), (1977), 606-610.
17. MAJHI, S. N. AND VASUDEVAIAH, M.: *Flow separation in a viscous parabolic shear past a sphere*, Acta Mech., **45**, (1982), 233-249.
18. KALONI, P. N.: *A note on the drag force on a spherical particle in a quadratic flow of a micropolar fluid*, Int. J. Engg. Science, **21**(8), (1983), 1001-1008.
19. KEH, HUAN J. AND ANDERSON, J. L.: *Configurational statistics of Brownian dumbbells in a quadratic flow*, J. Chem. Phys., **80**, (1984), 1632-1639.
20. YUAN, FAN AND WU WANG-YI: *The Stokes flow of an arbitrary prolate axisymmetric body towards an infinite plane wall*, Applied Mathematics and Mechanics, **8**(1), (1987) 17-30.
21. YANG, SEUNG-MAN AND HONG, WON-HI: *Motions of a porous particles in Stokes flow: Part 1. Unbounded single-fluid domain problem*, Korean J. Chem. Eng., **5**(1), (1988), 23-34.
22. SEKI, MASAKO SUGIHARA: *The motion of an ellipsoid in tube flow at low Reynolds number*, J. Fluid Mech., **324**, (1996), 287-308.
23. HABER, S. AND BRENNER, H.: *Symbolic operator solutions of Laplace's and Stokes equations. Part II. Stokes flow past a rigid sphere*, Chemical Engineering Communications, **27**(5-6), (1984), 297-311.
24. HABER, S. AND BRENNER, H.: *Hydrodynamic interactions of spherical particles in quadratic Stokes flows*, Int. J. Multiphase Flow, vol. **25**(6-7), (1999), 1009-1032.
25. PALANIAPPAN, D. AND DARIPA, PRABIR: *Compound droplet in extensional and paraboloidal flows*, Phys. Fluids, **12**(10), (2000), 2377-2385.
26. LIN, W., GRAHAM, A. L., INGBER, M. S., ABBOTT, J. R. AND LEGGOE, J. W.: *Hydrodynamic interaction of two neutrally-buoyant smooth spheres suspended in plane Poiseuille flow: the BEM simulations versus the MoR approximations*, Computational Mechanics, **36**(4), (2005), 307-319.
27. PASOL, L., SELLIER, A. AND FEUILLEBOIS, F.: *A sphere in a second degree polynomial creeping flow parallel to a wall*, Quart. J. Mech. Appl. Math., **59**(4), (2006), 587-614.
28. PRAKASH, J., RAJASEKHAR, G. P. AND KOHR, M.: *Faxen's law for arbitrary Stokes flow past a porous sphere*, Arch. Mech., **64**(1), (2012), 41-63.
29. SRIVASTAVA, D. K., YADAV, R. R. AND YADAV, S.: *Steady Stokes flow past deformed sphere. Class of oblate axi-symmetric bodies*, Int. J. Appl. Math. Mech., **8**(9), (2012), 17-53.
30. HAPPEL, J. AND BRENNER, H.: *Low Reynolds Number Hydrodynamics*. Nijhoff, Dordrecht, The Netherlands, 1964, 1983.
31. CHAN, P. C. H. AND LEAL, L. G.: *A note on the motion of a spherical particle in a general quadratic flow of a second-order fluid*, J. Fluid Mech., **82**, (1977), 549-559.

AXISYMMETRIC SHELL MODEL USING A THREE-FIELD DUAL-MIXED VARIATIONAL PRINCIPLE

BALÁZS TÓTH

Department of Mechanics, University of Miskolc
3515 Miskolc-Egyetemváros, Hungary
mechttb@uni-miskolc.hu

[Received: April 10, 2007]

Abstract. A dimensionally reduced axisymmetric shell model using a three-field complementary energy-based variational principle set up in terms of non-symmetric stresses, rotations and displacements is derived. Considering axisymmetrically loaded shells of revolution, a special form of the three-dimensional variational principle of Hellinger-Reissner is obtained and applied for the derivation of the Euler-Lagrange equations and natural boundary conditions of the shell model.

Mathematical Subject Classification:

Keywords: axisymmetric shell, three-field dual-mixed variational principle, dimensional reduction, Euler-Lagrange equations

1. INTRODUCTION

Mixed variational principles in elasticity offer the possibility of approximating the stress space directly. Complementary energy-based dual-mixed variational formulations and properly designed finite element models have the additional advantage that they provide better convergence rates and higher accuracy for the variables of primary interest, i.e. for the stresses, when compared to strain energy-based primal-mixed formulations and displacement-based formulations. Stress-based finite element models, furthermore, are known to be free from those numerical locking problems that appear in many displacement-based finite element models. These facts seem to be especially important for shell models and shell finite elements for which the modelling and approximation difficulties can lead to several type of numerical problems.

The main objective of this paper is to derive a dimensionally reduced axisymmetric shell model based on Hellinger-Reissner's three-field dual-mixed variational principle. Its functional can be derived from the total complementary energy functional

$$K_d(\sigma^{rs}) = -\frac{1}{2} \int_{(V)} \sigma^{kl} \varepsilon_{kl}(\sigma^{rs}) \, dV + \int_{(S_u)} \tilde{u}_k \sigma^{kl} n_l \, dS, \quad (1.1)$$

which depends on the stress tensor σ^{rs} alone. Here V denotes the volume of the body in the undeformed configuration, ε_{kl} is the symmetric strain tensor and \tilde{u}_k is the displacement vector prescribed on the surface part S_u with outward unit normal n_l . The subsidiary conditions to the total complementary energy functional (1.1) are the equilibrium equations

$$\sigma^{pq}_{;q} + b^p = 0 \quad x^m \in V, \quad (1.2)$$

where b^p stands for the body forces, the symmetry condition

$$\epsilon_{pqr}\sigma^{pq} = 0 \quad x^m \in V, \quad (1.3)$$

where ϵ_{pqr} is the covariant permutation tensor, and the stress boundary conditions

$$\tilde{p}^k = \sigma^{kl}n_l \quad x^m \in S_p, \quad (1.4)$$

where \tilde{p}^k are prescribed surface tractions on S_p with outward unit normal n_l (the surface of the body is $S = S_p \cup S_u$, $S_p \cap S_u = \emptyset$). For linear elastic materials the strain tensor ε_{kl} can be obtained from the inverse stress-strain relations (Hooke's law)

$$\varepsilon_{kl} = C_{klrs}^{-1}\sigma^{rs} \quad x^m \in V, \quad (1.5)$$

where the fourth-order tensor C_{klrs}^{-1} with symmetry properties $C_{klrs}^{-1} = C_{klsr}^{-1} = C_{rskl}^{-1}$ is the elastic compliance tensor.

Classical, complementary energy-based and dimensionally reduced shell models in terms of symmetric stresses can be derived using functional (1.1). In that case both the translational and rotational equilibrium equations, (1.2) and (1.3), as well as the stress boundary conditions (1.4) should be satisfied *a priori*. A dimensionally reduced cylindrical shell model based on this approach using second-order stress functions can be found in [3]. The related finite element formulation requires, however, C_1 continuous approximation of the second-order stress functions and this requirement, which is primarily due to the symmetry condition for the stress tensor, makes it rather difficult to establish a numerically efficient formulation for general shells.

One possibility to overcome the difficulties mentioned in connection with the derivation of numerically efficient stress-based shell models is the incorporation of the symmetry condition for the stress tensor into the principle by the use of the rotations as Lagrangian multipliers. A dimensionally reduced non-linear shell model using the corresponding dual-mixed variational principle of Fraeijs de Veubeke [6] has been derived in [4].

Another possibility for the derivation of dimensionally reduced stress-based shell models is to apply the three-field dual-mixed variational principle of Hellinger-Reissner [7, 9, 10]. The functional of this principle can be considered as the sum of the total complementary energy functional (1.1) and two Lagrangian multiplier terms which red ensure the fulfillment of the translational and rotational equilibrium equations, (1.2) and (1.3). In the linear theory of elasticity the functional red is of the form

$$HR_d(\sigma^{rs}, \phi^s, u_p) = - \int_{(V)} W_c(\sigma^{rs}) dV + \int_{(S_u)} \tilde{u}_p \sigma^{pq} n_q dS +$$

$$+ \int_{(V)} \sigma^{pq} \epsilon_{pq} \phi^s dV - \int_{(V)} u_p (\sigma^{pq}_{;q} + b^p) dV, \quad (1.6)$$

where σ^{rs} is the not *a priori* symmetric stress tensor, red the strain tensor ϵ_{pq} is a symmetric one, ϕ^s denotes the axial vector of the skew-symmetric rotation tensor, ψ_{pq} red which are related to each other via the equation

$$\psi_{pq} = -\epsilon_{pq} \phi^s, \quad (1.7)$$

\tilde{u}_p is the prescribed displacement vector on S_u with outward unit normal n_q and W_c is the complementary strain energy density defined by

$$W_c(\sigma^{rs}) = \frac{1}{2} \sigma^{pq} \epsilon_{pq}(\sigma^{rs}) = \frac{1}{2} C_{pqrs}^{-1} \sigma^{pq} \sigma^{rs}. \quad (1.8)$$

The only subsidiary conditions to be satisfied by functional (1.6) are the stress boundary conditions (1.4). It means that applying Hellinger-Reissner's dual-mixed principle with functional (1.6), *a priori* satisfaction of neither the translational nor the rotational equilibrium equations is required.

It is noted here that the classical two-field dual-mixed variational principle of Hellinger-Reissner with *a priori* symmetric stresses can also be used as a starting point for deriving dimensionally reduced stress-based shell models. The design of stable and efficient finite element models assuming symmetric stresses is, however, much more difficult than that with not *a priori* symmetric ones (for a discussion of the latter problem, see [5]).

This paper presents a dimensional reduction procedure for shells of revolution applying the three-dimensional dual-mixed variational principle of Hellinger-Reissner with functional (1.6). Section 2 contains the geometric description of the shell of revolution. In section 3 the three-dimensional equilibrium equations are derived in the curvilinear coordinate system attached to the shell middle surface. The dimensional reduction procedure is presented in Section 4. Applying truncated power series expansions, the independent variables, i.e., the stresses, the displacements and the rotations are approximated by polynomials of the first- and second-order in the thickness coordinate. After inserting the variables expanded into series into the special form of the Hellinger-Reissner functional for thin shells of revolution and introducing the notions of strain and rotation resultants as well as that of the prescribed displacement resultants, the Euler-Lagrange equations and the natural boundary conditions of the dimensionally reduced shell model are derived, assuming axisymmetrical loads. Section 5 contains some concluding remarks and an outlook for further research in the presented direction.

2. GEOMETRY OF THE SHELL OF REVOLUTION

Let x^k refer to a fixed right-handed orthogonal Cartesian frame in an Euclidean three-dimensional space, the corresponding base vectors are denoted by \mathbf{e}_k . We consider a shell of revolution as a three-dimensional body, the rotation axis of which is defined

by

$$0 \leq x^1 \leq L, \quad (2.1)$$

where L is the length of the shell (see Figure 1). The axisymmetric shell is a 3D

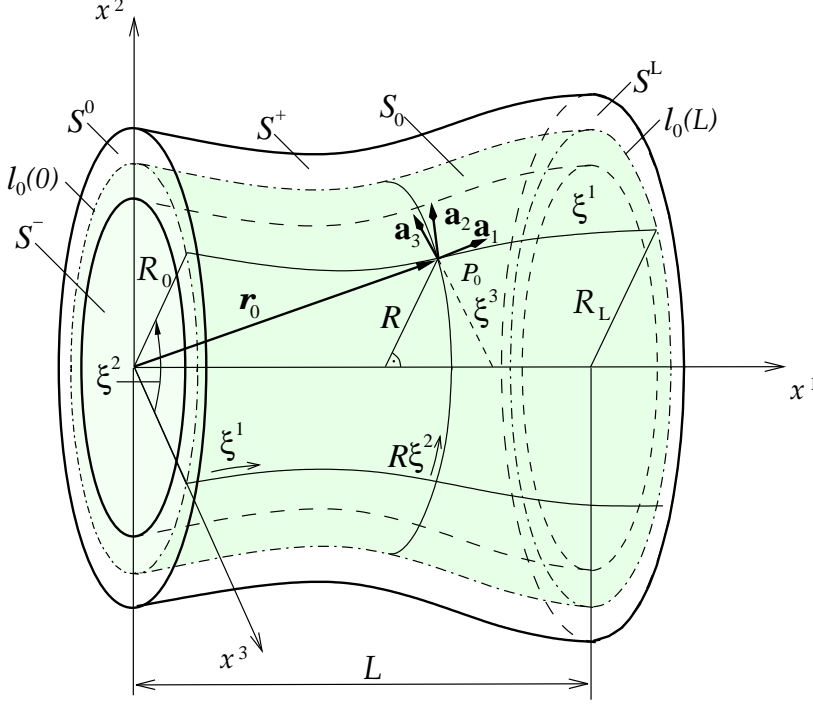


Figure 1. Axisymmetric shell

region bounded by two axisymmetric surfaces S^+ and S^- called the top and bottom surfaces which are symmetrically situated with respect to the surface S_0 called the middle surface, and the lateral surfaces S^0 and S^L , the intersections of which with S_0 are the circles $l_0(0)$ and $l_0(L)$, respectively (see Figure 1). The middle surface of the shell can be generated by rotating a curve about the x^1 -axis. This curve is the meridian curve defined by the function

$$R = R(x^1) > 0. \quad (2.2)$$

The shell is parametrized by the curvilinear coordinates ξ^m , with ξ^α called surface coordinates on S_0 and with ξ^3 which is the arc-length measured along the normal to the middle surface ($\xi^3 = 0$). Throughout this paper, the usual summation convention is used and the range of the Latin indices is 1, 2, 3 and that of the Greek indices is 1 and 2. The undeformed configuration of the shell is defined by

$$V = \left\{ \xi^m \mid \xi^\alpha \in S_0, \left| \xi^3 \right| \leq \frac{d}{2} \right\}, \quad (2.3)$$

where d , the distance between S^+ and S^- measured along ξ^3 , is the thickness of the shell. Henceforward it will be assumed that d is constant. The boundary of V , denoted by S , consists of the top and bottom surfaces

$$S^\pm = \left\{ \xi^m \mid \xi^\alpha \in S_0, \xi^3 = \pm \frac{d}{2} \right\} \quad (2.4)$$

and lateral surfaces

$$S^0 = \left\{ \xi^m \mid \xi^\alpha \in \ell_0(0), |\xi^3| \leq \frac{d}{2} \right\}, \quad (2.5)$$

$$S^L = \left\{ \xi^m \mid \xi^\alpha \in \ell_0(L), |\xi^3| \leq \frac{d}{2} \right\}. \quad (2.6)$$

The relation between the Cartesian coordinates x^k and the curvilinear coordinates ξ^α parametrizing the shell middle surface S_0 is given by

$$x^1 = f(\xi^1), \quad (2.7)$$

$$x^2 = R \sin \xi^2, \quad (2.8)$$

$$x^3 = R \cos \xi^2, \quad (2.9)$$

where ξ^1 is measured along the meridian curve and ξ^2 is the polar angle:

$$0 \leq \xi^2 < 2\pi \quad (2.10)$$

measured along the latitude circles lying in the planes perpendicular to the rotation axis (see Figure 1). The position vector of an arbitrary point $P_0 \in S_0$ can be written in the Cartesian coordinate frame as

$$\mathbf{r}_0 = x^k \mathbf{e}_k = x^1 \mathbf{e}_1 + R \sin \xi^2 \mathbf{e}_2 + R \cos \xi^2 \mathbf{e}_3. \quad (2.11)$$

Introducing the notations

$$A_1(x^1) = \frac{d\xi^1}{dx^1}, \quad \frac{1}{A_1(x^1)} = \frac{dx^1}{d\xi^1}, \quad (2.12)$$

the base vectors \mathbf{a}_α of the surface coordinate system can be obtained by deriving the position vector \mathbf{r}_0 (2.11) with respect to ξ^α :

$$\mathbf{a}_1 = \frac{\partial \mathbf{r}_0}{\partial \xi^1} = \frac{1}{A_1} \mathbf{e}_1 + \frac{1}{A_1} R' \sin \xi^2 \mathbf{e}_2 + \frac{1}{A_1} R' \cos \xi^2 \mathbf{e}_3 = \mathbf{a}^1, \quad (2.13)$$

$$\mathbf{a}_2 = \frac{\partial \mathbf{r}_0}{\partial \xi^2} = R \cos \xi^2 \mathbf{e}_2 - R \sin \xi^2 \mathbf{e}_3 = R^2 \mathbf{a}^2. \quad (2.14)$$

The base vector \mathbf{a}_3 , which is a normal to the middle surface S_0 , is obtained as

$$\mathbf{a}_3 = \frac{\mathbf{a}_1 \times \mathbf{a}_2}{|\mathbf{a}_1 \times \mathbf{a}_2|} = \frac{1}{A_1} (\sin \xi^2 \mathbf{e}_2 + \cos \xi^2 \mathbf{e}_3 - R' \mathbf{e}_1) = \mathbf{a}^3, \quad (2.15)$$

where the prime in the superscript indicates differentiation with respect to the coordinate x^1 . Making use of equations (2.13)–(2.15), the matrices of the covariant and contravariant metric tensor on the middle surface are obtained as

$$[a_{k\ell}] = \begin{bmatrix} 1 & 0 & 0 \\ 0 & R^2 & 0 \\ 0 & 0 & 1 \end{bmatrix}, \quad [a^{pq}] = \begin{bmatrix} 1 & 0 & 0 \\ 0 & \frac{1}{R^2} & 0 \\ 0 & 0 & 1 \end{bmatrix}. \quad (2.16)$$

The covariant base vectors at an arbitrary shell point P are denoted by \mathbf{g}_l (see Figure 2). The covariant metric tensor at P is denoted by g_{kl} ($g_{3\beta} = 0$). The Christoffel

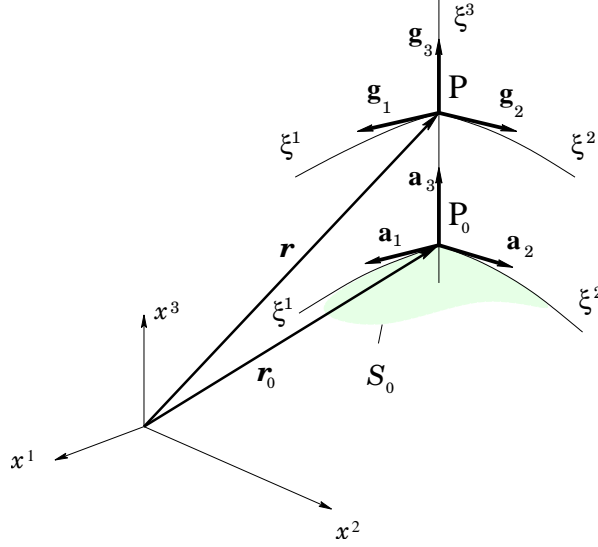


Figure 2. Local coordinate systems and their base vectors

symbols of the second kind on the middle surface S_0 are defined by the equations

$$\bar{\Gamma}_{sm}^k = \mathbf{a}_{s,m} \cdot \mathbf{a}^k, \quad \bar{\Gamma}_{\alpha\beta}^\kappa = \mathbf{a}_{\alpha,\beta} \cdot \mathbf{a}^\kappa, \quad \bar{\Gamma}_{\lambda 3}^\mu = \bar{\Gamma}_{33}^m = \bar{\Gamma}_{3\kappa}^3 = \bar{\Gamma}_{\lambda 3}^3 = 0, \quad (2.17)$$

where the subscripts m or β preceded by a coma mean partial differentiation with respect to the corresponding coordinates ξ^m or ξ^β . The curvature tensor of the middle surface is given by

$$b_{\kappa\lambda} = \bar{\Gamma}_{\kappa\lambda}^3, \quad b_\kappa^\mu = \bar{\Gamma}_{3\kappa}^\mu. \quad (2.18)$$

The relation between the covariant and contravariant base vectors at P and $P_0 \in S_0$ is written in the following form:

$$\mathbf{g}_l = \mu_l^k \mathbf{a}_k, \quad \mathbf{g}^m = (\mu^{-1})_p^m \mathbf{a}^p, \quad (2.19)$$

where μ_l^k and $(\mu^{-1})_p^m$ are, respectively, the shifter and the inverse shifter. Making use of (2.19) an arbitrary tensor \mathbf{T} defined at the point P of the shell can be shifted to the point P_0 of the middle surface:

$$\mathbf{T} = T_k^\ell \mathbf{g}^k \mathbf{g}_\ell = \bar{T}_m^n \mathbf{a}^m \mathbf{a}_n, \quad (2.20)$$

where a bar over a tensor variable denotes its tensorial components related to the base vectors \mathbf{a}_k of the shell middle surface, and

$$\bar{T}_m^n = T_k^\ell (\mu^{-1})_m^k \mu_\ell^n \quad (2.21)$$

are the shifted tensor components. Thus the covariant derivative tensor $T^{pq}_{;m}$ can be obtained by

$$T^{pq}_{;m} = \bar{T}^{kl}_{|m} (\mu^{-1})^p_k (\mu^{-1})^q_l, \quad (2.22)$$

where

$$\bar{T}^{kl}_{|m} = \bar{T}^{kl}_{,m} + \bar{\Gamma}^k_{sm} \bar{T}^{sl} + \bar{\Gamma}^l_{rm} \bar{T}^{kr} \quad (2.23)$$

is the three-dimensional covariant derivative on the middle surface S_0 . The covariant derivative (2.23) can be separated into

$$\bar{T}^{kl}_{|\nu} = \bar{T}^{kl}_{,\nu} + \bar{\Gamma}^k_{s\nu} \bar{T}^{sl} + \bar{\Gamma}^l_{r\nu} \bar{T}^{kr} \quad (2.24)$$

and

$$\bar{T}^{kl}_{|3} = \bar{T}^{kl}_{,3}. \quad (2.25)$$

In the case of axisymmetric shells the non-zero components of the Christoffel symbols (2.17) and the curvature tensor (2.18) are, respectively,

$$\bar{\Gamma}^2_{12} = \bar{\Gamma}^2_{21} = \frac{R'}{RA_1}, \quad \bar{\Gamma}^1_{22} = -\frac{RR'}{A_1} \quad (2.26)$$

and

$$b_{11} = \bar{\Gamma}^3_{11} = \frac{R''}{A_1^3}, \quad b_{22} = \bar{\Gamma}^3_{22} = -\frac{R}{A_1}, \quad (2.27)$$

$$b_1^1 = -\frac{1}{R_1} = -\bar{\Gamma}^1_{31} = \frac{R''}{A_1^3}, \quad b_2^2 = -\frac{1}{R_2} = -\bar{\Gamma}^2_{32} = -\frac{1}{RA_1}, \quad (2.28)$$

where R_1 and R_2 are the principal radii of curvature of the middle surface S_0 . In view of (2.28), the matrix of the shifter (2.19) can be represented by

$$[\mu_l^k] = \begin{bmatrix} 1 - \frac{R''}{A_1^3} \xi^3 & 0 & 0 \\ 0 & 1 + \frac{1}{RA_1} \xi^3 & 0 \\ 0 & 0 & 1 \end{bmatrix}. \quad (2.29)$$

For thin shells, the thickness is assumed to be small, i.e., the relations

$$\frac{d}{L} \ll 1, \quad \frac{d}{R_{\min}} \ll 1 \quad (2.30)$$

hold true, where

$$R_{\min} = \min_{x^1 \in [0; L]} \{|R_1|, |R_2|\}, \quad (2.31)$$

thus

$$\mu_l^k \cong (\mu^{-1})_l^k \cong \delta_l^k, \quad \mu = 1, \quad (2.32)$$

where μ is the determinant of the shifter (2.29). For thin shells of revolution, the volume element dV and the surface elements dS^0 and dS^L are given by

$$dV = R d\xi^1 d\xi^2 d\xi^3, \quad (2.33)$$

$$dS^0 = R_0 d\xi^2 d\xi^3, \quad (2.34)$$

$$dS^L = R_L d\xi^2 d\xi^3, \quad (2.35)$$

where

$$R = R(x^1 = 0) = R_0, \quad R = R(x^1 = L) = R_L. \quad (2.36)$$

3. EQUILIBRIUM EQUATIONS OF SHELLS OF REVOLUTION

The three-dimensional equilibrium equations of the axisymmetric shells are derived from equations (1.2). Using the derivation rule (2.22) and the geometric properties (2.30)–(2.32), the three-dimensional translational equilibrium equations for thin shells can be written in the following form:

$$\bar{\sigma}^{pl}_{|l} + \bar{b}^p = 0 \quad \xi^m \in V. \quad (3.1)$$

Making use of equations (2.26)–(2.28) obtained for the Christoffel symbols, the three-dimensional scalar equilibrium equations (3.1) can be written as

$$\bar{\sigma}^{11}_{,1} - \frac{R''}{A_1^3} (\bar{\sigma}^{31} + \bar{\sigma}^{13}) + \bar{\sigma}^{12}_{,2} + \frac{1}{RA_1} (R' \bar{\sigma}^{11} + \bar{\sigma}^{13}) - \frac{RR'}{A_1} \bar{\sigma}^{22} + \bar{\sigma}^{13}_{,3} + \bar{b}^1 = 0, \quad (3.2)$$

$$\bar{\sigma}^{21}_{,1} - \frac{R''}{A_1^3} \bar{\sigma}^{23} + \bar{\sigma}^{22}_{,2} + \frac{R'}{RA_1} (\bar{\sigma}^{12} + 2\bar{\sigma}^{21}) + \frac{1}{RA_1} (\bar{\sigma}^{23} + \bar{\sigma}^{32}) + \bar{\sigma}^{23}_{,3} + \bar{b}^2 = 0, \quad (3.3)$$

$$\bar{\sigma}^{31}_{,1} + \frac{R''}{A_1^3} (\bar{\sigma}^{11} - \bar{\sigma}^{33}) + \bar{\sigma}^{32}_{,2} + \frac{1}{RA_1} (R' \bar{\sigma}^{31} + \bar{\sigma}^{33}) - \frac{R}{A_1} \bar{\sigma}^{22} + \bar{\sigma}^{33}_{,3} + \bar{b}^3 = 0. \quad (3.4)$$

For axisymmetrically loaded shells of revolution the differentiation with respect to ξ^2 leads to zero, thus the equations (3.2)–(3.4) can be simplified to

$$\bar{\sigma}^{11}_{,1} - \frac{R''}{A_1^3} (\bar{\sigma}^{31} + \bar{\sigma}^{13}) + \frac{1}{RA_1} (R' \bar{\sigma}^{11} + \bar{\sigma}^{13}) - \frac{RR'}{A_1} \bar{\sigma}^{22} + \bar{\sigma}^{13}_{,3} + \bar{b}^1 = 0, \quad (3.5)$$

$$\bar{\sigma}^{21}_{,1} - \frac{R''}{A_1^3} \bar{\sigma}^{23} + \frac{R'}{RA_1} (\bar{\sigma}^{12} + 2\bar{\sigma}^{21}) + \frac{1}{RA_1} (\bar{\sigma}^{23} + \bar{\sigma}^{32}) + \bar{\sigma}^{23}_{,3} + \bar{b}^2 = 0, \quad (3.6)$$

$$\bar{\sigma}^{31}_{,1} + \frac{R''}{A_1^3} (\bar{\sigma}^{11} - \bar{\sigma}^{33}) + \frac{1}{RA_1} (R' \bar{\sigma}^{31} + \bar{\sigma}^{33}) - \frac{R}{A_1} \bar{\sigma}^{22} + \bar{\sigma}^{33}_{,3} + \bar{b}^3 = 0. \quad (3.7)$$

These two-dimensional scalar equilibrium equations can be separated into two independent groups according to the stress components. Equations (3.5) and (3.7) involve the stress components $\bar{\sigma}^{11}$, $\bar{\sigma}^{22}$, $\bar{\sigma}^{13}$, $\bar{\sigma}^{31}$ and $\bar{\sigma}^{33}$ which describe the bending-shearing problems (including tension-compression) of the axisymmetric shell while equation (3.6) describes the torsion problem of the shell. The corresponding stress components are $\bar{\sigma}^{12}$, $\bar{\sigma}^{21}$, $\bar{\sigma}^{23}$ and $\bar{\sigma}^{32}$.

4. DIMENSIONALLY REDUCED AXISYMMETRIC SHELL MODEL

4.1. Approximation of the stress components along the thickness. Let us consider a shell of revolution loaded axisymmetrically. Then the problem is a two dimensional one – each quantity depends on ξ^1 and ξ^3 only. The components of the tensor variables are assumed to be shifted to the points of the middle surface. The fundamental variables of the two-dimensional problems can be expanded in power series with respect to the thickness coordinate ξ^3 . After being expanded into series

the stresses $\bar{\sigma}^{kl}$, the rotation components $\bar{\phi}^m$ and the displacements \bar{u}_n can be written as

$$\bar{\sigma}^{kl}(\xi^1, \xi^3) = \sum_{i=0}^{\infty} {}_i\bar{\sigma}^{kl}(\xi^1) (\xi^3)^i, \quad (4.1)$$

$$\bar{\phi}^m(\xi^1, \xi^3) = \sum_{i=0}^{\infty} {}_i\bar{\phi}^m(\xi^1) (\xi^3)^i, \quad (4.2)$$

$$\bar{u}_n(\xi^1, \xi^3) = \sum_{i=0}^{\infty} {}_i\bar{u}_n(\xi^1) (\xi^3)^i, \quad (4.3)$$

where the rotation coefficients ${}_i\bar{\phi}^m(\xi^1)$, the stress coefficients ${}_i\bar{\sigma}^{kl}(\xi^1)$ and the displacement coefficients ${}_i\bar{u}_n(\xi^1)$ depend only on the surface coordinate ξ^1 . Substituting stress components (4.1) into the two-dimensional scalar equilibrium equations (3.5)–(3.7) and making separation with respect to the powers of the thickness coordinate ξ^3 , the following one-dimensional equilibrium equations are obtained for the one-dimensional stress coefficients:

$$\begin{aligned} {}_i\bar{\sigma}^{11}_{,1} - \frac{R''}{A_1^3} ({}_i\bar{\sigma}^{31} + {}_i\bar{\sigma}^{13}) + \frac{1}{RA_1} (R' {}_i\bar{\sigma}^{11} + {}_i\bar{\sigma}^{13}) - \frac{RR'}{A_1} {}_i\bar{\sigma}^{22} + \\ + (i+1) {}_{i+1}\bar{\sigma}^{13} + {}_i\bar{b}^1 = 0, \quad i = 0, 1, 2, \dots, \end{aligned} \quad (4.4)$$

$$\begin{aligned} {}_i\bar{\sigma}^{21}_{,1} - \frac{R''}{A_1^3} {}_i\bar{\sigma}^{23} + \frac{R'}{RA_1} ({}_i\bar{\sigma}^{12} + 2{}_i\bar{\sigma}^{21}) + \frac{1}{RA_1} ({}_i\bar{\sigma}^{23} + {}_i\bar{\sigma}^{32}) + \\ + (i+1) {}_{i+1}\bar{\sigma}^{23} + {}_i\bar{b}^2 = 0, \quad i = 0, 1, 2, \dots, \end{aligned} \quad (4.5)$$

$$\begin{aligned} {}_i\bar{\sigma}^{31}_{,1} + \frac{R''}{A_1^3} ({}_i\bar{\sigma}^{11} - {}_i\bar{\sigma}^{33}) + \frac{1}{RA_1} (R' {}_i\bar{\sigma}^{31} + {}_i\bar{\sigma}^{33}) - \frac{R}{A_1} {}_i\bar{\sigma}^{22} + \\ + (i+1) {}_{i+1}\bar{\sigma}^{33} + {}_i\bar{b}^3 = 0, \quad i = 0, 1, 2, \dots. \end{aligned} \quad (4.6)$$

Depending on the number of equations selected from the above equilibrium equations, a large number of dimensionally reduced axisymmetric shell models can be derived. In this paper a shell model, which is based on the equations valid for $i = 0$ and $i = 1$, is investigated assuming that the higher-order equilibrium equations are identically satisfied. In this case the stress components $\bar{\sigma}^{k\lambda}$ and $\bar{\sigma}^{k3}$ are approximated, respectively, by polynomials of the first- and second-degree in ξ^3 :

$$\bar{\sigma}^{k\lambda}(\xi^1, \xi^3) = {}_0\bar{\sigma}^{k\lambda}(\xi^1) + {}_1\bar{\sigma}^{k\lambda}(\xi^1) \xi^3, \quad (4.7)$$

$$\bar{\sigma}^{k3}(\xi^1, \xi^3) = {}_0\bar{\sigma}^{k3}(\xi^1) + {}_1\bar{\sigma}^{k3}(\xi^1) \xi^3 + {}_2\bar{\sigma}^{k3}(\xi^1) (\xi^3)^2. \quad (4.8)$$

The corresponding one-dimensional translational equilibrium equations for the 18 stress coefficients ${}_0\bar{\sigma}^{k\lambda}$, ${}_1\bar{\sigma}^{k\lambda}$, ${}_0\bar{\sigma}^{k3}$, ${}_1\bar{\sigma}^{k3}$, ${}_2\bar{\sigma}^{k3}$ are obtained from equations (4.7)–(4.8):

$${}_0\bar{\sigma}^{11}_{,1} - \frac{R''}{A_1^3} ({}_0\bar{\sigma}^{31} + {}_0\bar{\sigma}^{13}) + \frac{1}{RA_1} (R' {}_0\bar{\sigma}^{11} + {}_0\bar{\sigma}^{13}) - \frac{RR'}{A_1} {}_0\bar{\sigma}^{22} + {}_1\bar{\sigma}^{13} + {}_0\bar{b}^1 = 0, \quad (4.9)$$

$${}_0\bar{\sigma}^{21}_{,1} - \frac{R''}{A_1^3} {}_0\bar{\sigma}^{23} + \frac{R'}{RA_1} ({}_0\bar{\sigma}^{12} + 2{}_0\bar{\sigma}^{21}) + \frac{1}{RA_1} ({}_0\bar{\sigma}^{23} + {}_0\bar{\sigma}^{32}) + {}_1\bar{\sigma}^{23} + {}_0\bar{b}^2 = 0, \quad (4.10)$$

$${}_0\bar{\sigma}^{31}_{,1} + \frac{R''}{A_1^3} ({}_0\bar{\sigma}^{11} - {}_0\bar{\sigma}^{33}) + \frac{1}{RA_1} (R' {}_0\bar{\sigma}^{31} + {}_0\bar{\sigma}^{33}) - \frac{R}{A_1} {}_0\bar{\sigma}^{22} + {}_1\bar{\sigma}^{33} + {}_0\bar{b}^3 = 0, \quad (4.11)$$

and

$${}_1\bar{\sigma}^{11}_{,1} - \frac{R''}{A_1^3} ({}_1\bar{\sigma}^{31} + {}_1\bar{\sigma}^{13}) + \frac{1}{RA_1} (R' {}_1\bar{\sigma}^{11} + {}_1\bar{\sigma}^{13}) - \frac{RR'}{A_1} {}_1\bar{\sigma}^{22} + {}_2\bar{\sigma}^{13} + {}_1\bar{b}^1 = 0, \quad (4.12)$$

$${}_1\bar{\sigma}^{21}_{,1} - \frac{R''}{A_1^3} {}_1\bar{\sigma}^{23} + \frac{R'}{RA_1} ({}_1\bar{\sigma}^{12} + 2{}_1\bar{\sigma}^{21}) + \frac{1}{RA_1} ({}_1\bar{\sigma}^{23} + {}_1\bar{\sigma}^{32}) + {}_2\bar{\sigma}^{23} + {}_1\bar{b}^2 = 0, \quad (4.13)$$

$${}_1\bar{\sigma}^{31}_{,1} + \frac{R''}{A_1^3} ({}_1\bar{\sigma}^{11} - {}_1\bar{\sigma}^{33}) + \frac{1}{RA_1} (R' {}_1\bar{\sigma}^{31} + {}_1\bar{\sigma}^{33}) - \frac{R}{A_1} {}_1\bar{\sigma}^{22} + {}_2\bar{\sigma}^{33} + {}_1\bar{b}^3 = 0. \quad (4.14)$$

The rotation components $\bar{\phi}^m(\xi^1)$ and the displacement components $\bar{u}_n(\xi^1)$ are approximated by polynomials of the first-degree in ξ^3 :

$$\bar{\phi}^m(\xi^1, \xi^3) = {}_0\bar{\phi}^m(\xi^1) + {}_1\bar{\phi}^m(\xi^1)\xi^3, \quad (4.15)$$

and

$$\bar{u}_n(\xi^1, \xi^3) = {}_0\bar{u}_n(\xi^1) + {}_1\bar{u}_n(\xi^1)\xi^3, \quad (4.16)$$

where ${}_0\bar{\phi}^m$, ${}_1\bar{\phi}^m$ and ${}_0\bar{u}_n$, ${}_1\bar{u}_n$ are, respectively, the rotation and displacement coefficients.

4.2. Stress boundary conditions and prescribed displacements. The stress boundary conditions on the top and bottom surfaces S^\pm of the shell can be written in the form

$$\boldsymbol{\sigma} \cdot \mathbf{n}^\pm = \boldsymbol{\sigma} \cdot (\pm \mathbf{a}_3) = \pm \bar{\sigma}^{k3} \mathbf{a}_k = \tilde{\mathbf{p}}^\pm, \quad \pm \bar{\sigma}^{k3} = (\tilde{p}^\pm)^k \quad \xi^m \in S^\pm, \quad (4.17)$$

where the outward unit normals are denoted by

$$\mathbf{n}^\pm = \bar{n}^\pm \mathbf{a}_3, \quad \bar{n}^\pm = \begin{cases} -1 & \text{on } S^-, \\ 1 & \text{on } S^+, \end{cases} \quad (4.18)$$

and $\tilde{\mathbf{p}}^\pm$ are prescribed surface tractions on S^\pm . Substituting (4.8) into the stress boundary conditions (4.17) and taking into account (4.18), we obtain the following equations:

$${}_0\bar{\sigma}^{k3} + {}_1\bar{\sigma}^{k3} \frac{d}{2} + {}_2\bar{\sigma}^{k3} \frac{d^2}{4} = (\tilde{p}^+)^k, \quad (4.19)$$

$$-{}_0\bar{\sigma}^{k3} + {}_1\bar{\sigma}^{k3} \frac{d}{2} - {}_2\bar{\sigma}^{k3} \frac{d^2}{4} = (\tilde{p}^-)^k. \quad (4.20)$$

Adding and subtracting the above equations, the one-dimensional vector-valued load coefficients on S^\pm are given by

$${}_0\tilde{p}^k(\xi^1) = \frac{1}{2} \left[(\tilde{p}^+)^k + (\tilde{p}^-)^k \right], \quad (4.21)$$

$${}_1\tilde{p}^k(\xi^1) = \frac{1}{d} \left[(\tilde{p}^+)^k - (\tilde{p}^-)^k \right]. \quad (4.22)$$

Making use of equations (4.21)–(4.22), the stress boundary conditions (4.19)–(4.20) can be manipulated into the form

$${}_1\bar{\sigma}^{k3} = \frac{2}{d} {}_0\tilde{p}^k, \quad (4.23)$$

$${}_2\bar{\sigma}^{k3} = -\frac{4}{d^2} {}_0\bar{\sigma}^{k3} + \frac{2}{d} {}_1\tilde{p}^k, \quad (4.24)$$

where

$$\tilde{p}^k(\xi^1, \xi^3) = {}_0\tilde{p}^k + {}_1\tilde{p}^k \xi^3, \quad (4.25)$$

and

$$\tilde{p}^k(\xi^1, \xi^3 = \pm d/2) = (\tilde{p}^\pm)^k = {}_0\tilde{p}^k \pm \frac{d}{2} {}_1\tilde{p}^k. \quad (4.26)$$

The outward unit normals of the lateral surfaces S^0 and S^L can be given by

$$\mathbf{n}^\times = \bar{n}^\times \mathbf{a}_1, \quad \bar{n}^\times = \begin{cases} -1 & \text{on } S^0, \\ 1 & \text{on } S^L. \end{cases} \quad (4.27)$$

Let $\tilde{\mathbf{p}}^\times$ be the prescribed surface traction on the lateral surface S^L with outward unit normal \mathbf{n}^\times defined by equation (4.27). The stress boundary conditions on S^L can be written in the form

$$\boldsymbol{\sigma} \cdot \mathbf{n}^\times = \boldsymbol{\sigma} \cdot \mathbf{a}^1 = \bar{\sigma}^{k1} \mathbf{a}_k = \tilde{\mathbf{p}}^\times, \quad \bar{\sigma}^{k1} = (\tilde{p}^\times)^k \quad \xi^m \in S^L. \quad (4.28)$$

Expanding the prescribed lateral surface tractions $(\tilde{p}^\times)^k$ into a truncated power series with respect to ξ^3 and substituting (4.7) into (4.28), we obtain the following stress boundary conditions on the lateral surface S^L :

$${}_0\bar{\sigma}^{k1}|_{x^1=L} = {}_0(\tilde{p}^\times)^k \quad \xi^m \in S^L, \quad (4.29)$$

$${}_1\bar{\sigma}^{k1}|_{x^1=L} = {}_1(\tilde{p}^\times)^k \quad \xi^m \in S^L, \quad (4.30)$$

where ${}_0(\tilde{p}^\times)^k$ and ${}_1(\tilde{p}^\times)^k$ are the prescribed one-dimensional vector-valued load coefficients on the lateral surface S^L .

Considering expression (4.16), the displacement boundary conditions on the lateral surface S^0 with outward unit normal \mathbf{n}^\times can be given by

$$\bar{u}_k = {}_0\bar{u}_k + {}_1\bar{u}_k \xi^3 = \tilde{u}_k = {}_0\tilde{u}_k + {}_1\tilde{u}_k \xi^3 \quad \xi^m \in S^0, \quad (4.31)$$

or

$${}_0\bar{u}_k|_{\xi^1=0} = {}_0\tilde{u}_k \quad \xi^m \in S^0, \quad (4.32)$$

$${}_1\bar{u}_k|_{\xi^1=0} = {}_1\tilde{u}_k \quad \xi^m \in S^0, \quad (4.33)$$

where ${}_0\tilde{u}_k$, ${}_1\tilde{u}_k$ are prescribed displacement coefficients on the lateral surface S^0 .

4.3. Euler-Lagrange equations and natural boundary conditions. Assuming linearly elastic, homogeneous and isotropic materials, the strain tensor $\bar{\varepsilon}_{kl}$ for thin shells can be expressed by the inverse stress-strain relation (Hooke's law)

$$\bar{\varepsilon}_{kl}(\bar{\sigma}^{rs}) = \frac{1}{4G} \left[(\bar{\sigma}^{rs} + \bar{\sigma}^{sr}) a_{rk} a_{sl} - \frac{2\nu}{1+\nu} \bar{\sigma}^{pq} a_{pq} a_{kl} \right], \quad (4.34)$$

where G is the shear modulus of elasticity and ν is the Poisson ratio. Making use of equation (2.16), the above constitutive equations can be written in the following form:

$$\bar{\varepsilon}_{11} = \frac{1}{E} [\bar{\sigma}^{11} - \nu (R^2 \bar{\sigma}^{22} + \bar{\sigma}^{33})], \quad (4.35)$$

$$\bar{\varepsilon}_{22} = \frac{R^2}{E} [R^2 \bar{\sigma}^{22} - \nu (\bar{\sigma}^{11} + \bar{\sigma}^{33})], \quad (4.36)$$

$$\bar{\varepsilon}_{33} = \frac{1}{E} [\bar{\sigma}^{33} - \nu (\bar{\sigma}^{11} + R^2 \bar{\sigma}^{22})], \quad (4.37)$$

$$\bar{\varepsilon}_{31} = \frac{1}{4G} (\bar{\sigma}^{13} + \bar{\sigma}^{31}) = \bar{\varepsilon}_{13}, \quad (4.38)$$

$$\bar{\varepsilon}_{21} = \frac{R^2}{4G} (\bar{\sigma}^{12} + \bar{\sigma}^{21}) = \bar{\varepsilon}_{12}, \quad (4.39)$$

$$\bar{\varepsilon}_{32} = \frac{R^2}{4G} (\bar{\sigma}^{23} + \bar{\sigma}^{32}) = \bar{\varepsilon}_{23}, \quad (4.40)$$

where $E = 2G(1+\nu)$ is the elasticity modulus. In the case of axisymmetric shells, the outward unit normal to the lateral surface $S_u \equiv S^0$ is defined by (4.27). In view of this, the Hellinger-Reissner functional (1.6) for thin shells can be written in the form

$$\begin{aligned} HR_d(\bar{\sigma}^{rs}, \bar{\phi}^m, \bar{u}_n) = & -\frac{1}{2} \int_{-\frac{d}{2}(S_0)}^{+\frac{d}{2}} \int \bar{\sigma}^{kl} \bar{\varepsilon}_{kl}(\bar{\sigma}^{rs}) dS_0 d\xi^3 - \int_{-\frac{d}{2}}^{+\frac{d}{2}} \int_0^{2\pi} \tilde{u}_k \bar{\sigma}^{k1} R_0 d\xi^2 d\xi^3 + \\ & + \int_{-\frac{d}{2}(S_0)}^{+\frac{d}{2}} \int \bar{\sigma}^{kl} \bar{\varepsilon}_{klm} \bar{\phi}^m dS_0 d\xi^3 - \int_{-\frac{d}{2}(S_0)}^{+\frac{d}{2}} \int \bar{u}_n (\bar{\sigma}^{nl}|_l + \bar{b}^n) dS_0 d\xi^3. \end{aligned} \quad (4.41)$$

Since the axisymmetrical deformation means that tensor variables are independent of the coordinate ξ^2 , the integration with respect to ξ^2 can easily be carried out. Thus the first variation of (4.41) with respect to stresses $\bar{\sigma}^{kl}$, rotations $\bar{\phi}^m$ and displacements \bar{u}_n yields the Hellinger-Reissner variational principle in the following form

$$\begin{aligned} \frac{1}{2\pi} \delta HR_d(\bar{\sigma}^{rs}, \bar{\phi}^m, \bar{u}_n, \delta \bar{\sigma}^{rs}, \delta \bar{\phi}^m, \delta \bar{u}_n) = \\ - \int_{-\frac{d}{2}}^{+\frac{d}{2}} \int_0^{s_L} \delta \bar{\sigma}^{kl} \bar{\varepsilon}_{kl} R d\xi^1 d\xi^3 - \int_{-\frac{d}{2}}^{+\frac{d}{2}} \tilde{u}_k \delta \bar{\sigma}^{k1} R_0 d\xi^3 + \int_{-\frac{d}{2}}^{+\frac{d}{2}} \int_0^{s_L} \delta \bar{\sigma}^{kl} \bar{\varepsilon}_{klm} \bar{\phi}^m R d\xi^1 d\xi^3 + \end{aligned}$$

$$+ \int_{-\frac{d}{2}}^{\frac{d}{2}} \int_0^{s_L} \bar{\sigma}^{kl} \bar{\epsilon}_{klm} \delta \bar{\phi}^m R d\xi^1 d\xi^3 - \int_{-\frac{d}{2}}^{\frac{d}{2}} \int_0^{s_L} \bar{u}_n \delta \bar{\sigma}^{nl} R d\xi^1 d\xi^3 - \int_{-\frac{d}{2}}^{\frac{d}{2}} \int_0^{s_L} \delta \bar{u}_n \left(\bar{\sigma}^{nl} + \bar{b}^n \right) R d\xi^1 d\xi^3 = 0, \quad (4.42)$$

where

$$s_L = \int_{\hat{x}^1=0}^L A_1(\hat{x}^1) d\hat{x}^1 \quad (4.43)$$

is the arc-length measured along the meridian curve.

4.3.1. *The first variation of the complementary strain energy.* Making use of the expanded stress components (4.7)–(4.8), the first variation of the complementary strain energy of the shell can be written as

$$\begin{aligned} \frac{1}{2\pi} \int_{(V)} \delta W_c(\bar{\sigma}^{rs}) dV &= \int_{-\frac{d}{2}}^{\frac{d}{2}} \int_0^{s_L} \delta \bar{\sigma}^{kl} \bar{\epsilon}_{kl} R d\xi^1 d\xi^3 = \\ &= \int_{-\frac{d}{2}}^{\frac{d}{2}} \int_0^{s_L} \left[\delta_0 \bar{\sigma}^{kl} \bar{\epsilon}_{kl} + \delta_1 \bar{\sigma}^{kl} \bar{\epsilon}_{kl} \xi^3 + \delta_2 \bar{\sigma}^{k3} \bar{\epsilon}_{k3} (\xi^3)^2 \right] R d\xi^1 d\xi^3. \end{aligned} \quad (4.44)$$

Introducing the strain resultants

$$\bar{E}_{k\ell}^{(0)} := \int_{-\frac{d}{2}}^{\frac{d}{2}} \bar{\epsilon}_{k\ell} d\xi^3, \quad \bar{E}_{k\ell}^{(1)} := \int_{-\frac{d}{2}}^{\frac{d}{2}} \bar{\epsilon}_{k\ell} \xi^3 d\xi^3, \quad \bar{E}_{k3}^{(2)} := \int_{-\frac{d}{2}}^{\frac{d}{2}} \bar{\epsilon}_{k3} (\xi^3)^2 d\xi^3 \quad (4.45)$$

and inserting them into equation (4.44) the following expression is obtained:

$$\begin{aligned} \frac{1}{2\pi} \int_{(V)} \delta W_c(\bar{\sigma}^{rs}) dV &= \int_{-\frac{d}{2}}^{\frac{d}{2}} \int_0^{s_L} \delta \bar{\sigma}^{kl} \bar{\epsilon}_{kl} R d\xi^1 d\xi^3 = \\ &= \int_0^{s_L} \left[\delta_0 \bar{\sigma}^{kl} \bar{E}_{k\ell}^{(0)} + \delta_1 \bar{\sigma}^{kl} \bar{E}_{k\ell}^{(1)} + \delta_2 \bar{\sigma}^{k3} \bar{E}_{k3}^{(2)} \right] R d\xi^1. \end{aligned} \quad (4.46)$$

4.3.2. *The first variation of the boundary integral term.* Making use of the expanded stress components (4.7), the first variation of the boundary integral in equation (4.41) in terms of the variations of the one-dimensional stress coefficients can be written as

$$- \int_{-\frac{d}{2}}^{\frac{d}{2}} \tilde{u}_k \delta \bar{\sigma}^{k1} R_0 d\xi^3 = - \int_{-\frac{d}{2}}^{\frac{d}{2}} \left[\tilde{u}_k \delta_0 \bar{\sigma}^{k1} + \tilde{u}_k \delta_1 \bar{\sigma}^{k1} \xi^3 \right] R_0 d\xi^3. \quad (4.47)$$

Introducing the prescribed displacement resultants

$$\widetilde{\mathbf{U}}_k^{(0)} := \int_{-\frac{d}{2}}^{+\frac{d}{2}} \widetilde{u}_k d\xi^3, \quad \widetilde{\mathbf{U}}_k^{(1)} := \int_{-\frac{d}{2}}^{+\frac{d}{2}} \widetilde{u}_k \xi^3 d\xi^3 \quad (4.48)$$

and substituting these into equation (4.47), the first variation of the boundary integral term takes the form

$$- \int_{-\frac{d}{2}}^{+\frac{d}{2}} \widetilde{u}_k \delta \bar{\sigma}^{k1} R_0 d\xi^3 = -R_0 \widetilde{\mathbf{U}}_k^{(0)} \delta_0 \bar{\sigma}^{k1} - R_0 \widetilde{\mathbf{U}}_k^{(1)} \delta_1 \bar{\sigma}^{k1}. \quad (4.49)$$

4.3.3. The first variation of the Lagrangian multiplier terms. Making use of the expanded stress components (4.7)–(4.8) and rotation components (4.15), the first variations of the Lagrangian multiplier term

$$\int_{-\frac{d}{2}}^{+\frac{d}{2}} \int \bar{\sigma}^{kl} \bar{\epsilon}_{klm} \bar{\phi}^m dS_0 d\xi^3 \quad (4.50)$$

in functional (4.41) with respect to the stresses $\bar{\sigma}^{kl}$ and the rotations $\bar{\phi}^m$ are, respectively,

$$\begin{aligned} & \int_{-\frac{d}{2}}^{+\frac{d}{2}} \int_0^{s_L} \delta \bar{\sigma}^{kl} \bar{\epsilon}_{klm} \bar{\phi}^m R d\xi^1 d\xi^3 = \\ & = \int_{-\frac{d}{2}}^{+\frac{d}{2}} \int_0^{s_L} \left[\delta_0 \bar{\sigma}^{kl} \bar{\epsilon}_{klm} \bar{\phi}^m + \delta_1 \bar{\sigma}^{kl} \bar{\epsilon}_{klm} \bar{\phi}^m \xi^3 + \delta_2 \bar{\sigma}^{k3} \bar{\epsilon}_{k3m} \bar{\phi}^m (\xi^3)^2 \right] R d\xi^1 d\xi^3 \end{aligned} \quad (4.51)$$

and

$$\int_{-\frac{d}{2}}^{+\frac{d}{2}} \int_0^{s_L} \bar{\sigma}^{kl} \bar{\epsilon}_{klm} \delta \bar{\phi}^m R d\xi^1 d\xi^3 = \int_{-\frac{d}{2}}^{+\frac{d}{2}} \int_0^{s_L} \left[\bar{\sigma}^{kl} \bar{\epsilon}_{klm} \delta_0 \bar{\phi}^m + \bar{\sigma}^{kl} \bar{\epsilon}_{klm} \delta_1 \bar{\phi}^m \xi^3 \right] R d\xi^1 d\xi^3. \quad (4.52)$$

Introducing the rotation resultants

$$\bar{\Phi}_{kl}^{(0)} := - \int_{-\frac{d}{2}}^{+\frac{d}{2}} \bar{\epsilon}_{klm} \bar{\phi}^m d\xi^3, \quad \bar{\Phi}_{kl}^{(1)} := - \int_{-\frac{d}{2}}^{+\frac{d}{2}} \bar{\epsilon}_{klm} \bar{\phi}^m \xi^3 d\xi^3, \quad \bar{\Phi}_{k3}^{(2)} := - \int_{-\frac{d}{2}}^{+\frac{d}{2}} \bar{\epsilon}_{k3m} \bar{\phi}^m (\xi^3)^2 d\xi^3 \quad (4.53)$$

and substituting them into equation (4.51), expression (4.51) can be written in the following form:

$$\int_{-\frac{d}{2}}^{+\frac{d}{2}} \int_0^{s_L} \delta \bar{\sigma}^{kl} \bar{\epsilon}_{klm} \bar{\phi}^m R d\xi^1 d\xi^3 = - \int_0^{s_L} \left[\delta {}_0\bar{\sigma}^{kl} \bar{\Phi}_{kl}^{(0)} + \delta {}_1\bar{\sigma}^{kl} \bar{\Phi}_{kl}^{(1)} + \delta {}_0\bar{\sigma}^{k3} \bar{\Phi}_{k3}^{(2)} \right] R d\xi^1. \quad (4.54)$$

Let us investigate the integral (4.52) appearing in (4.42). Substituting the expanded stress components (4.7)–(4.8) into (4.52) and carrying out integrations with respect to ξ^3 , the equation (4.52) can be written as

$$\begin{aligned} \int_{-\frac{d}{2}}^{+\frac{d}{2}} \int_0^{s_L} \bar{\sigma}^{kl} \bar{\epsilon}_{klm} \delta \bar{\phi}^m R d\xi^1 d\xi^3 = \\ \int_0^{s_L} \left\{ d \left[({}_0\bar{\sigma}^{23} - {}_0\bar{\sigma}^{32}) \delta {}_0\bar{\phi}^1 + ({}_0\bar{\sigma}^{31} - {}_0\bar{\sigma}^{13}) \delta {}_0\bar{\phi}^2 + ({}_0\bar{\sigma}^{12} - {}_0\bar{\sigma}^{21}) \delta {}_0\bar{\phi}^3 \right] + \right. \\ \left. + \frac{d^3}{12} \left[({}_1\bar{\sigma}^{23} - {}_1\bar{\sigma}^{32}) \delta {}_1\bar{\phi}^1 + ({}_1\bar{\sigma}^{31} - {}_1\bar{\sigma}^{13}) \delta {}_1\bar{\phi}^2 + ({}_1\bar{\sigma}^{12} - {}_1\bar{\sigma}^{21}) \delta {}_1\bar{\phi}^3 + \right. \right. \\ \left. \left. + {}_2\bar{\sigma}^{23} \delta {}_0\bar{\phi}^1 - {}_2\bar{\sigma}^{13} \delta {}_0\bar{\phi}^2 \right] \right\} R^2 d\xi^1. \quad (4.55) \end{aligned}$$

According to (4.42), the coefficients of the rotation components $\delta {}_0\bar{\phi}^m, \delta {}_1\bar{\phi}^m$ in the above expression should be equal to zero:

$$\delta {}_0\bar{\phi}^1 : \quad {}_0\bar{\sigma}^{32} = {}_0\bar{\sigma}^{23} + \frac{d^2}{12} {}_2\bar{\sigma}^{23}, \quad (4.56)$$

$$\delta {}_0\bar{\phi}^2 : \quad {}_0\bar{\sigma}^{31} = {}_0\bar{\sigma}^{13} + \frac{d^2}{12} {}_2\bar{\sigma}^{13}, \quad (4.57)$$

$$\delta {}_0\bar{\phi}^3 : \quad {}_0\bar{\sigma}^{12} = {}_0\bar{\sigma}^{21}, \quad (4.58)$$

$$\delta {}_1\bar{\phi}^1 : \quad {}_1\bar{\sigma}^{32} = {}_1\bar{\sigma}^{23}, \quad (4.59)$$

$$\delta {}_1\bar{\phi}^2 : \quad {}_1\bar{\sigma}^{31} = {}_1\bar{\sigma}^{13}, \quad (4.60)$$

$$\delta {}_1\bar{\phi}^3 : \quad {}_1\bar{\sigma}^{12} = {}_1\bar{\sigma}^{21}. \quad (4.61)$$

It can easily be seen that equations (4.56)–(4.57) and (4.59)–(4.60) are equivalent to the symmetry of the transverse shear stresses satisfied in integral average sense. The advantage of equations (4.56)–(4.61) is that ${}_0\bar{\sigma}^{32}, {}_0\bar{\sigma}^{31}, {}_0\bar{\sigma}^{12}, {}_1\bar{\sigma}^{32}, {}_1\bar{\sigma}^{31}$ and ${}_1\bar{\sigma}^{12}$ are expressed in terms of the stress coefficients ${}_0\bar{\sigma}^{23}$ and ${}_2\bar{\sigma}^{23}, {}_0\bar{\sigma}^{13}$ and ${}_2\bar{\sigma}^{13}, {}_0\bar{\sigma}^{21}, {}_1\bar{\sigma}^{23}, {}_1\bar{\sigma}^{13}$ and ${}_1\bar{\sigma}^{21}$, respectively. Thus, not only the number of rotation variables but also the number of stress variables could further be reduced. After substituting the expanded displacement components (4.16) into equation (4.42) and carrying out the integration with respect to ξ^3 , the coefficients of the displacement components

$\delta_0 \bar{u}_k, \delta_1 \bar{u}_k$ should be equal to zero:

$${}_0\bar{\sigma}^{11}_{,1} - \frac{R''}{A_1^3} ({}_0\bar{\sigma}^{31} + {}_0\bar{\sigma}^{13}) + \frac{1}{RA_1} (R' {}_0\bar{\sigma}^{11} + {}_0\bar{\sigma}^{13}) - \frac{RR'}{A_1} {}_0\bar{\sigma}^{22} + {}_1\bar{\sigma}^{13} + {}_0\bar{b}^1 = 0, \quad (4.62)$$

$${}_0\bar{\sigma}^{21}_{,1} - \frac{R''}{A_1^3} {}_0\bar{\sigma}^{23} + \frac{R'}{RA_1} ({}_0\bar{\sigma}^{12} + 2{}_0\bar{\sigma}^{21}) + \frac{1}{RA_1} ({}_0\bar{\sigma}^{23} + {}_0\bar{\sigma}^{32}) + {}_1\bar{\sigma}^{23} + {}_0\bar{b}^2 = 0, \quad (4.63)$$

$${}_0\bar{\sigma}^{31}_{,1} + \frac{R''}{A_1^3} ({}_0\bar{\sigma}^{11} - {}_0\bar{\sigma}^{33}) + \frac{1}{RA_1} (R' {}_0\bar{\sigma}^{31} + {}_0\bar{\sigma}^{33}) - \frac{R}{A_1} {}_0\bar{\sigma}^{22} + {}_1\bar{\sigma}^{33} + {}_0\bar{b}^3 = 0, \quad (4.64)$$

and

$${}_1\bar{\sigma}^{11}_{,1} - \frac{R''}{A_1^3} ({}_1\bar{\sigma}^{31} + {}_1\bar{\sigma}^{13}) + \frac{1}{RA_1} (R' {}_1\bar{\sigma}^{11} + {}_1\bar{\sigma}^{13}) - \frac{RR'}{A_1} {}_1\bar{\sigma}^{22} + 2{}_2\bar{\sigma}^{13} + {}_1\bar{b}^1 = 0, \quad (4.65)$$

$${}_1\bar{\sigma}^{21}_{,1} - \frac{R''}{A_1^3} {}_1\bar{\sigma}^{23} + \frac{R'}{RA_1} ({}_1\bar{\sigma}^{12} + 2{}_1\bar{\sigma}^{21}) + \frac{1}{RA_1} ({}_1\bar{\sigma}^{23} + {}_1\bar{\sigma}^{32}) + 2{}_2\bar{\sigma}^{23} + {}_1\bar{b}^2 = 0, \quad (4.66)$$

$${}_1\bar{\sigma}^{31}_{,1} + \frac{R''}{A_1^3} ({}_1\bar{\sigma}^{11} - {}_1\bar{\sigma}^{33}) + \frac{1}{RA_1} (R' {}_1\bar{\sigma}^{31} + {}_1\bar{\sigma}^{33}) - \frac{R}{A_1} {}_1\bar{\sigma}^{22} + 2{}_2\bar{\sigma}^{33} + {}_1\bar{b}^3 = 0. \quad (4.67)$$

Thus we have obtained the one-dimensional equilibrium equations (4.9)–(4.14) for the one-dimensional stress coefficients.

Applying a similar procedure to the Lagrangian multiplier term

$$\int_{-\frac{d}{2}}^{+\frac{d}{2}} \int_0^{s_L} \bar{u}_n \delta \bar{\sigma}^{nl} |_l R d\xi^1 d\xi^3 \quad (4.68)$$

and taking into account the integration rule

$$\begin{aligned} \int_0^{s_L} {}_i\bar{u}_n \delta {}_i\bar{\sigma}^{n1}_{,1} R d\xi^1 &= [{}_i\bar{u}_n \delta {}_i\bar{\sigma}^{n1} R]_{\xi^1=0}^{\xi^1=s_L} - \\ &- \int_0^{s_L} {}_i\bar{u}_{n,1} \delta {}_i\bar{\sigma}^{n1} R d\xi^1 - \int_0^{s_L} {}_i\bar{u}_n \delta {}_i\bar{\sigma}^{n1} \frac{R'}{A_1} d\xi^1, \quad i = 0, 1, \end{aligned} \quad (4.69)$$

as well as expressions (4.46), (4.49) and (4.54), the coefficients of $\delta_0 \bar{\sigma}^{kl}$, $\delta_1 \bar{\sigma}^{kl}$ and $\delta_2 \bar{\sigma}^{k3}$ should be equal to zero, yielding the kinematic equations

$$\delta_0 \bar{\sigma}^{11}: \quad d {}_0\bar{u}_{1,1} - d \frac{R''}{A_1^3} {}_0\bar{u}_3 - \bar{\mathbf{E}}_{11}^{(0)} = 0, \quad (4.70)$$

$$\delta_0 \bar{\sigma}^{12}: \quad -d \frac{R'}{A_1} {}_0\bar{u}_2 - R \bar{\Phi}_{12}^{(0)} - R \bar{\mathbf{E}}_{12}^{(0)} = 0, \quad (4.71)$$

$$\delta_0 \bar{\sigma}^{13}: \quad d \left(\frac{RR''}{A_1^3} - \frac{1}{A_1} \right) {}_0\bar{u}_1 - R \bar{\Phi}_{13}^{(0)} - R \bar{\mathbf{E}}_{13}^{(0)} = 0, \quad (4.72)$$

$$\delta_0 \bar{\sigma}^{21} : \quad dR_0 \bar{u}_{2,1} - d \frac{R'}{A_1} {}_0 \bar{u}_2 - R \bar{\Phi}_{21}^{(0)} - R \bar{E}_{21}^{(0)} = 0, \quad (4.73)$$

$$\delta_0 \bar{\sigma}^{22} : \quad d \frac{RR'}{A_1} {}_0 \bar{u}_1 + d \frac{R}{A_1} {}_0 \bar{u}_3 - \bar{E}_{22}^{(0)} = 0, \quad (4.74)$$

$$\delta_0 \bar{\sigma}^{23} : \quad d \left(\frac{RR''}{A_1^3} - \frac{1}{A_1} \right) {}_0 \bar{u}_2 - R \bar{\Phi}_{23}^{(0)} - R \bar{E}_{23}^{(0)} = 0, \quad (4.75)$$

$$\delta_0 \bar{\sigma}^{31} : \quad d {}_0 \bar{u}_{3,1} + d \frac{R''}{A_1^3} {}_0 \bar{u}_1 - \bar{\Phi}_{31}^{(0)} - \bar{E}_{31}^{(0)} = 0, \quad (4.76)$$

$$\delta_0 \bar{\sigma}^{32} : \quad - \frac{d}{A_1} {}_0 \bar{u}_2 - R \bar{\Phi}_{32}^{(0)} - R \bar{E}_{32}^{(0)} = 0, \quad (4.77)$$

$$\delta_0 \bar{\sigma}^{33} : \quad d \left(\frac{RR''}{A_1^3} - \frac{1}{A_1} \right) {}_0 \bar{u}_3 - R \bar{E}_{33}^{(0)} = 0, \quad (4.78)$$

and

$$\delta_1 \bar{\sigma}^{11} : \quad \frac{d^3}{12} \left({}_1 \bar{u}_{1,1} + \frac{R''}{A_1^3} {}_1 \bar{u}_3 \right) - \bar{E}_{11}^{(1)} = 0, \quad (4.79)$$

$$\delta_1 \bar{\sigma}^{12} : \quad - \frac{d^3}{12} \frac{R'}{A_1} {}_1 \bar{u}_2 - R \bar{\Phi}_{12}^{(1)} - R \bar{E}_{12}^{(1)} = 0, \quad (4.80)$$

$$\delta_1 \bar{\sigma}^{13} : \quad \frac{d^3}{12} \left(\frac{RR''}{A_1^3} - \frac{1}{A_1} \right) {}_1 \bar{u}_1 - dR_0 \bar{u}_1 - R \bar{\Phi}_{13}^{(1)} - R \bar{E}_{13}^{(1)} = 0, \quad (4.81)$$

$$\delta_1 \bar{\sigma}^{21} : \quad \frac{d^3}{12} \left(R_1 \bar{u}_{2,1} - \frac{R'}{A_1} {}_1 \bar{u}_2 \right) - R \bar{\Phi}_{21}^{(1)} - R \bar{E}_{21}^{(1)} = 0, \quad (4.82)$$

$$\delta_1 \bar{\sigma}^{22} : \quad \frac{d^3}{12} \left(\frac{RR'}{A_1} {}_1 \bar{u}_1 + \frac{R}{A_1} {}_1 \bar{u}_3 \right) - \bar{E}_{22}^{(1)} = 0, \quad (4.83)$$

$$\delta_1 \bar{\sigma}^{23} : \quad \frac{d^3}{12} \left(\frac{RR''}{A_1^3} - \frac{1}{A_1} \right) {}_1 \bar{u}_2 - dR_1 \bar{u}_2 - R \bar{\Phi}_{23}^{(1)} - R \bar{E}_{23}^{(1)} = 0, \quad (4.84)$$

$$\delta_1 \bar{\sigma}^{31} : \quad \frac{d^3}{12} \left({}_1 \bar{u}_{3,1} + \frac{R''}{A_1^3} {}_1 \bar{u}_1 \right) - \bar{\Phi}_{31}^{(1)} - \bar{E}_{31}^{(1)} = 0, \quad (4.85)$$

$$\delta_1 \bar{\sigma}^{32} : \quad - \frac{d^3}{12A_1} {}_1 \bar{u}_2 - R \bar{\Phi}_{32}^{(1)} - R \bar{E}_{32}^{(1)} = 0, \quad (4.86)$$

$$\delta_1 \bar{\sigma}^{33} : \quad \frac{d^3}{12} \left(\frac{RR''}{A_1^3} - \frac{1}{A_1} \right) {}_1 \bar{u}_3 - dR_0 \bar{u}_3 - R \bar{E}_{33}^{(1)} = 0, \quad (4.87)$$

$$\delta_2 \bar{\sigma}^{13} : \quad - \frac{d^3}{6} {}_1 \bar{u}_1 - \bar{\Phi}_{13}^{(2)} - \bar{E}_{13}^{(2)} = 0, \quad (4.88)$$

$$\delta_2 \bar{\sigma}^{23} : \quad - \frac{d^3}{6} {}_1 \bar{u}_2 - \bar{\Phi}_{23}^{(2)} - \bar{E}_{23}^{(2)} = 0, \quad (4.89)$$

$$\delta_2 \bar{\sigma}^{33} : \quad - \frac{d^3}{6} {}_1 \bar{u}_3 - \bar{E}_{33}^{(2)} = 0, \quad (4.90)$$

and the natural boundary conditions

$$\delta_0 \bar{\sigma}^{n1} : \quad -d_0 \bar{u}_n|_{\xi^1=0} - \tilde{\bar{u}}_n^{(0)} = 0, \quad (4.91)$$

$$\delta_1 \bar{\sigma}^{n1} : \quad -\frac{d^3}{12} {}_1\bar{u}_n|_{\xi^1=0} - \tilde{\bar{u}}_n^{(1)} = 0. \quad (4.92)$$

The Euler-Lagrange equations of Hellinger-Reissner's variational principle with functional (4.41) are the rotational and translational equilibrium equations, (4.56)–(4.61) and (4.62)–(4.67), respectively, the kinematic equations (4.70)–(4.90) and the displacement boundary conditions (4.91)–(4.92).

5. CONCLUSIONS

A new dimensionally reduced shell model in terms of displacements, rotations and non-symmetric stresses has been derived for axisymmetric shells applying the three-dimensional dual-mixed variational principle of Hellinger-Reissner. The displacement and rotation fields appearing in this principle are considered as Lagrangian multipliers that enforce the translational and the rotational equilibrium equations into the functional of the total complementary energy. *A priori* satisfaction of the stress boundary conditions is required, boundary conditions for the rotations cannot be prescribed.

After describing the geometry of the shell of revolution, the main steps of the dimensional reduction in terms of displacements, rotations and non-symmetric stresses are presented. Applying a special form of the Hellinger-Reissner functional derived for shells of revolution and introducing the notion of strain, rotation and prescribed displacement resultants, the Euler-Lagrange equations and the natural boundary conditions of the dimensionally reduced shell model are derived, assuming axisymmetrical loads. These equations, written in terms of one-dimensional variables defined on the middle surface of the shell, consist of the special forms of the translational and rotational equilibrium equations, the kinematic equations and the displacement boundary conditions. The Euler-Lagrange equations obtained may be used for analytical investigations of shells of revolution with special geometry, especially when closed-form solutions in terms of the stress field can be constructed.

The most important features of the shell model derived and presented in this paper can be summarized as follows:

- Classical kinematical hypotheses regarding the deformation of the normal to the shell middle surface are not applied.
- The transverse normal stress distribution is parabolic across the thickness of the shell. This allows for the deformation of the shell in the thickness direction.
- Unmodified three-dimensional constitutive equations are applied and, at the same time, the inverse stress-strain relations for linearly elastic isotropic materials do not contain the $1/(1 - 2\nu)$ term. This fact has importance from the point of view of an incompressibility locking-free finite element formulation, when the Poisson ratio ν is close to the incompressible limit of 0.5.

The finite element formulation and the development of new *hp*-version dual-mixed finite element models based on the shell theory presented in this paper are the next step of the research work in this direction.

Acknowledgements. This work was supported by the Hungarian Scientific Research Fund under Grant No. OTKA T49427 and by the European Union and the State of Hungary, co-financed by the European Social Fund in the framework of TÁMOP-4.2.4.A/2-11/1-2012-0001 „National Excellence Program”.

REFERENCES

1. BÉDA, GY., KOZÁK, I.: *Mechanics of elastic bodies*, Műszaki Könyvkiadó, Budapest, 1987 (in Hungarian).
2. BÉDA, GY., KOZÁK, I. and VERHÁS, J.: *Continuum Mechanics*, Akadémiai Kiadó, Budapest, 1995.
3. BERTÓTI, E.: Complementary energy method for cylindrical shells using second order stress functions, *Computer Methods in Applied Mechanics and Engineering* 1993; **108**:147-163.
4. BERTÓTI, E.: *Non-linear shell theory in terms of stresses and rotations*, DSc thesis, Hungarian Academy of Sciences – University of Miskolc, 2003, p. 133 (in Hungarian).
5. BREZZI, F., FORTIN, M.: *Mixed and hybridfinite element methods*, Springer Verlag, New York, 1991.
6. FRAEIJIS DE VEUBEKE, B.M. A new variational principle for finite elastic displacements, *International Journal of Engineering Sciences* 1972; **10**:745-763.
7. HELLINGER, E.: Der allgemeine Ansatz der Mechanik der Kontinua, *Encyclopädie der Mathematischen Wissenschaften* 1914; **4**:602-694.
8. NAGHDI, P. M.: *Foundations of Elastic Shell Theory*, In: Progress in Solid Mechanics, Volume IV (I. N. Sneddon and R. Hill, Eds.), North-Holland Publishing Company, Amsterdam, 1963, pp. 1–90.
9. REISSNER, E.: On a variational theorem in elasticity, *Journal of Mathematics and Physics* 1950; **29**:90–95.
10. REISSNER, E.: A note on variational principles in elasticity, *International Journal of Solids and Structures* 1965; **1**:93-95

Notes for Contributors

to the Journal of Computational and Applied Mechanics

Aims and scope. The aim of the journal is to publish research papers on theoretical and applied mechanics. Special emphasis is given to articles on computational mechanics, continuum mechanics (mechanics of solid bodies, fluid mechanics, heat and mass transfer) and dynamics. Review papers on a research field and materials effective for teaching can also be accepted and are published as review papers or classroom notes. Papers devoted to mathematical problems relevant to mechanics will also be considered.

Frequency of the journal. Two issues a year (approximately 80 pages per issue).

Submission of Manuscripts. Submission of a manuscript implies that the paper has not been published, nor is being considered for publication elsewhere. Papers should be written in standard grammatical English. The manuscript is to be submitted in electronic, preferably in pdf, format. The text is to be 130 mm wide and 190 mm long and the main text should be typeset in 10pt CMR fonts. Though the length of a paper is not prescribed, authors are encouraged to write concisely. However, short communications or discussions on papers published in the journal must not be longer than 2 pages. Each manuscript should be provided with an English Abstract of about 50–70 words, reporting concisely on the objective and results of the paper. The Abstract is followed by the Mathematical Subject Classification – in case the author (or authors) give the classification codes – then the keywords (no more than five). References should be grouped at the end of the paper in numerical order of appearance. Author's name(s) and initials, paper titles, journal name, volume, issue, year and page numbers should be given for all journals referenced.

The journal prefers the submission of manuscripts in L^AT_EX. Authors should prefer the $\mathcal{A}\mathcal{M}\mathcal{S}$ -L^AT_EX article class and are not recommended to define their own L^AT_EX commands. Visit our home page for further details concerning the issue how to edit your paper.

For the purpose of refereeing the manuscripts should be sent either to Balázs Tóth (Balazs.TOTH@uni-miskolc.hu) or György SZEIDL (Gyorgy.SZEIDL@uni-miskolc.hu).

The eventual supply of an accepted for publication paper in its final camera-ready form will ensure more rapid publication. Format requirements are provided by the home page of the journal from which sample L^AT_EX files can be downloaded:

<http://www.mech.uni-miskolc.hu/jcam>

These sample files can also be obtained directly (via e-mail) from Balázs TÓTH (Balazs.TOTH@uni-miskolc.hu), upon request.

One issue of the journal and ten offprints will be provided free of charge and mailed to the correspondent author. Since JCAM is an open access journal each paper can be downloaded freely from the homepage of the journal.

The Journal of Computational and Applied Mechanics is abstracted in Zentralblatt für Mathematik and in the Russian Referativnij Zhurnal.

Secretariat of the Vice-Rector for Research and International Relations, University of Miskolc
Responsible for publication: Prof. Dr. Tamás Kékesi
Published by the Miskolc University Press under the leadership of Erzsébet Burmeister
Responsible for duplication: Works manager Erzsébet Pásztor
Number of copies printed: 75
Put to the Press on June 5, 2014
Number of permission: TNRT 2014-200-ME

HU ISSN 1586–2070

A Short History of the Publications of the University of Miskolc

The University of Miskolc (Hungary) is an important center of research in Central Europe. Its parent university was founded by the Empress Maria Teresia in Selmechánya (today Banská Štiavnica, Slovakia) in 1735. After the first World War the legal predecessor of the University of Miskolc moved to Sopron (Hungary) where, in 1929, it started the series of university publications with the title *Publications of the Mining and Metallurgical Division of the Hungarian Academy of Mining and Forestry Engineering* (Volumes I.-VI.). From 1934 to 1947 the Institution had the name Faculty of Mining, Metallurgical and Forestry Engineering of the József Nádor University of Technology and Economic Sciences at Sopron. Accordingly, the publications were given the title *Publications of the Mining and Metallurgical Engineering Division* (Volumes VII.-XVI.). For the last volume before 1950 – due to a further change in the name of the Institution – *Technical University, Faculties of Mining, Metallurgical and Forestry Engineering, Publications of the Mining and Metallurgical Divisions* was the title.

For some years after 1950 the Publications were temporarily suspended.

After the foundation of the Mechanical Engineering Faculty in Miskolc in 1949 and the movement of the Sopron Mining and Metallurgical Faculties to Miskolc, the Publications restarted with the general title *Publications of the Technical University of Heavy Industry* in 1955. Four new series - Series A (Mining), Series B (Metallurgy), Series C (Machinery) and Series D (Natural Sciences) - were founded in 1976. These came out both in foreign languages (English, German and Russian) and in Hungarian.

In 1990, right after the foundation of some new faculties, the university was renamed to University of Miskolc. At the same time the structure of the Publications was reorganized so that it could follow the faculty structure. Accordingly three new series were established: Series E (Legal Sciences), Series F (Economic Sciences) and Series G (Humanities and Social Sciences). The latest series, i.e., the series H (European Integration Studies) was founded in 2001. The eight series are formed by some periodicals and such publications which come out with various frequencies.

Papers on computational and applied mechanics were published in the

Publications of the University of Miskolc, Series D, Natural Sciences.

This series was given the name Natural Sciences, Mathematics in 1995. The name change reflects the fact that most of the papers published in the journal are of mathematical nature though papers on mechanics also come out.

The series

Publications of the University of Miskolc, Series C, Fundamental Engineering Sciences

founded in 1995 also published papers on mechanical issues. The present journal, which is published with the support of the Faculty of Mechanical Engineering as a member of the Series C (Machinery), is the legal successor of the above journal.



Contents

Contributed Papers

- Jean-Michel DHAINAUT, Guangfeng CHENG and Chuh MEI: Response of plates under statistically unsynchronized uniform random loads using Monte-Carlo simulation 3–18
- Balázs PERE, János ÉGERT and Tamás SZABÓ: Reinforcement of inner and outer circular failures of pipes by textile composite layers 19–33
- Béla KOVÁCS: Vibration analysis of a piezoelectric cylinder panel 35–47
- János LÓGÓ: Topology optimization in the case of different boundary conditions by an iterative method 49–64
- D. K. SRIVASTAVA, N. SRIVASTAVA and Raja Ram YADAV: Quadratic flow past axially symmetric bodies at low Reynolds number 65–100
- Balázs TÓTH: Axisymmetric shell model using a three-field dual-mixed variational principle 101–119